UNCONVENTIONAL RESERVOIR FLOW SIMULATION: AN IMPROVED BOUNDARY ELEMENT FRACTURE MODELING TECHNIQUE AND THE INFLUENCE OF MULTI-COMPONENT DIFFUSION/ADSORPTION

A Dissertation

by

YANG CAO

Submitted to the Office of Graduate and Professional Studies of
Texas A&M University
in partial fulfillment of the requirements for the degree of

DOCTOR OF PHILOSOPHY

Chair of Committee,	John E. Killough
Committee Members,	Eduardo Gildin
	I. Yucel Akkutlu
	Vivek Sarin
Head of Department,	Jeff Spath

December 2018

Major Subject: Petroleum Engineering

ABSTRACT

The natural fractures and hydraulic fractures often form complex fracture network in shale reservoirs, which poses great challenge to the flow simulation of such complex reservoirs. In this study, a theoretically sound, and practically robust boundary element method (BEM) numerical algorithm is developed and successfully implemented. Explicit and discrete fracture description is adopted in this approach, and the complex fracture settings and interactions are effectively simulated. Comparing with the domain discretization methods (e.g., finite element method (FEM), finite difference method (FDM)), mesh generation is greatly simplified in our approach, especially for reservoirs with complex fracture configurations. Case studies show: our algorithm is capable of modeling two-dimensional (2D) steady state flow in fractured reservoirs with different boundary conditions and complex fracture networks; also, the transient flow dynamics and the flow dependence on matrix heterogeneity, which are seldom considered through a BEM approach, are successfully accounted for; in addition, by characterizing the fracture flow using finite volume element (FVM) formulation, the fluid flow in three-dimensional (3D) fractured reservoirs with irregular fractures is properly handled through this algorithm.

Multiple porosity systems (especially organic matter) existing in shale reservoirs require a reservoir simulator to properly account for the multi-component diffusion/adsorption phenomena occurring in the matrix. A compositional model specifically tailored for the characteristics of shale reservoirs is thus developed. The model takes the pressure and component molar masses as the primary variables, and the IMPEM (implicit pressure and explicit mass) method as the solution technique. The multi-component adsorption and diffusion influences are shown to be successfully accounted for through this model. Case studies indicate: the multi-component adsorption which mainly exists in the shale organic matter usually plays a positive role in shale reservoir recovery; the influence of the different TOC values on shale fluid recovery may be different depending on the fluid type and the operating conditions; and the multi-component diffusion facilitates the gas recovery, yet the degree of this improvement differs for different wettability formations.

DEDICATION

To my family.

ACKNOWLEDGMENTS

I am deeply indebted to my advisor, Professor John E. Killough, for his continuous and unreserved help, guidance, and support in the past few years. Without him, I wouldn't have been able to complete this doctoral degree.

I would like to thank Professor Eduardo Gildin, Professor I. Yucel Akkutlu and Professor Vivek Sarin for taking their time to sit on my advisory committee, and for their valuable comments and suggestions on my research work.

Special thanks to Dr. Bicheng Yan, Dr. Masoud Alfi, Dr. Lidong Mi, Dr. Hongqing Song for their advice and help. Also thanks to my officemates Dr. Xuyang Guo, Cheng An, Sunhua Gao, Abdul Hamed Alfale, and other Killough group members for their help and fellowship during my graduate studies.

Besides, I would like to express my gratitude to Professor I. Yucel Akkutlu, Professor Eduardo Gildin, Professor A. Daniel Hill, Professor Michael King, Professor Adam Larios, Professor Raytcho Lazarov, Professor William D. McCain, Jr., Professor George Moridis, Professor Nobuo Morita, Professor Peter Valkó, Professor Ding Zhu, and the late Professor Bob Wattenbarger. I have taken their courses. Their knowledge and wisdom aided me a lot in the study and research.

Furthermore, I would like to acknowledge my thankfulness to the great Texas A&M University. I enjoy the life here. It not only improved me academically, but also enriched me professionally and spiritually. I am always thankful. Once an Aggie, always an Aggie.

Finally, many thanks to my family for their endless love and support.

CONTRIBUTORS AND FUNDING SOURCES

Contributors

This work was supported by a dissertation committee consisting of Professor John E. Killough [advisor], Professor I. Yucel Akkutlu and Professor Eduardo Gildin of the Department of Petroleum Engineering , and Professor Vivek Sarin of the Department of Computer Science and Engineering.

The application of finite element method (FEM) simulator for result comparison in Section 2 to Section 4 was helped by Dr. Lidong Mi, who was a visiting scholar to Texas A&M University from the Department of Petroleum Engineering at China University of Petroleum, Beijing.

The other work conducted for the dissertation was completed by the student independently.

Funding Sources

Graduate study was supported by the Graduate Teaching Assistantship from Texas A&M University and Section 5 of this dissertation was funded by the Crisman Institute at Texas A&M University.

NOMENCLATURE

b	right hand side function in Poisson's equation
c	coefficient in boundary integral equation
c_t	total compressibility
C	fracture element
d	distance
D	vertical depth, or diffusion coefficient
f	interpolation basis function in DRBEM
F_1, F_2	line integral
J	diffusion molar flux
k	permeability
l	connecting side length
L	square side length, or number of internal nodes
m	time step, or number of PEBI element sides, or molar mass of component
M	molecular weight
n	outward normal vector, or number of components
n_f	number of embedded fractures
N	number of nodes or elements
p	pressure
$\boldsymbol{P_{fe}}$	vector containing fracture element end point pressures
$\boldsymbol{P_{fm}}, \boldsymbol{P_f}$	vector containing fracture element collation point pressures
Q	fracture linear or planar source strength, or adsorption molar mass

$\boldsymbol{Q}$	fracture source strength vector
Q_a	adsorbed gas storage capacity
t	time
u	transformed variable from pressure p
$u, \vec{v}$	Darcy velocity
$\boldsymbol{U}$	vector containing boundary unknowns
w_f	fracture aperture
x	molar fraction
x, y	local coordinate
$\vec{x}$,$\vec{z}$	local coordinate at matrix and fracture, respectively
$\boldsymbol{A_1}, \boldsymbol{A_2}, \boldsymbol{B_1}, \boldsymbol{B_2}, \boldsymbol{B_3}, \boldsymbol{B_4}, \boldsymbol{C_2}, \boldsymbol{C_3}, \boldsymbol{C_4}, \boldsymbol{D_3}, \boldsymbol{D_4}$	coefficient block matrices in matrix-vector system
$\boldsymbol{R_1}, \boldsymbol{R_2}, \boldsymbol{R_3}$	right hand side vector terms in matrix-vector system

Greek:

α	weight in DRBEM, or shape factor in Warren-Root dual porosity model
Γ	boundary
δ	Dirac delta function
ϵ	relative error
θ	angle between fracture and the perpendicular line of its intersecting boundary
λ, τ	dimensionless parameters in Warren-Root dual porosity model
μ	viscosity
ξ, μ	local coordinate
ρ	density

ϕ	porosity
Φ	fundamental solution of 2D Laplace's equation

Subscripts & Superscripts :

b	boundary
eb	neighboring elements
eff	effective
f	fracture
fm	fracture element collation (middle) point
fe	fracture element end point
hc	non-aqueous components
i	component
M	molecular diffusion
K	Knudsen diffusion
t	total
w	water
α	phase

Abbreviations:

2D	two dimensional
3D	three dimensional
BEM	boundary element method
BIE	boundary integral equation
DFN	discrete fracture network
DRBEM	dual reciprocity boundary element method
EDFM	embedded discrete fracture method
FEM	finite element method

FVM	finite volume method
IMPEM	implicit pressure explicit molar mass
PEBI	perpendicular bisector
MINC	multiple interacting continua approach
R.H.S.	right hand side
TOC	total carbon content

TABLE OF CONTENTS

Page

LIST OF FIGURES

FIGURE Page

LIST OF TABLES

TABLE Page

1. INTRODUCTION AND LITERATURE REVIEW

Fluid flow simulation in shale reservoirs has never been an easy task for researchers and engineers. The abundant natural fractures usually existing in shale reservoirs, together with the complex primary fracture clusters induced by the hydraulic fracturing, pose great challenge to the fracture modeling techniques. Also, the existence of multiple porosity systems (organic matter, inorganic matter, and fractures), especially the nano-scale organic pores, attracts researchers to study Non-Darcy flow effects on fluid flow in shale reservoirs. In this proposal, we try to advance knowledge towards these two aspects. In the first aspect, an improved boundary element method (BEM) is proposed to facilitate flow simulation in fractured shale reservoirs. In the second aspect, the influence of the important Non-Darcy flow mechanisms, namely multi-component diffusion and adsorption, on shale reservoir fluid flow, has been studied through a novel compositional simulator we developed. These two aspects are not exclusively independent, and studies integrating both aspects exist. But currently we constrain ourselves to these studies in a parallel fashion with emphasis on the first aspect.

First to concentrate on the aspect of fracture modeling techniques in shale reservoirs. The difficulties mainly lie in the embedded fractures which are usually multiple-scale, irregularly shaped and have complex connections. The conductivities of the fracture network are usually orders of magnitude larger than those of the surrounding matrix (Wang et al. 2015). To honor the complex fracture geometry and connection, also fully capture the sharp pressure transition between fractures and the matrix, large number of refined, preferably unstructured grids are required to be put around the fracture-matrix interfaces, which renders the popular finite difference method (FDM) cumbersome in simulating realistic fractured reservoir fluid flow. Several other approaches have therefore been adopted to tackle this problem.

1.1 Continuum medium methods

The industrial standard approach is the dual-porosity model (DPM). The dual-porosity concept was first introduced by Barenblatt and Zheltov (1960), later popularized by Warren and Root (1963) in the oil and gas industry. In this model, the fractures are viewed as a separate, continuous porous medium with appropriate attributes definable to characterize its hydraulic properties (Cao and Killough, 2016). Most of the reservoir fluid is stored in the matrix, while the fractures serve as the main flow conduits. Depending on whether intra-flow is allowed in the matrix, DPM can be sub-divided into two sub-categories: dual-porosity single-permeability model (DPSK, no matrix intra-flow) and dual-porosity dual-permeability model (DPDK, having matrix intra-flow), see Fig.1.1. The reason of DPM's popularity is in its simplicity. The complicated fracture network is lumped into one porous medium, and the complex interflow between fractures and matrix is described by the term called transfer function, which can be calculated either through analytical method (Kazemi et al. 1976) or history match. DPM is appropriate for reservoirs with highly connected, small-scale fractures (Jiang and Younis, 2015) and is proved useful in many applications. It has been extended to characterize two-phase flow (Kazemi et al. 1976) and three-phase flow (Thomas et al. 1983) in fractured reservoirs.

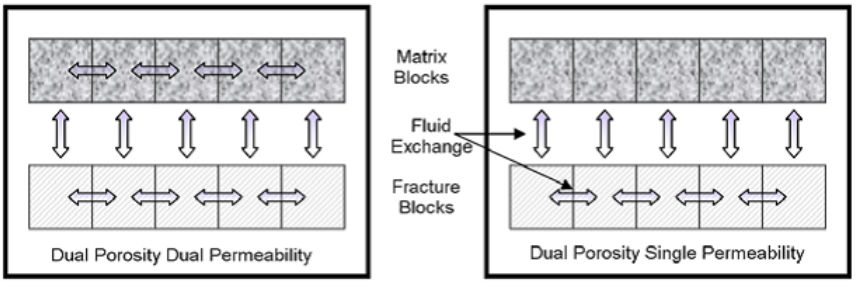

Figure 1.1: Connection schematic: DPDK (Left) and DPSK (Right). Reprinted from Figure 10.2 in Halliburton (2013)

The standard DPMs assume constant pressure and saturation in each matrix block, which may not be the case for local matrix regions with large spatial variations (Karimi-Fard et al. 2006).

To incorporate the spatial variability, the time or saturation-dependent transfer functions are developed, such as Zimmerman et al (1993), and Sarma and Aziz (2004). Another approach for resolving this issue is matrix subdivision. In this approach, the matrix cell is sub-divided into several sub-grids to capture the flow dynamics in the matrix. Different subgridding strategies exist, such as Gilman (1986), Gilman and Kazemi (1988), and Karimi-Fard et al. (2006), among them the most famous one is the multiple interacting continua approach (MINC) (Pruess and Narasimhan, 1985; Wu and Pruess, 1988). In order to divide the sub-grids more realistically, Pruess and Karasaki (1982) proposed the concept of proximity function, which represents the total matrix volume within some distance from the fracture faces, and can be computed through Monte Carlo integration. Also Karimi-Fard et al. (2006) established a coarse-scale continuum flow models where the geometry of the local subgrids and the required parameters are determined from local flow solutions using the underlying discrete fracture model. Gong et al. (2008) extended the approach of Karimi-Fard et al. (2006) to include the gravity influence, and Hui et al. (2007), Hui et al. (2008) successfully applied this technique to solve a number of flow problems. The methodologies of Pruss and Karasaki (1982), Karimi-Fard et al. (2006), and Gong et al. (2008) are subordinate to a broader endeavor where the dual-porosity parameters are extracted from the underlying discrete fracture models. Some of the other research in this respect are Dershowitz et al. (2000) and Sarda et al. (2002).

DPM belongs to continuous medium methods, other similar methods exist, such as single-medium method and multi-porosity method. When adequate pseudo-capillary pressure curves and pseudo-relative permeability curves are defined, single-medium method can be used to perform fractured reservoir simulation with acceptable accuracy (Sarda et al. 2002). In order to honor the complex interaction during shale reservoir's multiple porosity systems (such as organic matter, inorganic matter, natural fractures, and hydraulic fractures), several researchers (Hinkley et al. 2013; Sun et al. 2014; Yan et al. 2015) have explored the multi-porosity approach, where each porosity system is generalized as a separate, continuous porous medium respectively. Arbitrary intra-porosity and inter-porosity connection can be studied, and features capable of porosity subdi-

vision are also developed (Yan et al. 2015). The multi-porosity approach provides large flexibility in handling the complex interaction in complex lithology reservoirs, also can readily honor the specialty of each porosity system, yet the troublesome of determining or history match multiple transfer function parameters hinders its popularization.

1.2 Discrete fracture methods

To the contrary of continuous medium methods, the discrete fracture modeling (DFM) approach treats the fractures discretely and explicitly. Comparing to continuous methods, DFMs can resolve the flow details of complex flow paths and high, localized anisotropy even with large fracture density and sever irregular fracture patterns (Moinfar et al. 2011). The main differences among various DFM techniques lie in how they characterize and discretize the fracture networks. A simple approach is the discrete fracture network (DFN) model, where only the fracture intersections are meshed and fracture matrix interflow is linked through the middle points (recharge points) of the intersections (Mckoy and Sams, 1997; Mi et al. 2016). More complex approaches not only consider the fracture intersections and end points, but also discretize and set unknowns along each fracture line or surface. In these approach, several numerical methods have been adopted. For example, Rubin (2010) and He et al. (2015) used finite difference method (FDM) to discretize the fracture network and simulate fluid flow. And due to the constraints mentioned above, FDM usually is applied in reservoirs with regular fracture patterns (Rubin, 2010) or adopts large number of refined grids (He et al. 2015). Karimi-Fard et al. (2004) developed a finite volume method (FVM) based simulator, where the concept of delta transfer function was proposed to eliminate control volumes at fracture intersections, which facilitate the simulation process. Syihab (2009) discretized the two-dimensional (2D) DFN using Voronoi diagrams, and the non-uniform aperture distribution was implicitly accounted through appropriate computation domain treatment. To the contrary, Sun and Schechter (2014) simulated the natural fractures with actual aperture sizes explicitly using unstructured grids, and a force-based optimization method was combined with the fixed-point scheme to ensure good mesh quality. For fractured reservoirs with homogeneity matrix, boundary element method (BEM) has been used by several researchers. Rasmussen et al.

(1987) applied the boundary integral method to determine the relative contribution of the fracture flow and the matrix flow to the total liquid flow, and for fracture discretization, nodes were placed around the rim of each fracture. Lough et al. (1995, 1997, 1998) and Shapiro et al. (1983) both set only one single layer potential type integral for each fracture, and differences existed in their discretization schemes. When the fractured reservoirs contain very complex configurations, where the small distance between fracture extremities and the small angles between fractures pose great difficulties for good mesh generation, techniques reducing the complex structures and provide optimal grids exist (Graf and Therrien, 2007; Mustapha and Dimitrakopoulos, 2011; Mustapha et al. 2011). These methodologies indicate that the best strategy to simulate flow in fractured shale reservoirs is probably to first modify the given complex fracture configurations to some extent, instead of strictly adhering to the given fracture network throughout the simulation.

1.3 Integration methods

Studies combining the continuum medium approach and the discrete fracture approach have been conducted. The discrete fracture methods honor the local fracture configurations and can be used to generate the apparent or equivalent properties (permeability, conductivity, etc) for local grids, which afterwards can be taken as inputs for the continuum medium methods to simulate global scale fluid flow. The researches, such as Pruess and Karasaki (1982), Karimi-Fard et al. (2006), Gong et al. (2008), and Dershowitz et al. (2000) all belong to this category. Lough et al. (1995, 1997, 1998) and Teimoori et al. (2005) conducted similar investigations using BEM, where only the local grid boundaries and the fracture surfaces are discretized instead of domain discretization as for other methods. Jiang and Younis (2015) proposed a coupled method which integrates unstructured DFM with continuum models which can include dual-porosity, dual-permeability and MINC features. Another direction integrating the merits of both the continuum medium approach and discrete fracture approach comes from Lee et al. (2001), Li and Lee (2008) and Moinfar (2013), who proposed and studied the embedded discrete fracture method (EDFM). In this approach, the matrix is represented by structured grids, while additional fracture control volumes are applied for computing the intersection of fractures with the matrix grid. And this approach has at-

tracted attention of many researchers. Jiang and Younis (2015) developed a hybrid fracture model by combing EDFM with MINC to simulate unconventional gas reservoirs. Chai et al. (2016) explored the methodology of combing multiple porosity model and EDFM model, and highlighted their simulator's capacity for dynamic fracture network modeling. Recently, Ding et al. (2017) presents an EDFM based on the MINC proximity function to overcome the insufficiency of the conventional dual-porosity model in simulating unconventional reservoirs.

Continuum medium method disregards the explicit simulation of specific fracture configuration and interaction, thus simplifies the simulation process. Discrete fracture method, on the other hand, aims to capture the details of the flow dynamics induced by the fractures, which irrefutably improves the simulation accuracy yet carries heavier computation burden. Besides, the intrinsic uncertainties of the fracture characterization parameters probably blur the improved accuracy from the discrete fracture modeling. Therefore a good simulation strategy should balance off both the accuracy and efficiency. The hierarchical fracture models developed by Lee et al. (2001) and Hajibeygi et al. (2011) are two good examples in this regard.

Next, we will introduce the second aspect: the influence of multi-component diffusion/adsorption on fluid flow in shale reservoirs. The background on this subject is briefly summarized as following.

1.4 Multi-component adsorption/diffusion *

Four types of porosity systems coexist in shale reservoirs: organic matter, inorganic medium, natural fractures and hydraulic fractures, with different attributes associated with each (Wang and Reed, 2009). Significant porosity is discovered to exist within shale organic matter, and as pointed out by Loucks et al. (2009), most of the nano-pores are located in the organic matter. Large amounts of adsorbed hydrocarbon may exist in the porous organic matter of the shale matrix. Hill et al. (2000) mentioned that in some cases 85% of gas in shale might be stored as adsorbed gas. Proper treatment of the influence of adsorbed hydrocarbon on shale reservoir development is an

*Part of this section is reprinted with permission from "A Novel Compositional Model of Simulating Fluid Flow in Shale Reservoirs - Some Preliminary Tests and Results" by Y. Cao, B. Yan, M. Alfi and J. E. Killough, 2015. SPE Proceedings, Copyright [2015] by Society of Petroleum Engineers.

indispensable requirement for shale reservoir modeling to be realistic and accurate.

Also, as the pore size and the permeability decrease significantly in the shale matrix, Darcy flow may not be appropriate or adequate to describe the fluid flow in such media (Yan et al. 2013). Several methods have been proposed to describe the fluid flow in tight formations, such as the Dual-Mechanism Approach (Darcy flow and Fickian diffusion occur simultaneously) (Ertekin et al. 1986; Clarkson et al. 2010); the apparent permeability approach, either based on considering the combining effect of various flow mechanisms (Knudsen diffusion, slippage flow and advection flow) (Javadpour et al. 2009) or based on the condition of Knudsen number (Civan 2010); a more practical method is to use the experimentally determined effective diffusivity (which lumps both convection and diffusion) in the simulation (Sun et al. 2014). But the above mentioned methods or approaches limit the diffusivity or permeability adjustment to a single phase or component. Different diffusivity or permeability adjustments should be incorporated for different components. A compositional model specifically accounting for the aforementioned aspects should be developed.

1.5 Research objective and dissertation structure

The first objective of this work will focus on advancing BEM application in simulating fluid flow in fractured shale reservoirs. It belongs to the discrete fracture method category, and can be used to generate the local grid apparent or equivalent properties passing to the continuum medium method. Several limitations suffered by the previous studies are removed in this work, which include: (1) more compacted and efficient BEM formulations modeling fractured reservoirs fluid flow are proposed, (2) modules characterizing the transient flow dynamics and the matrix heterogeneity influence on fluid flow, which are seldom considered through a BEM perspective by previous researchers, are developed and investigated, and (3) in three-dimensional (3D) cases, the workflow for discretizing the fracture and the boundary surfaces, and the characterization of fracture flow using finite volume method (FVM) formulation are developed, which enable BEM simulator to readily model fluid flow in reservoirs with irregular fracture patterns. Other issues, such as the influence of the boundary and fracture element discretization strategy, are also covered.

The second objective of this work is to develop a new compositional simulator specifically

for shale fluid storage and flow modeling. The multi-component adsorption and diffusion phenomena occurring in the shale matrix are properly incorporated. The influences of the important parameters, such as total carbon content, wettability, and fluid composition, on shale reservoir fluid recovery are also investigated through this new simulator.

The following of this dissertation is arranged as these. In Section 2, our improved boundary element model for simulating steady state flow in 2D homogeneous fractured reservoirs is presented. (In this dissertation, the homogeneity or heterogeneity of the fractured reservoirs is defined by the properties of the matrix medium. If the matrix is homogeneous/heterogeneous, then the reservoirs are called homogeneous/heterogeneous by simplification.) The theoretical background and the case studies using this model are also described.

In Section 3, the theoretical background of the dual reciprocity boundary element method (DRBEM), which is a technique for treating matrix heterogeneity and transient flow dynamics in this work, is first briefly summarized. The technique for modeling matrix heterogeneity and transient flow in fractured shale reservoirs is then introduced. Examples verifying the feasibility of the model are presented. Studies on the influence of the matrix permeability, fracture permeability, and fluid viscosity on the transient flow dynamics are also to be discussed.

In Section 4, we extend the model to simulating flow in three-dimensional (3D) fractured reservoirs. Complex and irregular fracture configurations can be investigated. The description of the discretization scheme and the numerical implementation will first be described in this chapter. Then examples and discussions showing fluid flow in 3D porous medium with and without fractures are illustrated to validate our approach. The final part is devoted to the conclusion.

In Section 5, the equations and the methodology adopted in the development of the compositional simulator are discussed. The multi-component adsorption and diffusion terms are incorporated into the component mass balance equations. Several cases are conducted to validate the model. The influences of the important parameters, such as total carbon content, wettability, and fluid composition, on shale reservoir fluid recovery are investigated through the new simulator.

The last section (Section 6) presents the conclusion and the suggested future work.

2. STEADY STATE FLOW SIMULATION FOR 2D HOMOGENEOUS FRACTURED RESERVOIR*

In this section, we introduce the simulation of steady state flow in two-dimensional homogeneous fractured reservoirs. First, the background of boundary integral equation and boundary element method is introduced. This serves the basis for our improved boundary element method in this section and the following two sections. Then, the methodology of the improved boundary element method in simulating steady state flow in 2D homogeneous fractured reservoirs is shown. Finally, examples verifying the feasibility of our approach are presented. Conclusions are presented in the end.

2.1 BEM basics

The partial differential equations characterizing the physical problem can be converted to an integral form using the technique of weighted residuals. By employing integration by parts, we can obtain a series of boundary integrals, and the domain integral contains only the partial derivatives of the weighting function. The domain integral containing the field function can be eliminated by setting the fundamental solution as the weighting function. The resulted representation formula will have no unknown variables in the domain integral. Take Laplace equation as an example.

$$\bigtriangledown^2 p = 0 \quad \text{in} \quad \Omega \tag{2.1}$$

The resulting representation formula is

$$c(\xi)p(\xi) = \int_\Gamma G\frac{\partial p}{\partial n}d\Gamma - \int_\Gamma p\frac{\partial G}{\partial n}d\Gamma \tag{2.2}$$

Where p is the pressure, Γ is the boundary, G is the fundamental solution of the Laplace oper-

*Part of this section is reprinted with permission from "An Improved Boundary Element Method for Modeling Fluid Flow through Fractured Porous Medium" by Y. Cao, and J. E. Killough, 2017. SPE Proceedings, Copyright [2017] by Society of Petroleum Engineers.

ator, ξ is the load point position, and the value of c depends on the position of the load point with respect to the domain Ω, $c = 0$ for load point outside of the domain, $c = 1$ for load point inside, and $c = \frac{1}{2}$ for load point on the smooth boundary. The details on the derivation from Eq.(2.1) to Eq.(2.2) can be found in many references, such as Gaul et al. (2003), Ang (2007) and Archer (2000).

Eq.(2.2) relates one point's pressure with the contour integrals as shown in the right hand side of Eq.(2.2), and when the load point ξ is moved to the boundary, the resulted equation from Eq.(2.2) is the boundary integral equation (BIE). To numerically solve the BIE, the boundary is discretized into small elements honoring the boundary geometry, and the collocation type scheme is used by applying the BIE subsequently at each element node, which will generate the same number of equations as that of the boundary unknowns. And this is the BEM scheme. After the boundary unknowns are solved, the pressure of any point in the interior of the domain Ω can be computed using Eq.(2.2) with $c(\xi) = 1$.

2.2 Governing equations

The fractures embedded in the matrix are generated by nearby seismic activity or through local deformation of the strata containing the porous rock. The generated fractures are usually tortuous, irregular-shaped, with varying sizes of apertures. To improve the simulation efficiency, two simplifications have been made: first, the flow across the fracture apertures is assumed as negligible, and second, the fractures are equivalently seen linear (in 2D reservoirs) or planar (in 3D reservoirs) source or sink entities interacting with the matrix. These simplifications are not totally new. Lough et al. (1998), Shapiro and Andersson (1983) have adopted them in their studies. The justification is that the fracture apertures are usually much smaller than the other dimensions. Based on these assumptions, Lough et al. (1998), Shapiro and Andersson (1983) independently derived the equations governing the 2D fracture flow, and furthermore Lough et al. (1998) estimated the accuracy of this simplification, see Eq.(16) of their paper. The simplifications facilitate the BEM application, previously very fine meshes are required to be placed on the front and back of the fracture surfaces (Rasmussen et al. 1987; Teimoori et al. 2005), now only one layer of meshes are needed,

therefore the computation time and storage requirements are reduced significantly.

Ignoring well source or sink terms, the governing equation for single phase (constant viscosity assumed) flow at any point $\vec{x}$ in the matrix is

$$\bigtriangledown \cdot(k_m \bigtriangledown p) = \phi\mu c_t \frac{\partial p}{\partial t} + \mu \int_f Q(\vec{z})\delta(\vec{x} - \vec{z})dA \tag{2.3}$$

The last term in Eq.(2.3) represents the fracture source term. The governing equation for the mass flow in the fracture is (Lough et al. 1997):

$$\bigtriangledown_f \cdot(\vec{v_f}(\vec{z})) = -\frac{Q(\vec{z})}{w_f} \tag{2.4}$$

In Eq.(2.3) and Eq.(2.4), k_m is the matrix permeability, μ is the fluid viscosity, ϕ is the matrix porosity, c_t is the total compressibility, $\vec{z}$ is a position point in the fracture, Q is the linear or planar source strength of the fracture, $\vec{v_f}$ is the fracture Darcy velocity, w_f is the fracture aperture and δ is Dirac delta function. Eq.(2.3) and Eq.(2.4) are the basic equations in our study to relate the unknowns and solve the problems.

Eq.(2.3) are used to be converted into BEM/DRBEM form, and depending on the given reservoir and fluid conditions, the specific conversions vary; and Eq.(2.4) is transferred and solved either using finite difference method (FDM) for 2D reservoir cases or finite volume method (FVM) for 3D reservoir cases.

The transformation of Eq.(2.3) is shown first. Here we consider steady state flow in homogeneous fractured reservoirs, Eq.(2.3) becomes

$$\bigtriangledown \cdot(\bigtriangledown p) = \frac{\mu}{k_m} \int_f Q(\vec{z})\delta(\vec{x} - \vec{z})dA \tag{2.5}$$

This is the same form as Eq.(5) in Lough et al. (1997), and the corresponding boundary integral equation is shown as Eq.(2.6)

$$c(\xi)p(\xi) = \int_{\Gamma} G\frac{\partial p}{\partial n}d\Gamma - \int_{\Gamma} p\frac{\partial G}{\partial n}d\Gamma + \frac{\mu}{k_m}\int_{f} GQ(\vec{z})dA \tag{2.6}$$

As for Eq.(2.4), the fluid velocity in the fracture is given by Darcy's Law (Lough et al., 1997)

$$\vec{v_f}(\vec{z}) = -\frac{k_f}{\mu} \bigtriangledown p_f \tag{2.7}$$

Substitute Eq.(2.7) into Eq.(2.4), then we get

$$\bigtriangledown_f (\frac{k_f}{\mu} \bigtriangledown p_f) = \frac{Q(\vec{z})}{w_f} \tag{2.8}$$

Where k_f is the fracture permeability, p_f is the fracture pressure, and w_f is the fracture aperture. Depending on the simulated fractured reservoirs, Eq.(2.8) is discretized using the finite difference method (for 2D cases) or finite volume method (for 3D cases, in Section 4). The flexibility of finite volume method enables the handy discretization and simulation of the complex 3D fracture network.

2.3 Discretization scheme

In order to simulate flow in fractured reservoir using the approach we proposed above, the discretization of the fractures need be implemented. In this chapter, we consider the discretization of fractures in a square reservoir porous medium. One example is shown in Fig.2.1. In this case, 6 fractures exist and each fracture can be viewed as a line segment. And the problem of fracture discretization boils down to: how to generate fracture elements given a certain number of fracture segments in a square.

The procedure is as following: (1) Since flow at fracture intersections need special treatment, see Part 2.4.2, first the fracture intersections should be identified. We need check for any pair of the line segments to see if intersection points exist, and if so, the location of the intersection together with the associated fracture indexes need be recorded; (2) And for each fracture segment, the contained intersection points (if existing) plus its two end points are taken as the fixed points

for the fracture element generation. No matter how coarse or refined the following discretization is, these fixed points always serve as the element end points; (3) Generating fracture elements only through the fixed points usually results in low quality element, such as too large fracture elements. To control the size and number of the fracture elements on each fracture segment, the flexible points can be inserted.

For example, 6 fractures exist in Fig.2.1. Among the 6 fractures, 5 fractures intersect directly or indirectly, where 5 intersections A, B, C, D, and E (represented by red circles) exist. Fracture 6 has no fracture intersections. Each fracture segment has its own set of fixed points. Take fracture 3 as an example, where the intersection points (red circles) A, B, C and the two end points (blue circle) M, N are its fixed points. Since the adjacent fixed points A and B form a fracture element with suitable length, no flexible points (green circles) are inserted between them. Otherwise, flexible points (green circles) are inserted between fixed points A and M or B and C. In our example Fig.2.1, 3 flexible points (green circles) are inserted on fracture 3, which results in a total of seven fracture elements. The fracture element can be enclosed by either fixed points or flexible points.

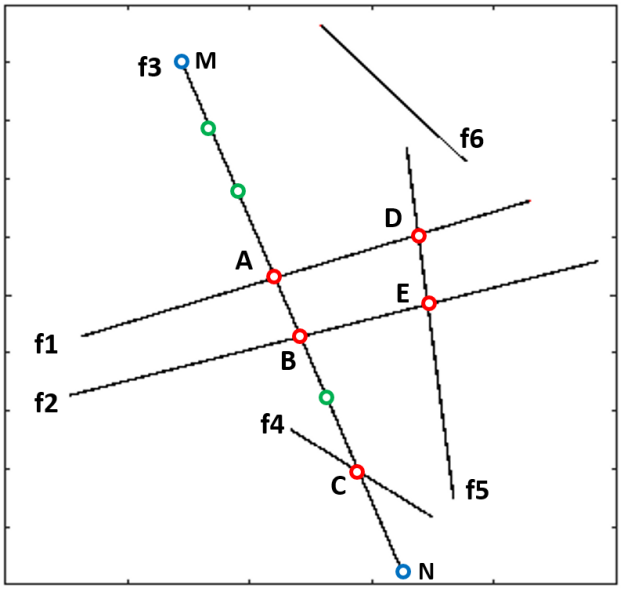

Figure 2.1: Schematic of fracture element generation

The developed algorithm honors the intersections and the end points of each fracture, also is able to adjust the fracture element number and sizes flexibly. Next we will explicitly introduce the techniques we used in the above Procedure (1) and Procedure (3).

For Procedure (1): the fracture intersection between two fractures is determined through the technique introduced by Bourke (1989). Take Fig.2.2 as an example. There are two fractures intersecting. The equations for the two fracture lines (where the two fracture segments belong to) are

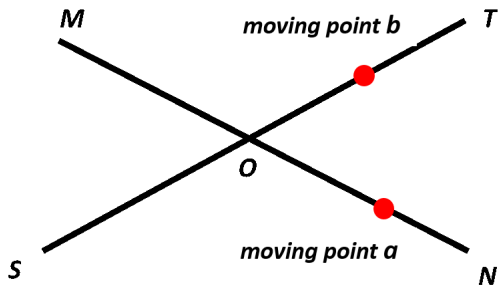

Figure 2.2: Schematic of fracture intersection determination

$$P_a = P_M + u_a(P_N - P_M) \tag{2.9a}$$

$$P_b = P_S + u_b(P_T - P_S) \tag{2.9b}$$

Where P is the coordinate vector corresponding to different subscripts, for example, for 2D Cartesian coordinates, $P_a = (x_a, y_a)$. x_a, y_a are the x, y coordinates of point a. a and b are the two moving points located on line segment MN and line segment ST, respectively. And u_a, u_b are the normalized distances of point a and b to the starting point M and S, respectively. The intersection point O if exists, whose coordinates are represented as:

$$x_o = x_M + u_a^*(x_N - x_M) \tag{2.10a}$$

$$y_o = y_M + u_b^*(y_N - y_M) \tag{2.10b}$$

Where u_a^* and u_b^* are expressed in Eq.(2.11a) and Eq.(2.11b), respectively:

$$u_a^* = \frac{(x_T - x_S)(y_M - y_S) - (y_T - y_S)(x_M - x_S)}{(y_T - y_S)(x_N - x_M) - (x_T - x_S)(y_N - y_M)} \tag{2.11a}$$

$$u_b^* = \frac{(x_N - x_M)(y_M - y_S) - (y_N - y_M)(x_M - x_S)}{(y_T - y_S)(x_N - x_M) - (x_T - x_S)(y_N - y_M)} \tag{2.11b}$$

$$0 \leq u_a^*, u_b^* \leq 1 \tag{2.11c}$$

To make sure the intersection point is located inside the fracture segments, Eq.(2.11c) should be satisfied.

And if the denominators of u_a^* and u_b^* are 0 then the two line segments are parallel, and if the denominator and numerators both are 0 then the two segments are coincident. This technique is applied to all pairs of the fractures in the porous medium to detect the intersection points.

For Procedure (3): After the intersection points being determined, the flexible points need be inserted to generate the fracture elements with suitable sizes. We continue our description using the example in Fig.2.3. Define the fracture segment enclosed by the adjacent fixed points as Subsegment, such as Subsegment M_1A, Subsegment AB in Fig.2.3. In other words, the numbers and the locations of flexible points in the subsegments need be determined. The following techniques are applied:

(a) Scan all the Subsegments in the fracture network and identify the longest Subsegment with its length as L_{max}, such as in Fig.2-3, subsegment M_2B is the longest. Recall in Fig.2.3, the blue circles and the red circles represent the fixed end points and fixed intersection points respectively;

(b) Divide the longest Subsegment into N (a user defined value) equal spaced segments by

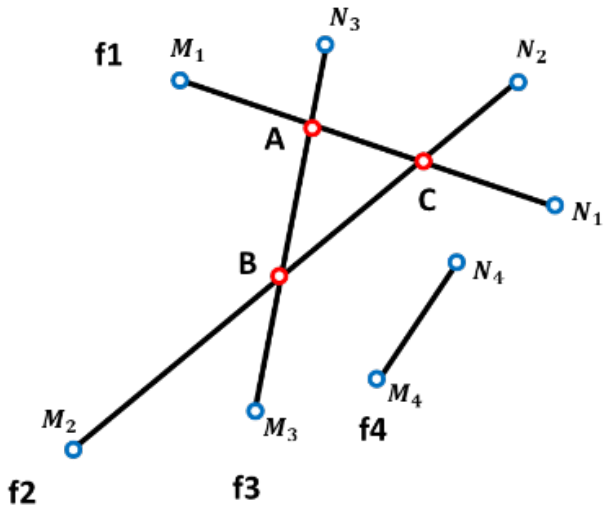

Figure 2.3: Flexible points insertion procedure (a)

inserting $N-1$ flexible points (green circles), with each small segment's length as $\frac{L_{max}}{N}$, such as in Fig.2.4, two flexible points (green circles) are inserted in Subsegment M_2B;

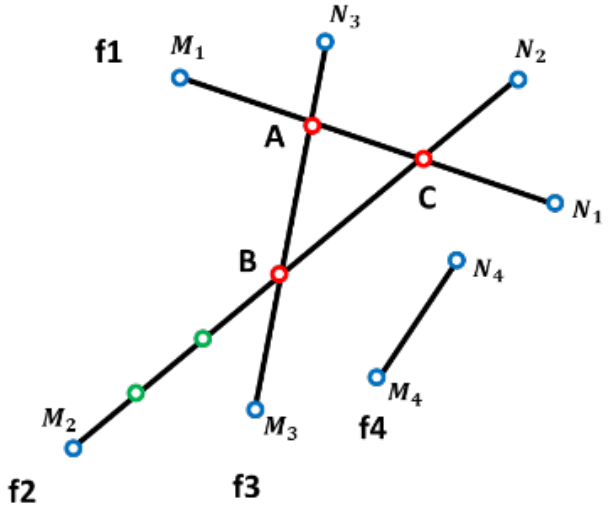

Figure 2.4: Flexible points insertion procedure (b)

(c)$\frac{L_{max}}{N}$ serves as the basic length to divide the remaining Subsegments. For example, if some

Subsegment has length L, and $\frac{L}{L_{max}}N = Q$ with remainder R, then this Subsegment will be divided into Q (if $R = 0$) or $Q + 1$ (if $R > 0$) small elements (with equal length of $\frac{L}{Q+1}$). For example, in Fig.2.5, Subsegment BC and Subsegment M_4N_4 are therefore divided;

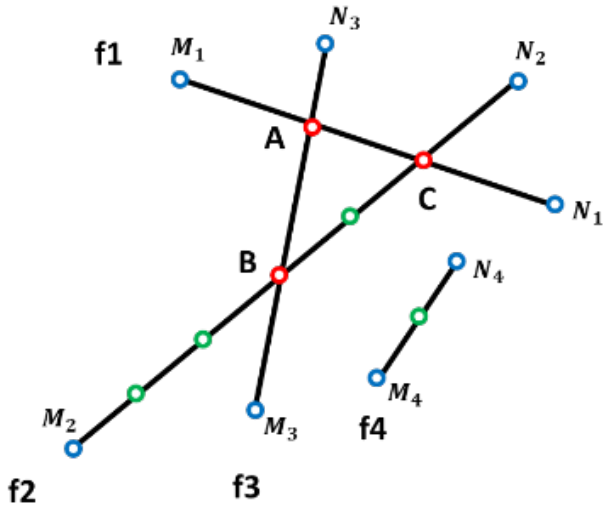

Figure 2.5: Flexible points insertion procedure (c)

(d) The procedure is repeated for all the remaining subsegments, which generates the final discretization, as shown in Fig.2.6.

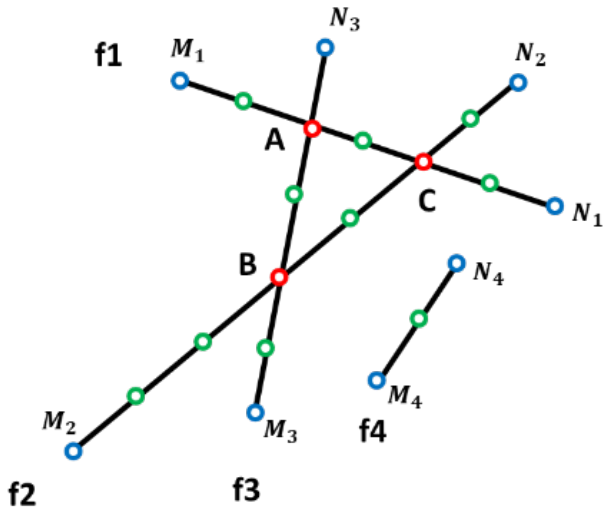

Figure 2.6: Flexible points insertion procedure (d)

The fracture elements generated through this approach will usually have suitable sizes, and the total number of the fracture elements can be reasonably controlled. Fig.2.7 and Fig.2.8 show the discretization examples for a 10 fracture example, where N sets to be 2 and 6 respectively. The first discretization generates 26 fracture elements, while the second discretization generates 56 fracture elements.

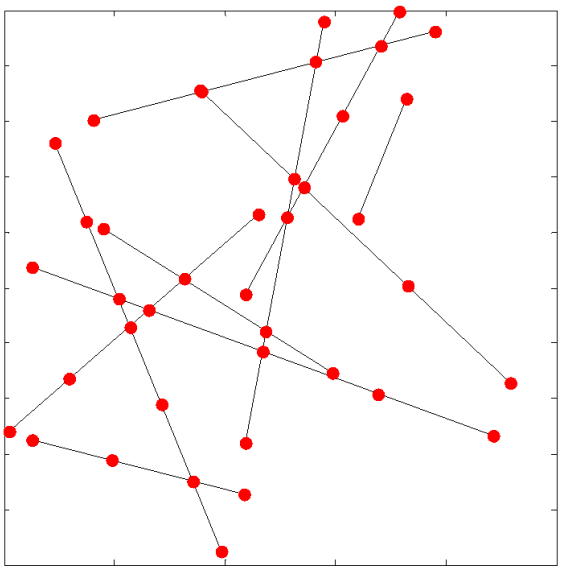

Figure 2.7: Discretization for 10 fractures ($N = 2$)

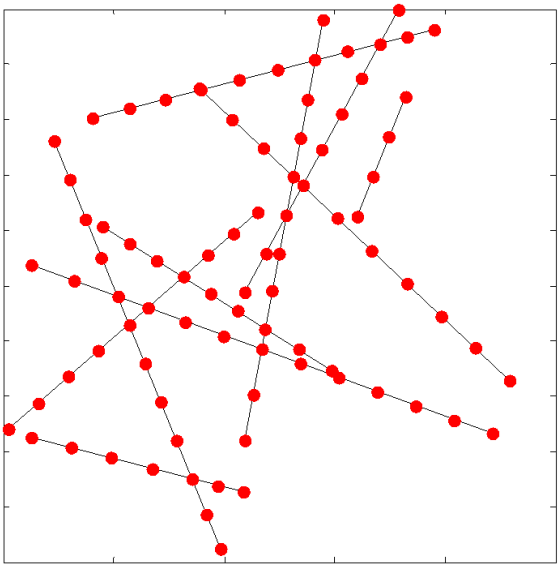

Figure 2.8: Discretization for 10 fractures ($N = 10$)

2.4 Numerical implementation

After the discretization is finished, here we will introduce how to apply the governing equations on the discretized elements and generate the corresponding matrix-vector system of the equations. For illustration, we take Fig.2.9 as an example, which is a simple discretization schematic of a 2D reservoir block with two embedded fractures. The block boundaries and the fractures are discretized into small elements, and each element is closed by two element end points (in triangular, these element end points can be fixed points or flexible points as introduced above.) with the middle points (in circle) selected as the collation points. The fracture elements are generated from the above procedures.

For the boundary elements in Fig.2.9, constant shape function is adopted, which indicates the pressure and the flow rate over each boundary element are set as constants. For each fracture element, a constant source strength Q is assumed. The BEM formed equations (e.g., Eq.(2.3), Eq.(2.6)) are set at the collocation points (red circles) subsequently on both the fracture elements and the boundary elements, and the flow equations (Eq.(2.4) or Eq.(2.8)) are set at the collation points (red circles) and the end points (white triangles) on the fracture elements.

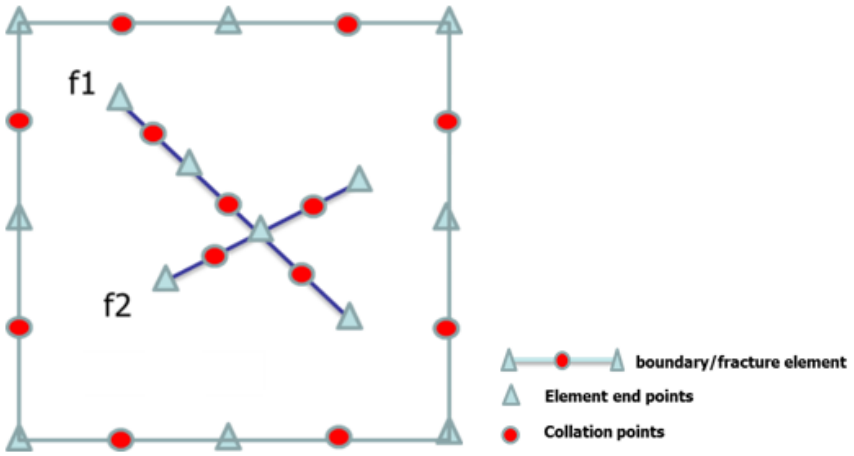

Figure 2.9: Discretization schematic of a reservoir block with two fractures

The matrix-vector system resulting from the above collations has the following block-matrix expressions:

$$\begin{bmatrix} \boldsymbol{A_1} & \boldsymbol{B_1} & \mathbf{0} & \mathbf{0} \\ \boldsymbol{A_2} & \boldsymbol{B_2} & \boldsymbol{C_2} & \mathbf{0} \\ \mathbf{0} & \boldsymbol{B_3} & \boldsymbol{C_3} & \boldsymbol{D_3} \\ \mathbf{0} & \boldsymbol{B_4} & \boldsymbol{C_4} & \boldsymbol{D_4} \end{bmatrix} \begin{bmatrix} \boldsymbol{U} \\ \boldsymbol{Q} \\ \boldsymbol{P_{fm}} \\ \boldsymbol{P_{fe}} \end{bmatrix} = \begin{bmatrix} \boldsymbol{R_1} \\ \boldsymbol{R_2} \\ \boldsymbol{R_3} \\ \mathbf{0} \end{bmatrix} \tag{2.12}$$

The collocated equations are grouped into four separate blocks. The first block comes from collating the BEM formed equations on the boundary collation points, the second block is from collating the BEM formed equations on the fracture collation points, while the third block is from collating the fracture flow equations on the fracture collation points, and the fourth block is from collating the fracture flow equations on the fracture element end points (Notice the difference between fracture element end points and fracture end points). $\boldsymbol{U}$ is an unknown vector with each element being either the pressure or the normal velocity (depending on the given boundary conditions) of the boundary collation points. $\boldsymbol{Q}$ is the vector with each element being the source strength of each fracture element. $\boldsymbol{P_{fm}}$ holds the pressure values on the fracture element collation points, while $\boldsymbol{P_{fe}}$ holds the pressure values on the fracture element end points. Notice $\boldsymbol{C_2}$ is just an identity matrix. Eq.(2.12) can be solved using direct methods or iterative methods. Eq.(2.12) can be further simplified by keeping the first three blocks unchanged, and only collating the fracture flow equations at the fracture end points and the fracture intersections. This will reduce the problem size significantly especially when fracture number is large.

Two aspects regarding to the matrix-vector system assembly and computation are described in the following.

2.4.1 Line integral computation

To compute the first block and second block in Eq.(2.12), the line integrals F_1^k and F_2^k for a collation point (ξ, μ) over a boundary element or fracture element C^k need be computed, where the line integrals are:

$$F_1^{(k)} = \int_{C^k} \Phi(x, y; \xi, \mu) ds(x, y) \tag{2.13a}$$

$$F_2^{(k)} = \int_{C^k} \frac{\partial}{\partial n} \Phi(x, y; \xi, \mu) ds(x, y) \tag{2.13b}$$

Where Φ is the fundamental solution for the two-dimensional Laplace's equation, and its form is as Eq.(2.14a):

$$\Phi(x, y; \xi, \mu) = \frac{1}{4\pi} In[(x - \xi)^2 + (y - \mu)^2] \tag{2.14a}$$

$$\frac{\partial \Phi}{\partial n} = n_x \frac{\partial \Phi}{\partial x} + n_y \frac{\partial \Phi}{\partial y} \tag{2.14b}$$

Where $\dfrac{\partial \Phi}{\partial n}$ is the normal derivative of Φ, and (n_x, n_y) is the unit normal vector of the element C^k.

To compute Eq.(2.13a) and Eq.(2.13b), the approaches outlined in Part 1.6 of Ang (2007) are adopted. Ang (2007) presents the analytical formulations to compute the line integrals. Depending on whether the collation point (ξ, μ) is on the same line of the element segment C^k or not, the formulations are different for both Eq.(2.13a) and Eq.(2.13b) (See Eq.(1.40), Eq.(1.14), and Eq.(1.37), Eq.(1.38) in Ang (2007)). For each collation point, the line integrals over all the fracture and the boundary elements need be computed.

2.4.2 Fracture intersection

When collating flow equations at the fracture intersections, the mass conservation should be conserved considering flow from all intersecting fractures. Take Fig.2.10 as an example, two fractures intersecting at point O, and four fracture elements, which are enclosed by element end points (triangles), form surrounding this intersection and A, B, C, D (blue circles) are the mid-points of the respective elements. The flow equation applied at the intersection O should be in the following form:

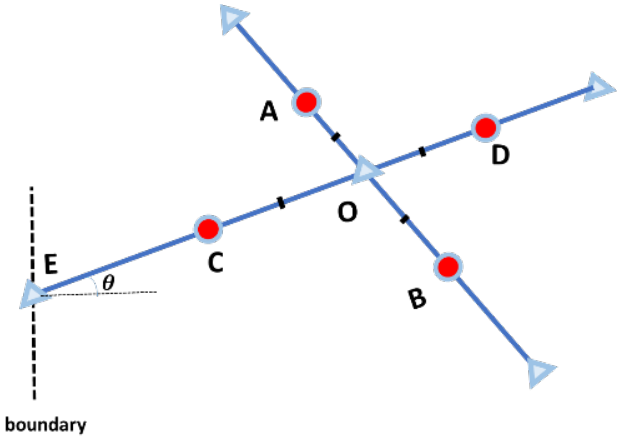

Figure 2.10: Schematic of fracture intersection

$$\sum_{j=A,B,C,D} \frac{k_f w_f}{\mu d_{j,O}} (p_j - p_O) = \frac{1}{2} \sum_{j=A,B,C,D} Q_j d_{j,O} \tag{2.15}$$

Where w_f, k_f, μ are the fracture aperture, fracture permeability and fluid viscosity respectively (here constant fracture permeability and aperture are assumed, but the methodology works for variable fracture permeabilities and apertures), and $d_{j,O}$ is the distance from point j to point O. Q_j and p_j are the element source strength and the pressure associated with the point j, respectively, where $j = A, B, C, D$.

In Eq.(2.15), the left sum represents the net flow from the two intersecting fractures to the controlling region of the intersection point O, and the right sum represents the fluid source of the fracture intersection controlling region to the surrounding matrix. The fracture intersection region includes half (which corresponds to the coefficient of $\frac{1}{2}$ in the right hand side of Eq.(2.15)) of the fracture segments AO, BO, CO, and DO. When multiple fractures intersect at the same point, the same methodology similar to Eq.(2.15) is applied.

Special adjustment should be conducted when the fractures intersecting at the boundaries. For example, in Fig.2.10, one fracture hits the left boundary and the resulting intersection is point E. If the pressure is given for the left boundary, then the pressure at E equals to the given pressure (one unknown in P_{fe} of Eq.(2.12) is thus reduced); if the flow rate is given at the boundary, then

the flow equation collating at point E should be changed into the following form:

$$qw_f cos\theta + \frac{k_f w_f}{\mu d_{C,E}}(p_C - p_E) = \frac{1}{2} Q_C d_{C,E} \tag{2.16}$$

Where q is the given volume flow rate (whose unit is ft^2/s for flow in a 2D porous medium) on that boundary, and $q > 0$ means flow into the matrix, θ is the angle between the fracture and the perpendicular line of the intersecting boundary.

2.5 Examples

2.5.1 Case A

In this case, a square porous medium with two intersecting fractures is considered, see Fig.2.11. The upper and lower boundaries are set as 100 psi and 50 psi, respectively. And the other two boundaries are set as no flow boundaries. This is a case with very simple fracture configurations. The fracture aperture is set as 50 um, and the corresponding fracture permeability is 211 D, and

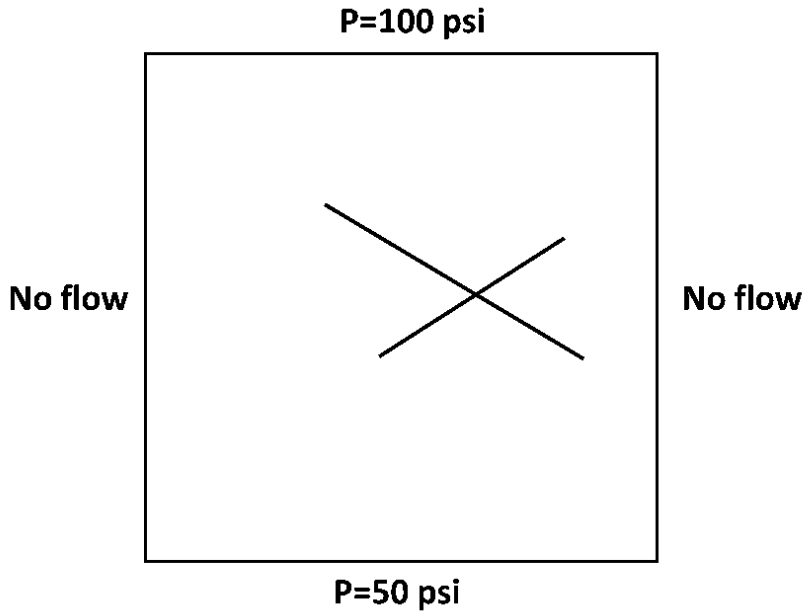

Figure 2.11: Schematic for Example Case A

the matrix permeability is set as 1e-4 md. And the fluid viscosity is 1 cp. We have computed the pressure distribution inside the porous medium through our BEM simulator and compared the results with those from a commercial FEM simulator. Fig.2.12 shows the discretization used in the FEM simulator, where 644 triangles are adopted.

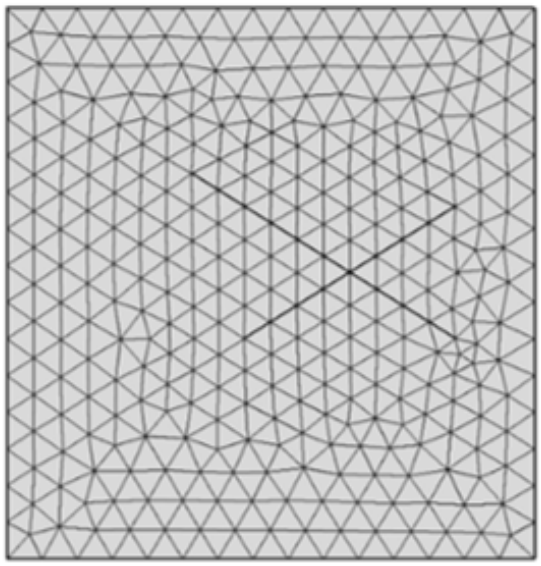

Figure 2.12: FEM Discretization for Example Case A

Different discretization schemes in our BEM simulator. Fig.2.13 shows one example, where 20 boundary elements and 8 fracture elements are contained. The green circles and the numbers on the fractures indicate the fracture element end points and their local indexes; and the red circles and the associated numbers on the boundaries indicate the boundary element end points and their associated boundary indexes (Notice that for fracture intersection point, two fracture local indexes 3 and 8 are allocated. Also, two boundary indexes 1 and 21 are assigned to the same point. The redundant indexes, such as fracture local index 8 and boundary local index 21, are removed in the matrix-vector system assembly).

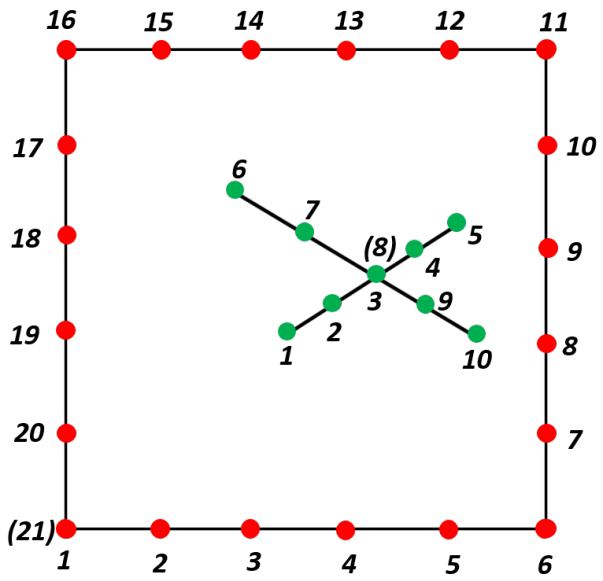

Figure 2.13: Discretization scheme for our simulator

The pressure distributions computed from our simulator (discretization based on Fig.2.13) and the FEM simulator are shown in Fig.2.14 and Fig.2.15 respectively. And we can see the results match each other closely.

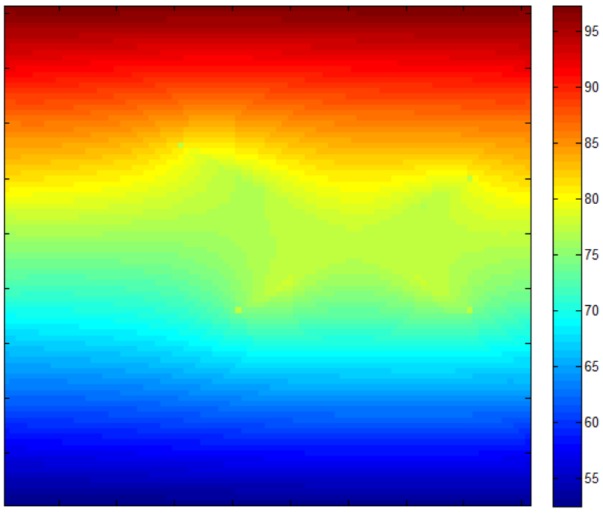

Figure 2.14: Pressure distribution computed from our simulator

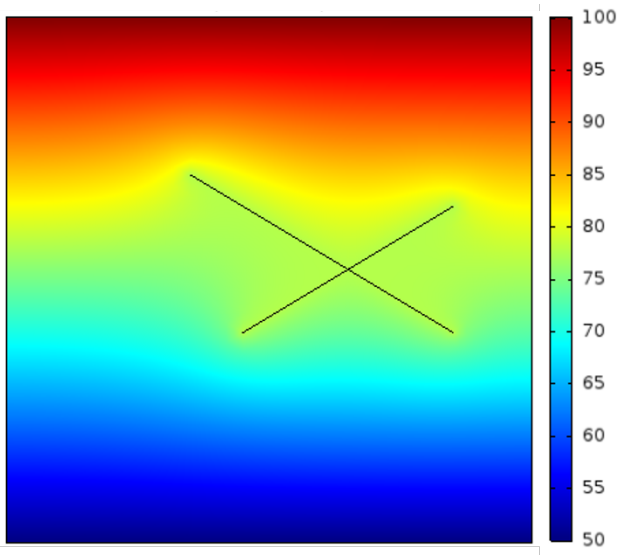

Figure 2.15: Pressure distribution computed from FEM simulator

To quantity the difference, we compare the results at 100 internal points of the square, whose x coordinates are $x = (0.1 \times i - 0.05)L$, and y coordinates are $y = (0.1 \times j - 0.05)L$, where L is the square side length, and $i, j = 1, 2, \cdots, 10$. Fig.2.16 shows the pressures for these 100 points from both simulators. We can see the results are very close with the average relative error is 0.49% and the maximum relative error is 2%.

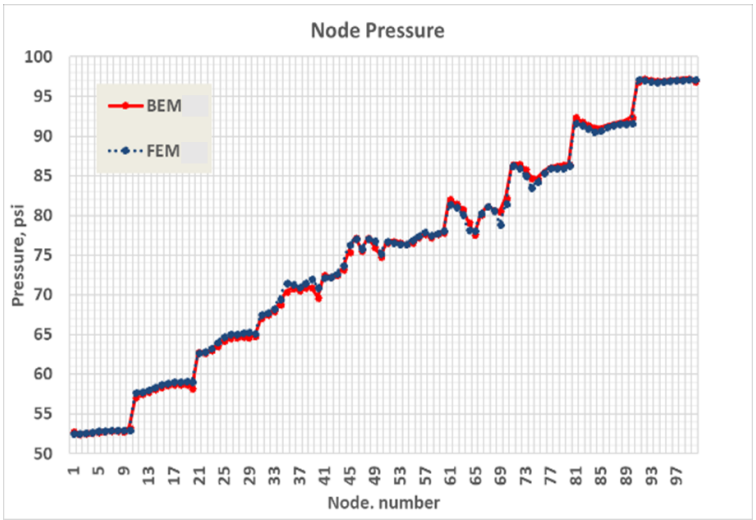

Figure 2.16: Pressure comparison at 100 internal points for Case A

2.5.2 Case B

In this part, we consider another case with more complex fracture configurations in the square porous medium, which is shown in Fig.2.17. There are 8 fractures with different lengths. Among the 8 fractures, 6 fractures intersecting with each other form a connecting network, and 2 fractures are isolated from the others. The same boundary conditions, rock and fluid properties as those in Case A are used.

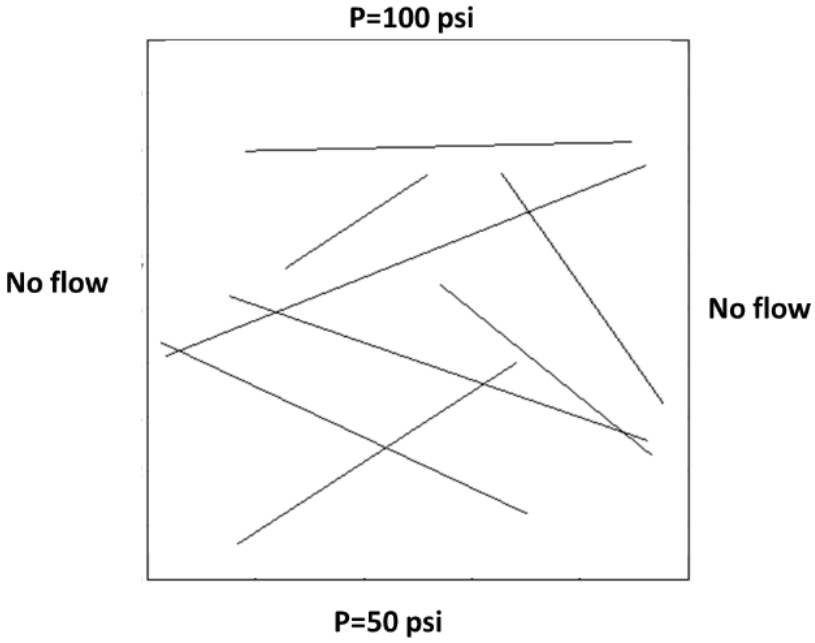

Figure 2.17: Schematic for Case B

Fig.2.18 shows one FEM discretization example for the above fractured porous medium, where 938 triangular elements are generated. We can see that many small triangles needed be placed in the intersections and the endpoints of the fractures. And Fig.2.19 shows the pressure distribution generated from this FEM simulator.

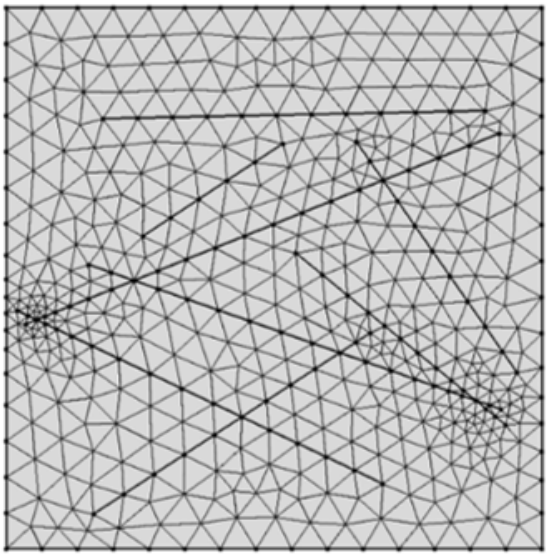

Figure 2.18: FEM Discretization for Example Case B

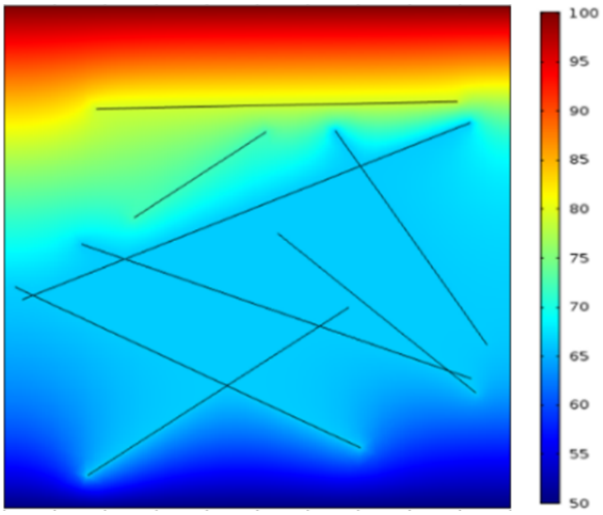

Figure 2.19: Pressure distribution computed from FEM simulator for Case B

Again we have tested different discretization strategies for our simulator. Fig.2.20 and Fig.2.21 are two examples. There are 20 boundary elements, 24 fracture elements, and 20 boundary elements, 40 fracture elements in Fig.2.20 and Fig.2.21, respectively.

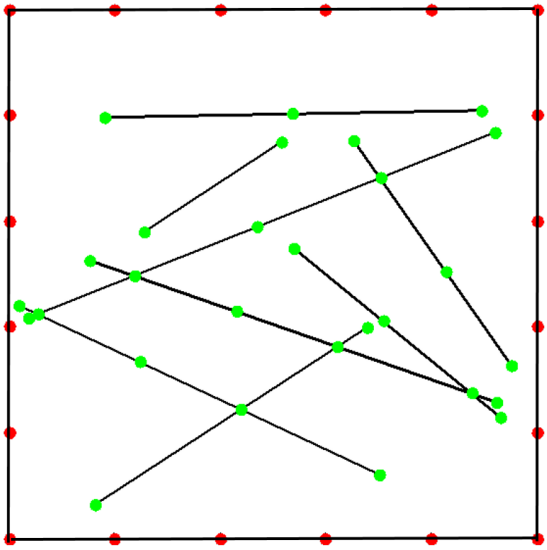

Figure 2.20: Discretization strategy 1 for Case B

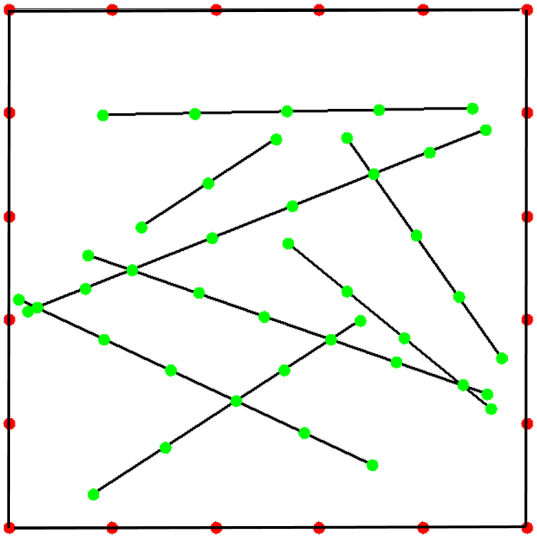

Figure 2.21: Discretization strategy 2 for Case B

The pressure distributions from our simulator are shown in Fig.2.22 and Fig.2.23 respectively, both match Fig.2.19 acceptably, and Fig.2.22 is computed based on the discretization strategy of Fig.2.20 and Fig.2.23 is computed based on Fig.2.21. We can see as the number of the fracture elements increases, the pressure subtleness (especially near the fracture tips and intersections) is

captured more.

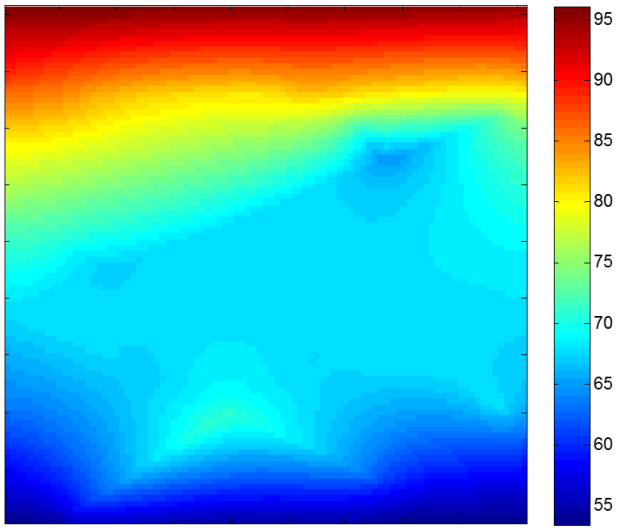

Figure 2.22: Pressure distribution computed from our simulator (Discretization based on Fig.2.20)

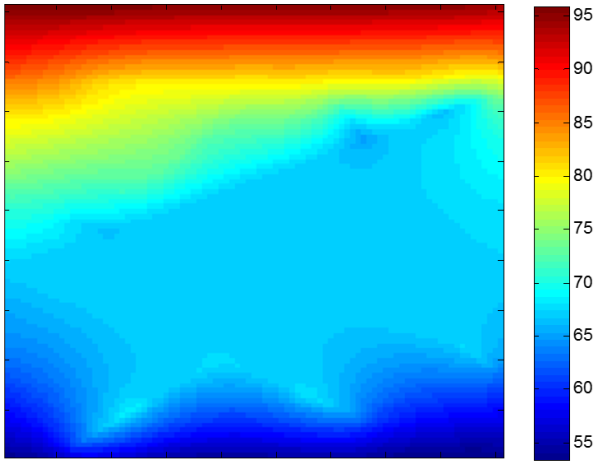

Figure 2.23: Pressure distribution computed from our simulator (Discretization based on Fig.2.21)

Again, we pick up 100 uniformly distributed internal points in the square and compare their pressures. Fig.2.24 shows the results from our simulator and those of the FEM simulator. We can

see that the results from our BEM simulator match that from FEM simulator very well. And as the number of discretized elements increase, the difference between our simulator result and the FEM simulator result decreases, which can be seen by the fact that the blue curve (corresponding to Fig.2.23) is closer to the red curve (corresponding to Fig.2.19) than the green curve (corresponding to Fig.2.22). Comparing the result from our simulator (corresponding to Fig.2.23) with that from the FEM simulator, the average relative error is 1.15% and the maximum relative error is 7.9%. And the accuracy can be increased if more elements are adopted or higher order of shape functions on the elements are used.

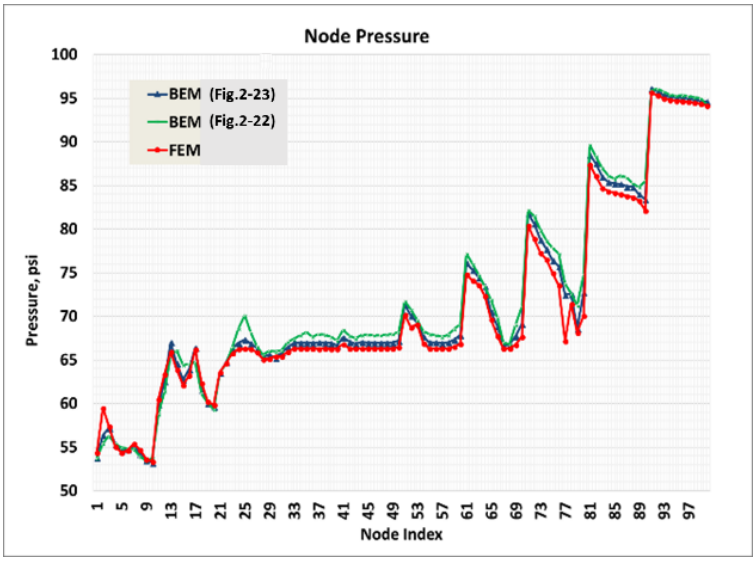

Figure 2.24: Pressure comparison at 100 internal points for Case B

2.5.3 Case C

Different boundary conditions have been developed into our simulator. In this part, we test the Neumann boundary condition in our example.

The porous medium under study is shown in Fig.2.25. The upper and lower boundaries are set as constant pressures of 100 psi and 50 psi, respectively. Fluid flows into the left boundary at a constant flow rate, and the right boundary is set as no flow boundary. The rock and fluid properties

are set the same as those in Case A.

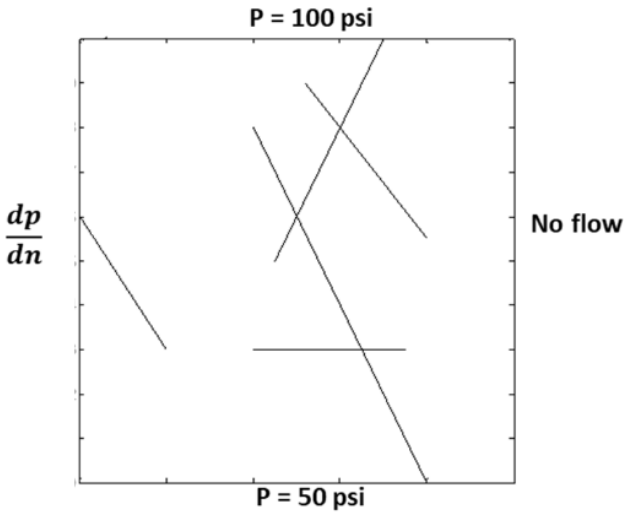

Figure 2.25: Schematic for Example Case C

Fig.2.26 shows the FEM discretization scheme, and there are 684 triangular elements within. Fig.2.27 shows the corresponding BEM discretization scheme, and there are 20 boundary elements and 19 fracture elements.

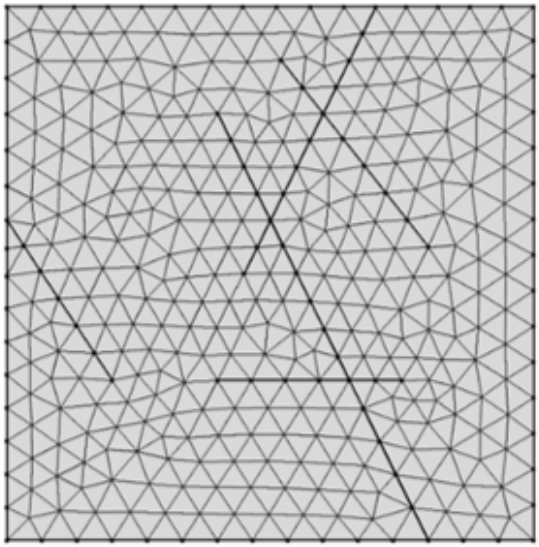

Figure 2.26: FEM Discretization for Case C

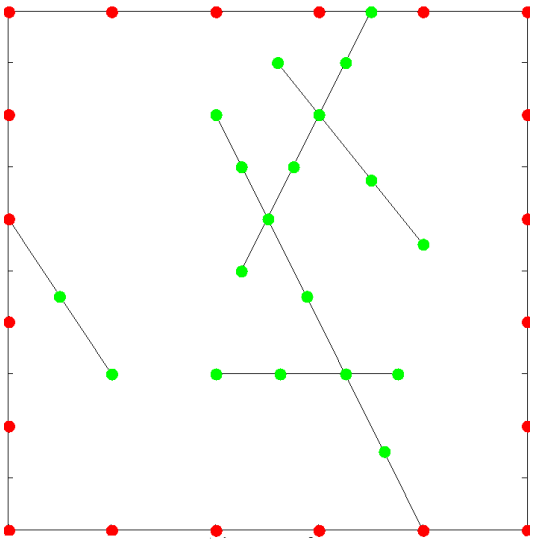

Figure 2.27: Discretization strategy for Case C in our simulator

Three different inflow mass fluxes are considered: (a): 10^{-8} kg/m^2·s; (b): 10^{-7} kg/m^2·s; and (c): 10^{-6} kg/m^2·s. And the pressure distributions calculated from the commercial FEM simulator

are shown in Fig.2.28 to Fig.2.30, respectively. We can see as the inflow rate increases, the average pressure increases. And the pressure maps change significantly for different inflow rates.

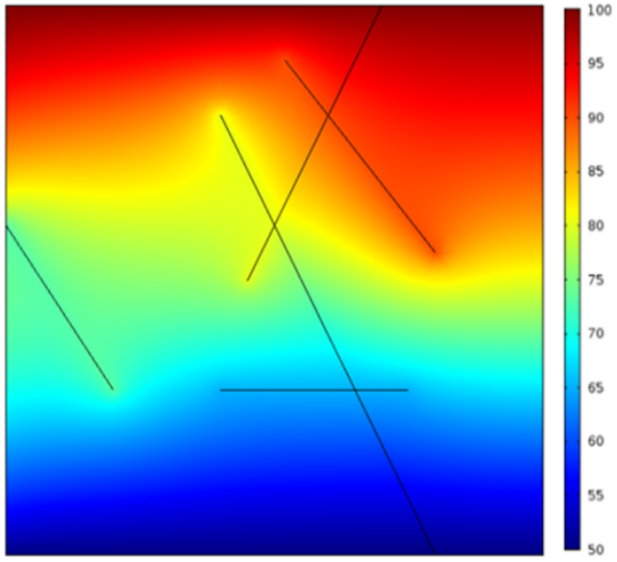

Figure 2.28: Pressure distribution of Case C (10^{-8} kg/m^2·s) from FEM simulator

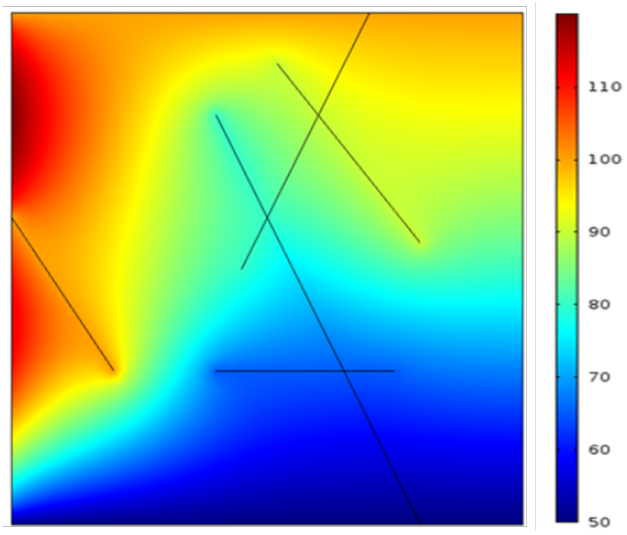

Figure 2.29: Pressure distribution of Case C (10^{-7} kg/m^2·s) from FEM simulator

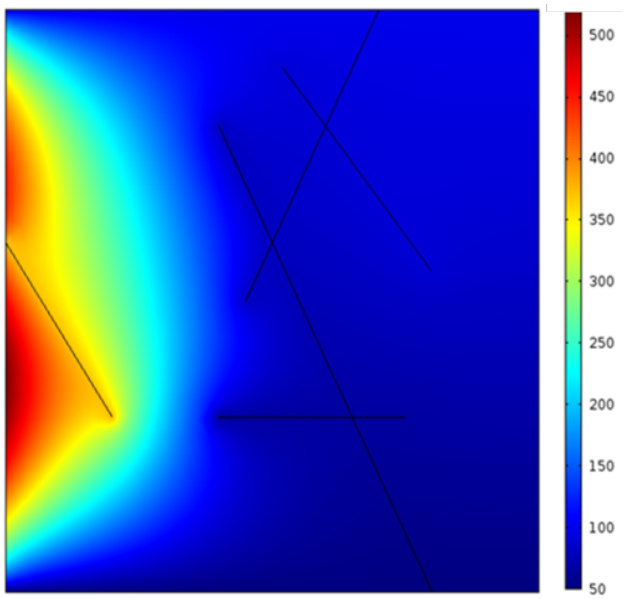

Figure 2.30: Pressure distribution of Case C (10^{-6} kg/m^2·s) from FEM simulator

The results from our BEM simulator are presented as in Fig.2.31 to Fig.2.33 correspondingly. The results from our simulator match those of the FEM simulator very well.

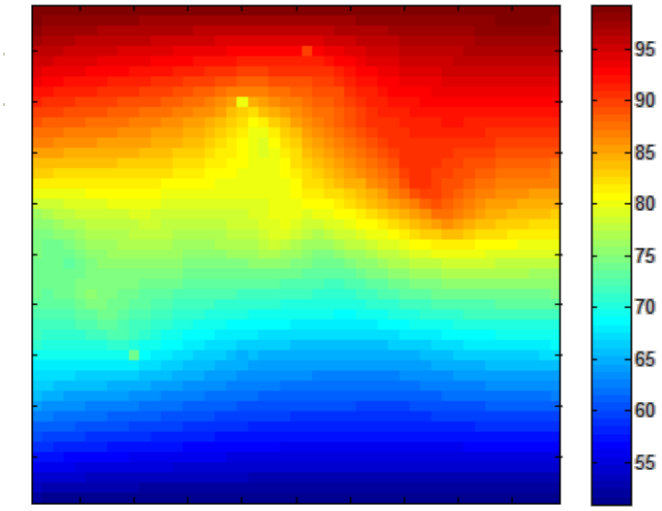

Figure 2.31: Pressure distribution of Case C (10^{-8} kg/m^2·s) from our simulator

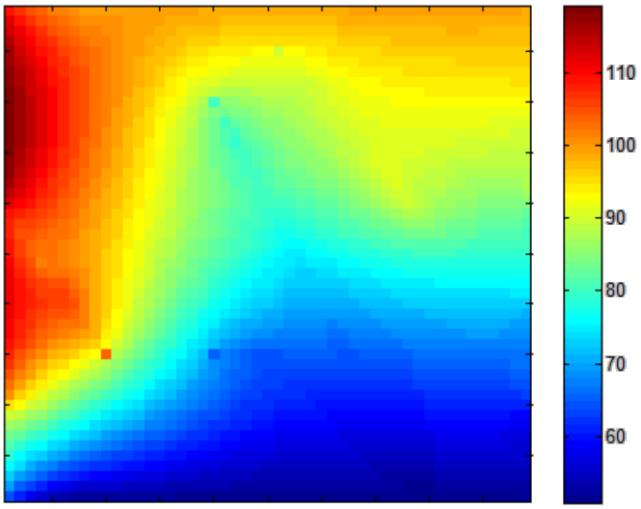

Figure 2.32: Pressure distribution of Case C (10^{-7} kg/m^2·s) from our simulator

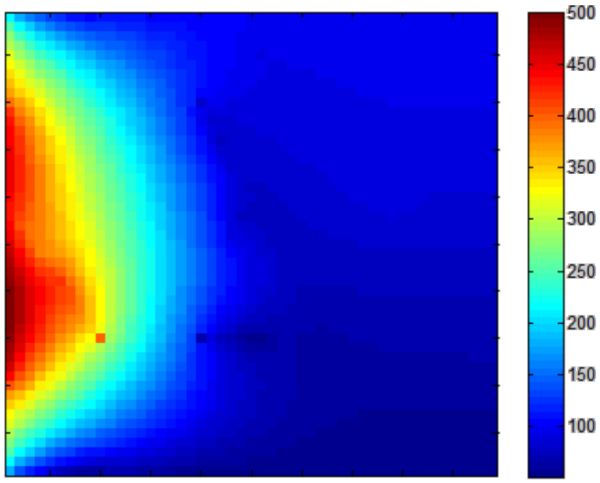

Figure 2.33: Pressure distribution of Case C (10^{-6} kg/m^2·s) from our simulator

Again, 100 internal points (selected as those in Case A) inside the square are selected to compare the results. Fig.2.34 to Fig.2.36 show the comparisons between our results and the FEM results for different inflow rates. For the three inflow rates, the maximum relative errors are 3.2%, 5.1%, 16.6%, and the average relative errors are 0.61%, 0.97%, 2.73%, respectively. The maxi-

mum relative error is a little large at a few points, which can be reduced by increasing the fracture element number and/or adopting higher order shaper function on each element.

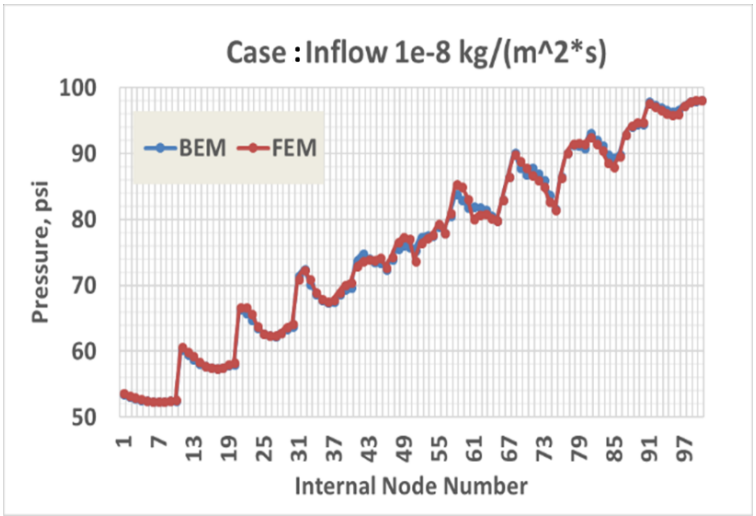

Figure 2.34: Pressure comparison at 100 internal points (10^{-8} kg/m^2·s)

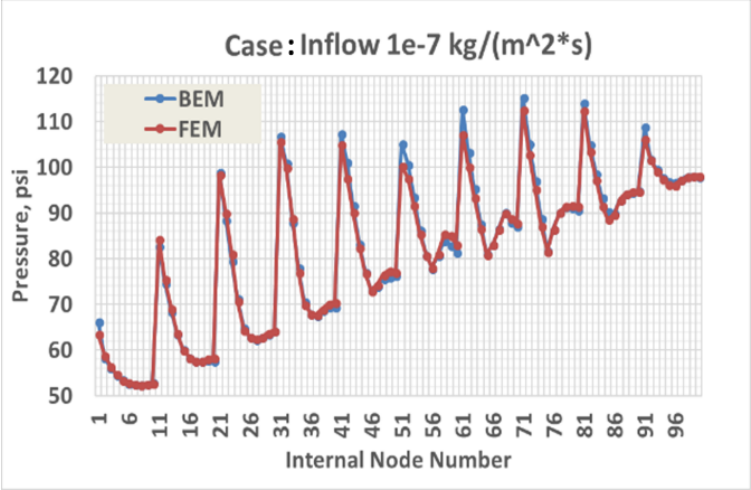

Figure 2.35: Pressure comparison at 100 internal points (10^{-7} kg/m^2·s)

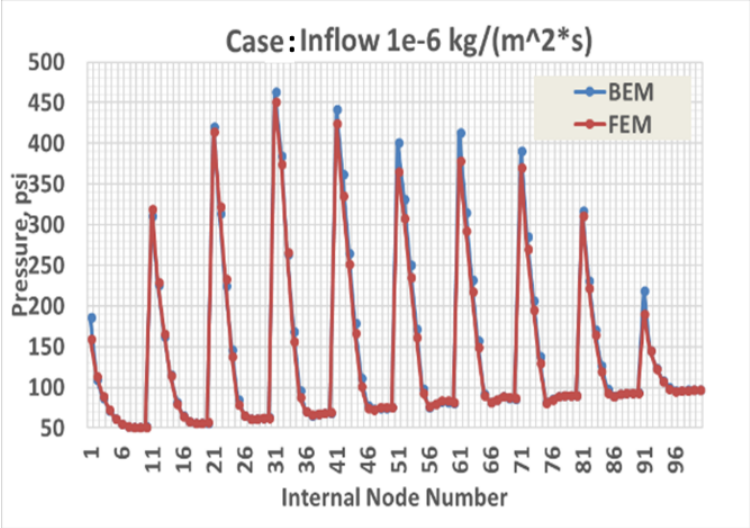

Figure 2.36: Pressure comparison at 100 internal points (10^{-6} kg/m^2·s)

2.5.4 Case D

Our simulator is convenient to simulate flow in curved fractures and handle complex fracture connections. For example, Fig.2.37 shows the pressure map of flow in a porous medium with two curved fractures. And each curved fracture is actually discretized using small straight segments. And the numerical implementation follows the same workflow described above. Fig.2.38 shows the pressure map of three fracture intersecting at a common point. Any number of fractures intersecting at the same point can be handled easily through our simulator. This is an significant improvement comparing to some approaches (Mckoy and Sams, 1997; Mi et al. 2016), where only two-fracture intersection is allowed. Notice in Fig.2.37 and Fig.2.38, the same boundary conditions and relevant properties as those in Case A are assigned. We compared with both results with those from FEM simulators, and the results match very well.

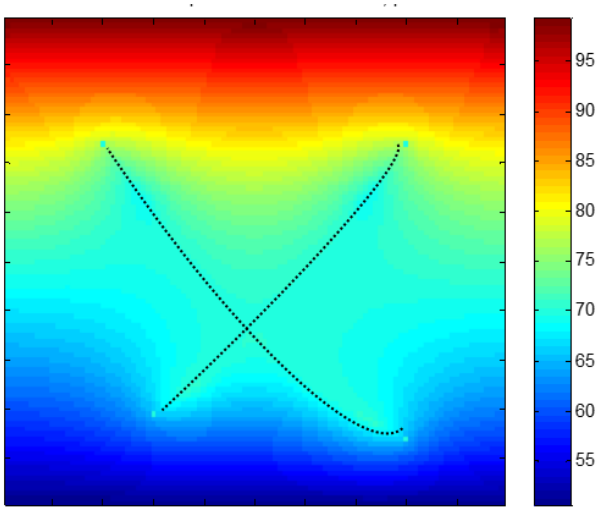

Figure 2.37: Pressure distribution for curved fracture case from our simulator

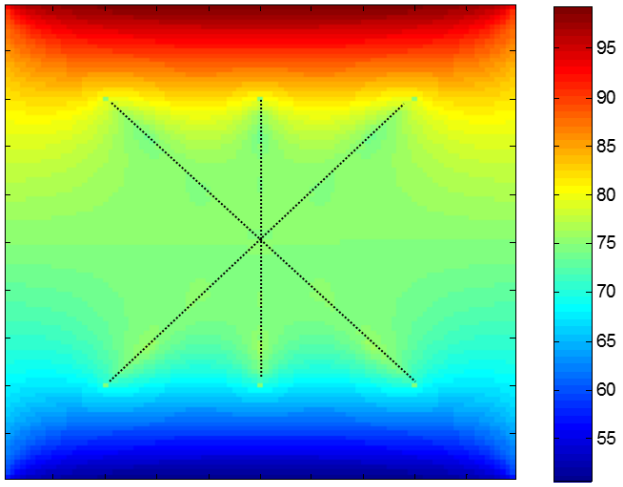

Figure 2.38: Pressure distribution for three fracture intersecting at the same point from our simulator

2.6 Conclusions

(1) Novel 2D fractured reservoir modeling technique based on improved boundary element method has been developed. Our technique has more compacted and efficient formulations comparing with previous research;

(2) General and flexible 2D fracture discretization algorithm is developed, which can readily discretize the complex fracture networks and generate suitable number and appropriate sizes of fracture elements. This procedure is much simplified comparing with other approaches (FEM or FDM). The more complex the fracture network, the more convenient our approach;

(3) The feasibility and accuracy of our simulator in modeling 2D steady flow in fractured reservoirs have been verified;

(4) Modules handling different boundary conditions have been incorporated in our simulator and verified through cases;

(5) Our simulator is convenient to simulate flow in curved fractures and handle complex fracture connections.

3. FLOW SIMULATION OF TRANSIENTNESS AND HETEROGENEITY IN FRACTURED RESERVOIR*

In this section, modules characterizing the transient flow dynamics and the matrix heterogeneity influence on fluid flow in fractured reservoirs are presented. First, the underlying mathematical background and the numerical implementation are introduced. Then, several cases verifying the feasibility and accuracy of our models are presented. Finally, the discussions and conclusions are presented. To the best of our knowledge, no previous research has been conducted to simulate fluid flow concerning transientness and heterogeneity in fractured reservoir through a BEM perspective.

3.1 DRBEM basics

For problems with non-linearity and/or heterogeneity, the fundamental solution is usually hard to find, if not impossible, and they generally introduce volume integrals which require volume discretization before the solution can be attempted. One technique for treating the volume integral without discretizing the volume is the dual-reciprocity boundary element method (DRBEM). In DRBEM, a series of interpolation functions is applied to approximate the integrand, which converts the associated domain integrals into boundary integrals only (Zhang et al. 1994). Instead of discretizing the volume into meshes, unknowns at chosen points inside the domain are involved in the linear algebraic equations approximating the problem being considered. Take Poisson's equation as an example:

$$\bigtriangledown^2 p = b(x, y) \tag{3.1}$$

The boundary integral equations (BIE) corresponding to Eq.(3.1) is as following:

$$c(\xi)p(\xi) + \int_\Gamma (p\frac{\partial G}{\partial n} - G\frac{\partial p}{\partial n})d\Gamma = -\int_\Omega bGd\Omega \tag{3.2}$$

*Part of this section is reprinted with permission from "An Improved Boundary Element Method for Modeling Fluid Flow through Fractured Porous Medium" by Y. Cao, and J. E. Killough, 2017. SPE Proceedings, Copyright [2017] by Society of Petroleum Engineers.

Notice the existence of the domain integral on the right hand of Eq.(3.2). The other nomenclatures follows the definitions of Eq.(2.2). The domain integral can be avoided by setting

$$b = \sum_{j=1}^{N+L} \alpha_j f_j \tag{3.3}$$

Where α_j are initially unknown weights and can be determined from collocation, f_j are the known interpolation basis functions, N and L are the number of boundary nodes and internal nodes, respectively. The use of the internal nodes improves the accuracy of the DRBEM, yet no internal gridding is involved (Archer 2000). The basis function f_j must be the Laplacian of the other function $\hat{p}_j$:

$$\bigtriangledown^2 \hat{p}_j = f_j \tag{3.4}$$

Therefore, Eq.(3.2) evolves into the following form:

$$c(\xi)p(\xi) + \int_\Gamma (p\frac{\partial G}{\partial n} - G\frac{\partial p}{\partial n})d\Gamma = \sum_{j=1}^{N+L} \alpha_j [c\hat{p}_j + \int_\Gamma (\hat{p}_j \frac{\partial G}{\partial n} - G\frac{\partial \hat{p}_j}{\partial n})d\Gamma] \tag{3.5}$$

Applying Eq.(3.5) at the $N + L$ boundary nodes and internal nodes subsequently, the same number of equations as that of the unknowns will be acquired. The detailed methodologies and algorithms of the DRBEM can be found in Archer (2000), Gaul et al. (2003), and Partridge et al. (1991).

3.2 Governing equations

Eq.(2.3) and Eq.(2.4) are still the governing equations for this chapter. Special treatments need be implemented for Eq.(2.3) to deal with transientness and heterogeneity in fractured reservoirs. For transient flow in fractured reservoirs with heterogeneous matrix, k_m in the left hand side of Eq.(2.3) needs be moved out to form a Laplace operator. Here we use the technique proposed by

El Harrouni et al. (1996), Eq.(2.3) becomes

$$\bigtriangledown^2 u = k_m^{'} u + \frac{\Phi \mu c_t}{k_m} \frac{\partial u}{\partial t} + \frac{\mu}{\sqrt{k_m}} \int_f Q(\vec{z}) \delta(\vec{x} - \vec{z}) dA \tag{3.6}$$

And

$$u = \sqrt{k_m} p \tag{3.7a}$$

$$k_m^{'} = \frac{\bigtriangledown^2 \sqrt{k_m}}{\sqrt{k_m}} \tag{3.7b}$$

$$u = (1 - \theta_u) u^m + \theta_u u^{m+1} \tag{3.7c}$$

$$q = (1 - \theta_q) q^m + \theta_q q^{m+1} \tag{3.7d}$$

$$\frac{\partial u}{\partial t} = \frac{1}{\triangle t} (u^{m+1} - u^m) \tag{3.7e}$$

Notice that a new variable u (Eq.3.7a) has been defined, and the given boundary conditions are adjusted accordingly. The solution of p can be back calculated from Eq.(3.7a) once u is solved. The first two terms on the right hand side of Eq.(3.6) require the application of DRBEM. The transient term needs special treatment. Here we adopt a two-level time integration scheme for the variation of u and q (Partridge et al., 1991), such as Eq.(3.7c) to Eq.(3.7e), where q refers to the normal derivative of the transformed pressure u, the indices m and m+1 correspond to time steps, θ_u, θ_q are time integration scheme coefficients, $\theta_u = 1$, $\theta_q = 1$ correspond to a fully implicit formulation.

The final DRBEM formulation in matrix form for this case is

$$\begin{aligned} (\frac{1}{\triangle t} C\gamma + \theta_u A - \theta_u C k_m^{'}) u^{m+1} - \theta_q B q^{m+1} = & (\frac{1}{\triangle t} C\gamma - (1 - \theta_u) A + (1 - \theta_u) C k_m^{'}) u^m \\ & + (1 - \theta_q) B q^m + D Q^{m+1} \end{aligned} \tag{3.8}$$

Where A, B are coefficient matrices from collation, $C = (A\hat{U} - B\hat{Q}) F^{-1}$, $\gamma = (\phi \mu c_t)/k_m$, Q is the source strength vector at the collation points of the fracture elements, D is the coefficient

matrix originated from collation of the 3rd term of the right hand side of Eq.(3.6). Archer derived a similar DRBEM formulation (Eq.(2.70) in Archer (2000)) without considering the last term.

3.3 Numerical implementation

The discretization scheme for the transient flow and heterogeneous matrix reservoirs is similar to that of the steady state flow in homogeneous reservoirs. Besides the block boundaries and the fracture surfaces need be discretized, when the reservoir heterogeneity and the transient flow are involved, additional internal points are required for computation using DRBEM. Fig.3.1 is a simple discretization schematic for a 2D reservoir block with two embedded fractures. The block boundaries and the fractures are discretized into small elements, and each element is closed by two element end points (in triangular) with the middle points (in circle) selected as the collation points. The additional internal points for DRBEM are represented by the stars. The locations of the internal points are selected by the users, as those stars shown in Fig.3.1. In our case studies, we usually take the internal points as uniformly distributed inside the square.

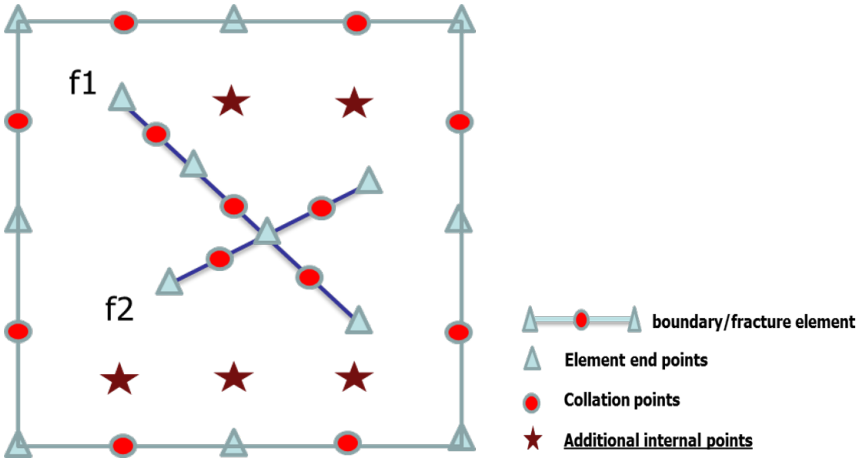

Figure 3.1: Discretization schematic of a reservoir block with two fractures

The BEM/DRBEM formed equations (Eq.(3.8)) will be set at the collocation points and the additional internal points respectively, and the flow equations (Eq.(2.4)) will be set at the collation

points and the end points on the fracture elements. The matrix-vector system resulting from the above collations has the following block-matrix expressions:

$$\begin{bmatrix} \boldsymbol{A_1} & \boldsymbol{B_1} & \mathbf{0} & \mathbf{0} \\ \boldsymbol{A_2} & \boldsymbol{B_2} & \boldsymbol{C_2} & \mathbf{0} \\ \mathbf{0} & \boldsymbol{B_3} & \boldsymbol{C_3} & \boldsymbol{D_3} \\ \mathbf{0} & \boldsymbol{B_4} & \boldsymbol{C_4} & \boldsymbol{d_4} \end{bmatrix} \begin{bmatrix} \boldsymbol{U} \\ \boldsymbol{Q} \\ \boldsymbol{P_{fm}} \\ \boldsymbol{P_{fe}} \end{bmatrix} = \begin{bmatrix} \boldsymbol{R_1} \\ \boldsymbol{R_2} \\ \boldsymbol{R_3} \\ \mathbf{0} \end{bmatrix} \tag{3.9}$$

This is the very same form as Eq.(2.12) in Section 2. The only difference is that the first block contains not only the boundary collation points but also the internal points. The assembly and computation of Eq.(3.9) follows the same approaches outlined in Section 2.

3.4 Examples

3.4.1 Transient case without fractures

First, we would like to verify our DRBEM code for the cases without fractures. A rectangular homogeneous porous medium with unit length is tested, see Fig.3.2. The governing flow equation is as the following:

$$\bigtriangledown \cdot (k \bigtriangledown p) = \phi \mu c_t \frac{\partial p}{\partial t} \tag{3.10}$$

And since the matrix is homogeneous, and the above equation can be simplified as

$$\frac{\partial p}{\partial t} = \bigtriangledown \cdot (\gamma \bigtriangledown p) \tag{3.11}$$

Where $\gamma = \dfrac{k}{\phi \mu c_t}$. We design cases like those described in J. Crank (1975), and compare our results with theirs. Fig.3.3 represents the concentration distribution C for different locations of a circular porous medium at different times, where C_i, C_o are the given initial concentration and the boundary concentration, respectively. The different curves are classified by $\dfrac{Dt}{a^2}$, where D is the diffusion coefficient, t is the time and a is the radius of the circular porous medium. Although

Fig.3.3 is describing for diffusion effects, considering the mathematical equivalence between the flow problem (Eq.(3.11)) and the diffusion problem (Eq.(5.1) in J. Crank (1975)), it also represents the pressure distributions at different times.

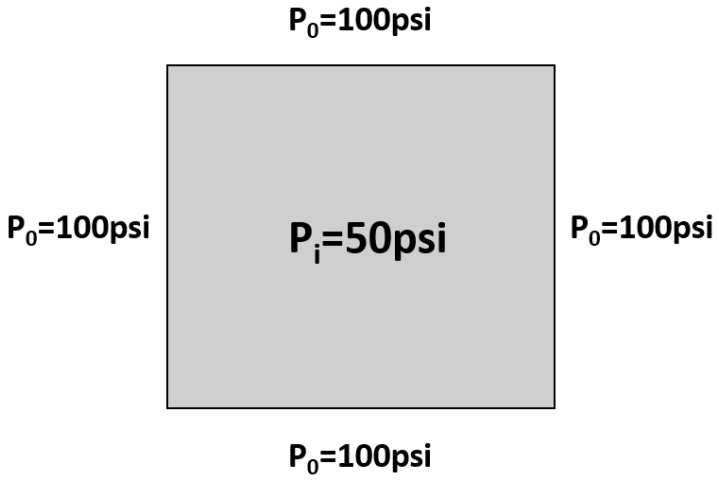

Figure 3.2: A rectangular homogeneous porous medium (no fracture)

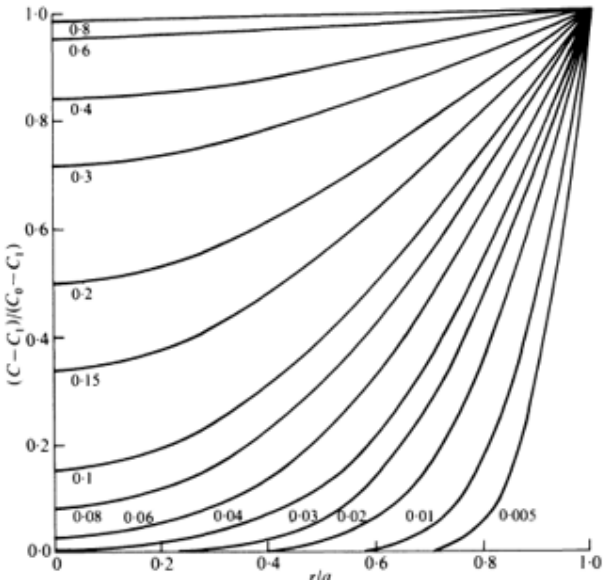

Figure 3.3: Concentration distribution at various times. Reprinted from Fig.5.3 in J. Crank (1975)

The relevant parameters adopted in our flow simulation of Fig.3.2 are: the permeability k, porosity ϕ, viscosity μ, and the total compressibility c_t are set as 0.1 md, 0.05, 1 cp, and 4.4e-6 psi^{-1}, respectively. And the boundary pressure p_0 is set 100 psi constant, the initial pressure p_i is set as 50 psi. For the DRBEM computation, 80 boundary elements, and 100 internal points, which are uniformly distributed inside the square, are selected.

Here we convert the square porous medium (Fig.3.2) to an equivalent circle (whose equivalent radius a_e is $\frac{1}{\sqrt{\pi}}$) and present the pressure distributions at different times for this circle. The pressures for t=1s, 3s, 14s, 28s (The corresponding dimensionless times $t_D = \frac{\gamma t}{a_e^2}$ are 0.014, 0.043, 0.2 and 0.4, respectively) along the radius of the equivalent circle are shown in Fig.3.4. The results are compared with the analytical solutions taken from Fig.3.3. We can see that the results for t_D = 0.043, 0.2 and 0.4 match very well, and the difference for t_D = 0.014 seem a little large, that is due to that the compared analytical solution is for t_D = 0.01 instead of t_D = 0.014. Anyway, by comparing with the analytical solutions, Fig.3.4 validates the accuracy of our simulator in simulating transient flow in porous medium without fractures.

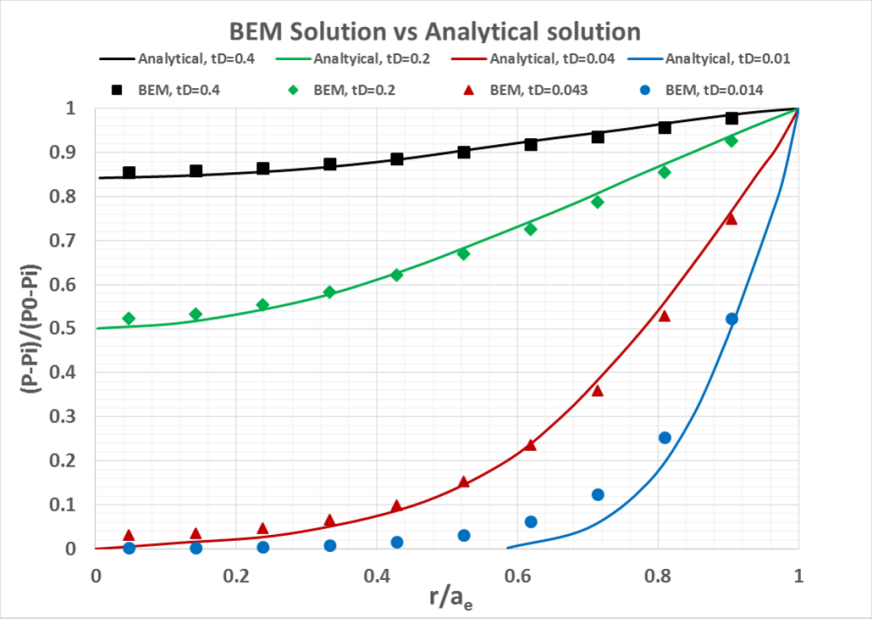

Figure 3.4: Pressure distribution comparison: BEM solution vs analytical solution

3.4.2 Transient case with fractures

Here we test our simulator for handling transient flow in porous medium with fractures. In addition, we will change the parameter settings and see the influence of the relevant parameters on pressure propagation and fluid flow.

A rectangular porous medium with three fractures contained are studied, among which two of them are intersecting with each other, and the specific configuration is shown in Fig.3.5.

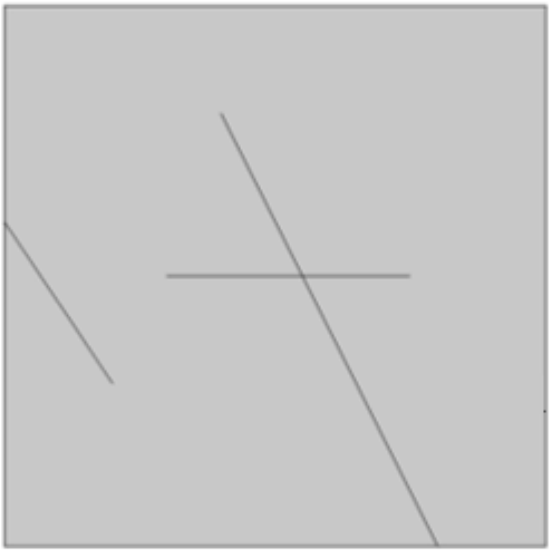

Figure 3.5: Fracture configurations in a block porous medium

The initial pressure in the domain is 100 psi, and the boundary pressure is kept constant as 50 psi. Single-phase fluid water is simulated with the constant density 62.4 lb/ft^3 and the constant viscosity 1 cp. The total compressibility is 3e-6 psi^{-1}. The fracture porosity and matrix porosity are set as 1 and 0.05 respectively. We set the fracture aperture as 1.64e-5 ft, according to the cubic law the fracture permeability is 2.11e5 md, and the matrix permeability is set as 0.1 md.

To verify our simulation code, the results from our simulator are compared with those from a commercial finite element method (FEM) software. Fig.3.6 shows the the domain discretization scheme in the FEM simulator, where 641 triangular elements are contained. The whole medium

can be depleted in about 10 seconds. Three representative pressure distribution results from the FEM simulator are shown in Fig.3.7 to Fig.3.9, and the figures correspond to results at 1 s, 3 s , and 5 s, respectively.

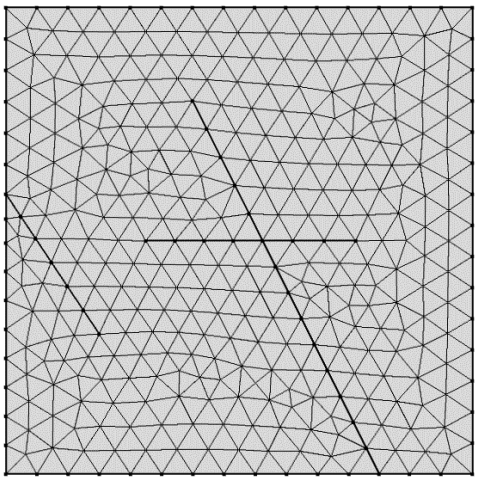

Figure 3.6: Domain discretization for Case in Fig.3.5

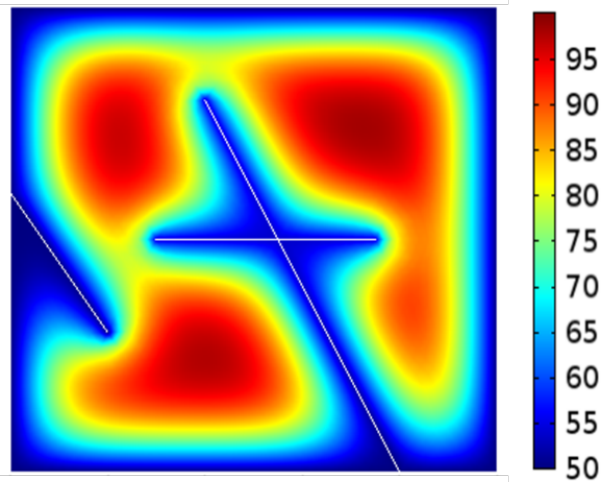

Figure 3.7: Pressure distribution at t=1 s for Case in Fig.3.5 (FEM simulator)

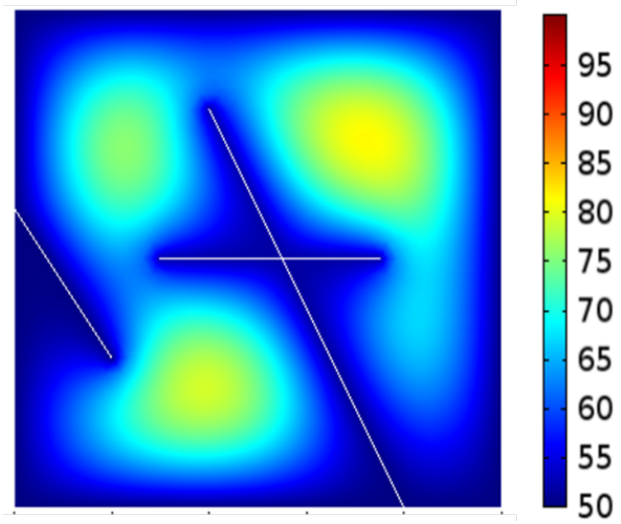

Figure 3.8: Pressure distribution at t=3 s for Case in Fig.3.5 (FEM simulator)

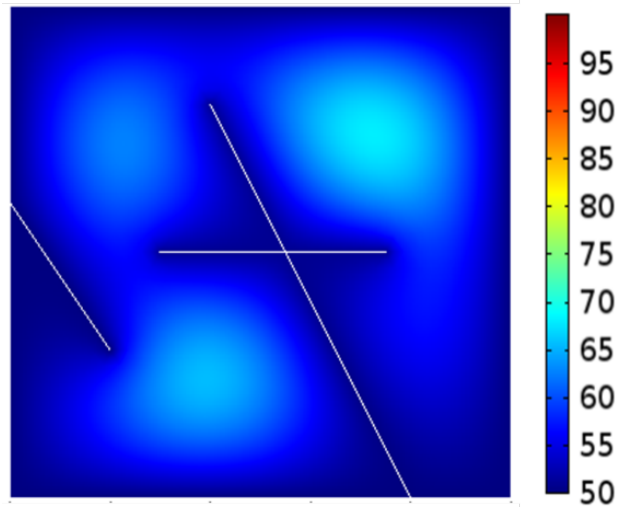

Figure 3.9: Pressure distribution at t=5 s for Case in Fig.3.5 (FEM simulator)

In our DRBEM simulator, the fractures are discretized as shown in Fig.3.10, where in total 32 elements are discretized on the fractures. Besides, 80 boundary elements, and 81 internal points (the stars in Fig.3.10), which are uniformly distributed inside the square, are selected, and the time step increment is 0.1 s. By the way, to avoid the formation of singular matrix, the internal points coinciding with the fracture element collation points or the fracture element end points are disregarded. The pressure distributions from our DRBEM simulator corresponding to Fig.3.7 to

Fig.3.9 are shown in Fig.3.11 to Fig.3.13, and the results match Fig.3.7 to Fig.3.9 very well.

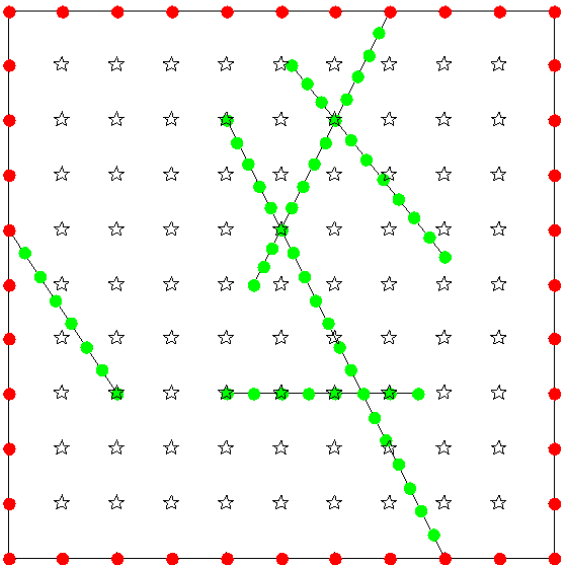

Figure 3.10: Domain discretization for Case in Fig.3.5

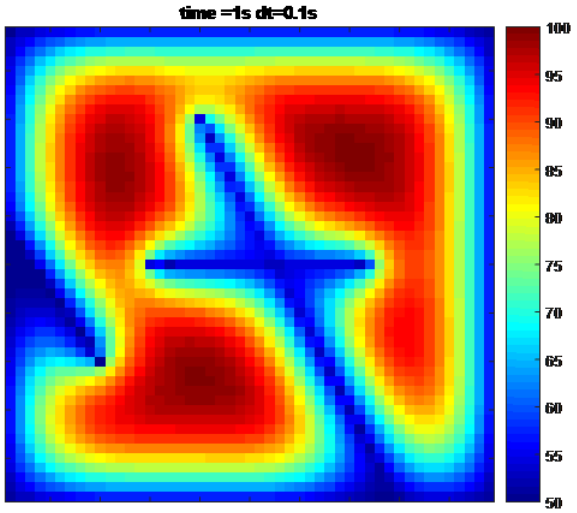

Figure 3.11: Pressure distribution at t=1 s for Case in Fig.3.5 (our simulator)

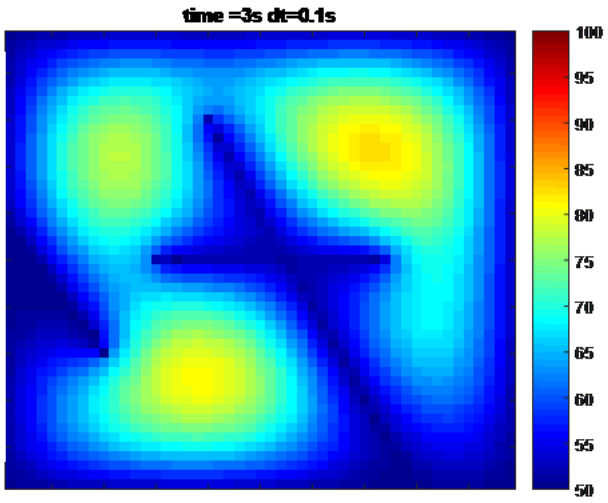

Figure 3.12: Pressure distribution at t=3 s for Case in Fig.3.5 (our simulator)

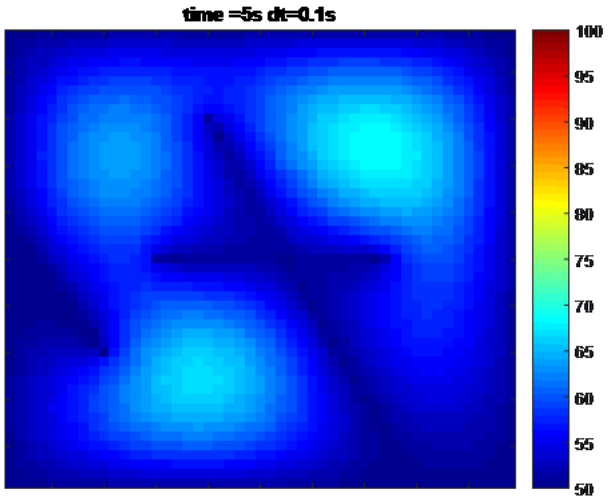

Figure 3.13: Pressure distribution at t=5 s for Case in Fig.3.5 (our simulator)

Here we quantitatively analyze the difference between our results and those from the FEM simulator. The relative error is defined as

$$\epsilon = \frac{|p_{BEM} - p_{FEM}|}{p_{BEM}} \tag{3.12}$$

Where p_{FEM}, p_{BEM} are the pressures calculated from our DRBEM simulator and the FEM simulator, respectively. Pressures at 361 internal points uniformly distributed in the domain (whose x coordinates as $x = \frac{i}{20}L$, y coordinates as $y = \frac{j}{20}L$, where L is the square side length, and $i, j = 1, 2, \cdots, 19$) are computed and compared. The maximum relative error at these points for the first 5 seconds are shown in Fig.3.14. We can see that the maximum relative error decreases as time goes on, and for t =1 s, the maximum relative error is 8.9%, which is quite acceptable. Also, the average and the standard deviation for the 361 relative errors are 1.98% and 1.71% respectively, which indicates a good relative error distribution. This comparison validates our BEM model. The comparably large relative errors locates around the fracture tips (see Fig.3.15), and from experience, we notice that if more fracture elements (especially near the fracture tips or intersections) or higher order shape functions on the fracture elements are implemented, these relative errors can be decreased.

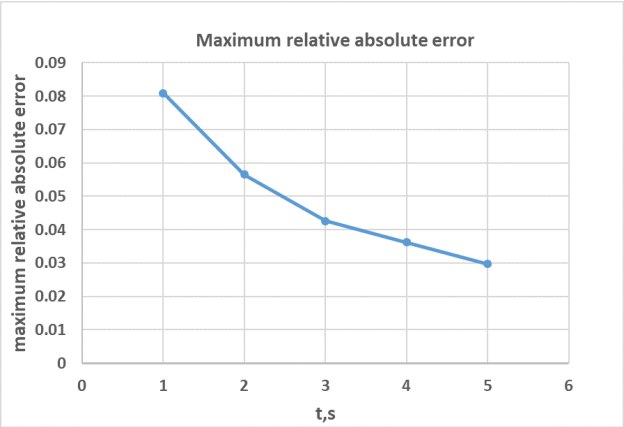

Figure 3.14: Maximum relative error comparison for Case in Fig.3.5

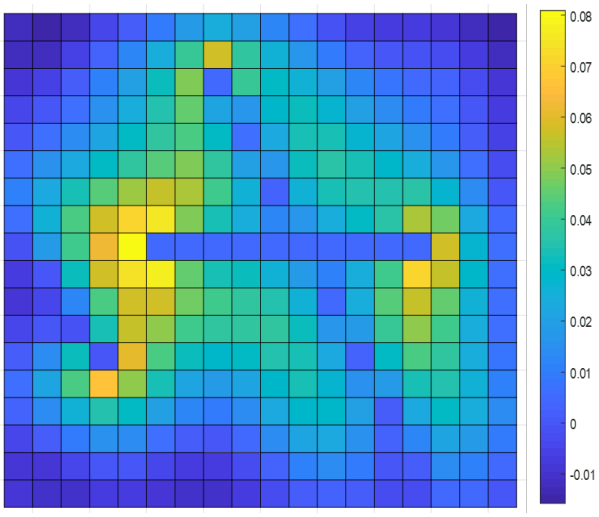

Figure 3.15: Relative error distribution for Case in Fig.3.5

3.4.3 Sensitivity parameter analysis

In this part, the influences of the relevant parameters on the pressure distribution and the fluid flow dynamics are studied using our DRBEM simulator. Each time, one parameter is investigated while keeping the other parameters unchanged. Expect for parameters explicitly mentioned, the other parameters are set as the same as those in Part 3.4.2. The parameters investigated here include the matrix permeability, the fracture permeability and the fluid viscosity.

First, the influence of the matrix permeability is studied. As the matrix permeability decreases, more time is required to deplete the matrix and the pressure distribution becomes more gradual in the real time space. Fig.3.16 to Fig.3.18 show the domain pressure distribution for t =100 s, 300 s and 500 s when the matrix permeability is 0.01 md, comparing with the case when matrix permeability is 1 md (such as Fig.3.31 to Fig.3.33), the time for the depletion is much longer. The time step increment is 5 s in the simulation.

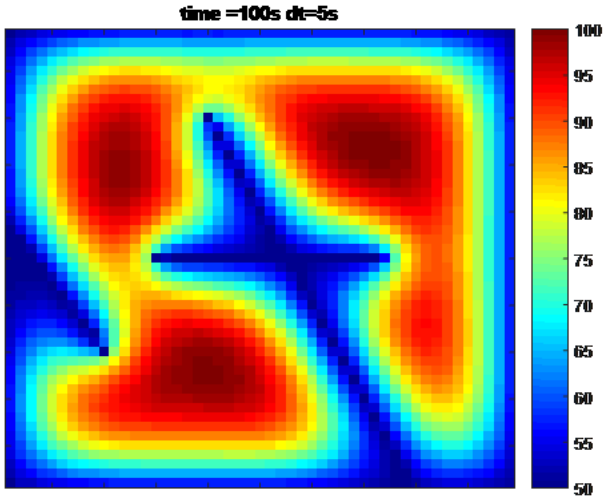

Figure 3.16: Pressure distribution at t = 100 s (k_m = 0.01 md, k_f = 2.11e5 md)

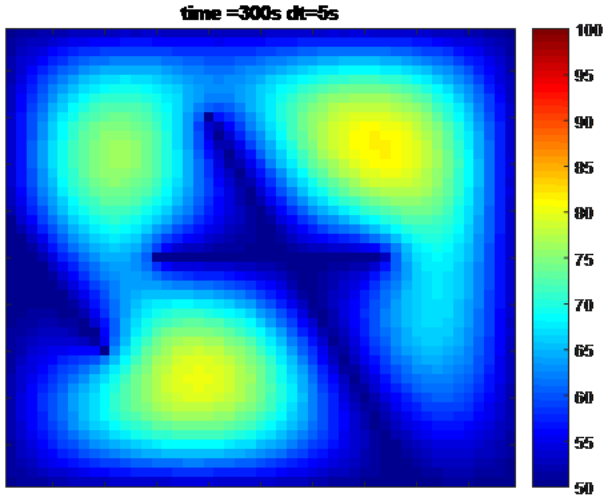

Figure 3.17: Pressure distribution at t = 300 s (k_m = 0.01 md, k_f = 2.11e5 md)

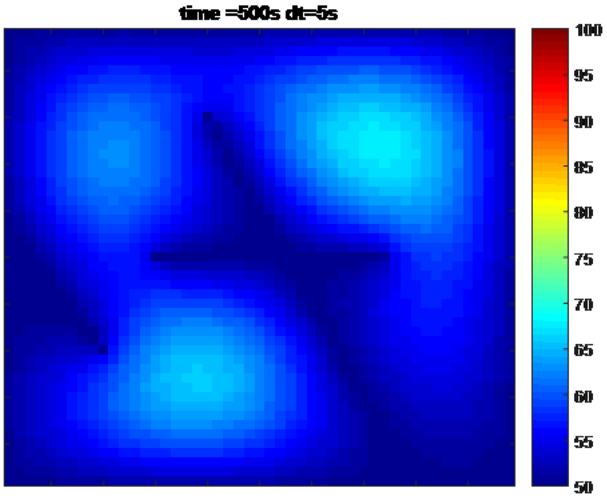

Figure 3.18: Pressure distribution at t = 500 s (k_m = 0.01 md, k_f =2.11e5 md)

Second, the influence of the fracture permeability is studied. Here the matrix permeability is set as 0.01 md, and the fracture permeability is varied. Fig.3.19 to Fig.3.21 show the pressure distributions for fracture permeability of 2.11e3 md. And Fig.3.22 to Fig.3.24 show those for the fracture permeability of 2.11e8 md.

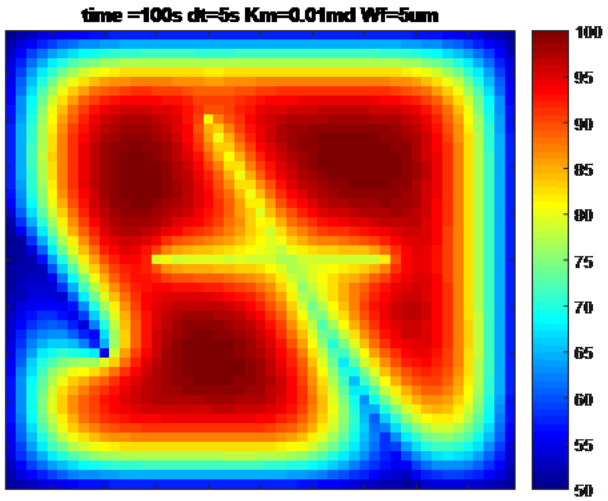

Figure 3.19: Pressure distribution at t = 100 s (k_m = 0.01 md, k_f = 2110 md)

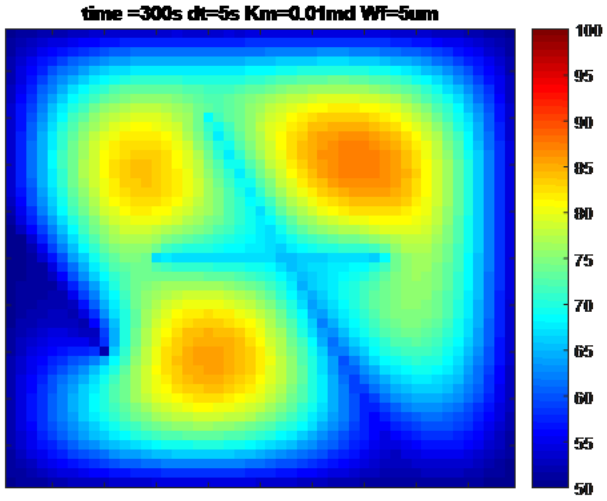

Figure 3.20: Pressure distribution at t = 300 s (k_m = 0.01 md, k_f = 2110 md)

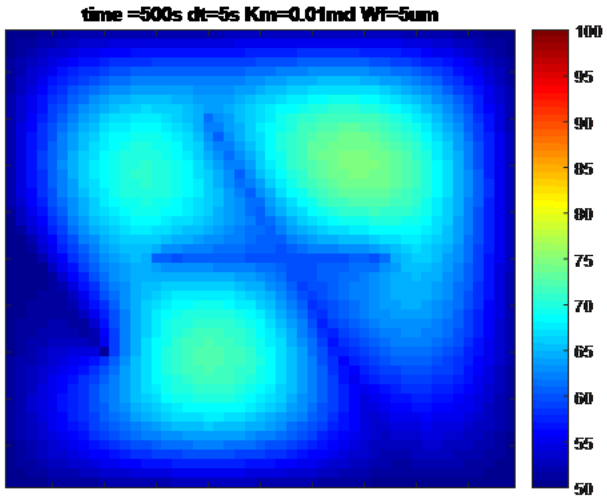

Figure 3.21: Pressure distribution at t = 500 s (k_m = 0.01 md, k_f = 2110 md)

Comparing with Fig.3.16 to Fig.3.18 (whose fracture permeability are 2.11e5 md), Fig.3.19 to Fig.3.21 have a little higher average pressure, which indicates that the pressure depletion is slowed due to lower fracture permeability. and the pressure depletion process for the case of Fig.3.22 to Fig.3.24 is almost identical as Fig.3.16 to Fig.3.18, which indicates although the fracture permeability increases one thousand times (from 2.11e5 md to 2.11e8 md), the pressure depletion process

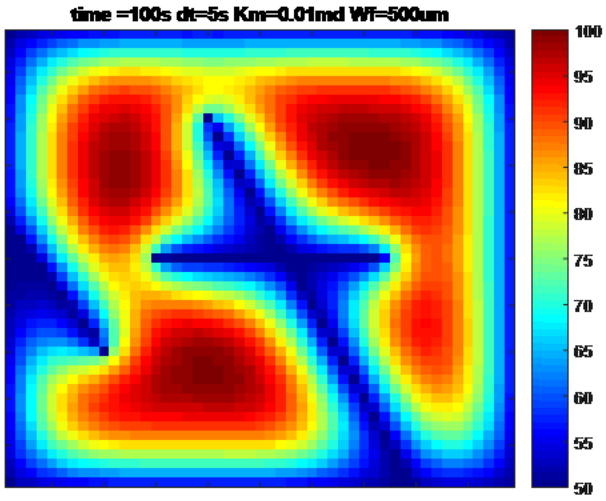

Figure 3.22: Pressure distribution at t = 100 s (k_m = 0.01 md,k_f = 2.11e8 md)

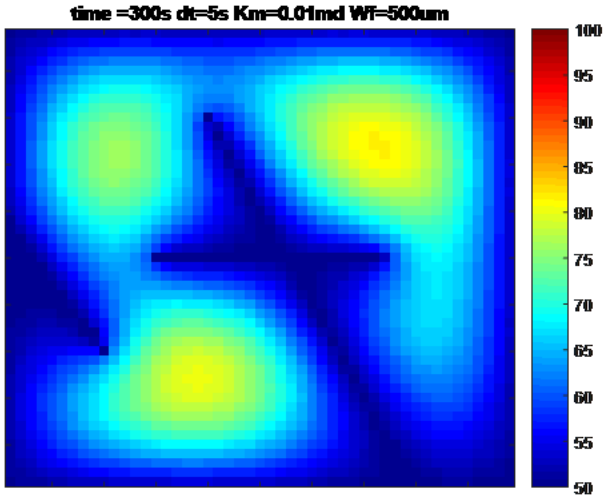

Figure 3.23: Pressure distribution at t = 300 s (k_m = 0.01 md,k_f = 2.11e8 md)

does not speed up significantly.

To quantify the influence of the fracture permeability, we calculate the relative difference comparing with the base case (whose fracture permeability is 2.11e5 md, such as Fig.3.16 to Fig.3.18), and the relative difference is defined as:

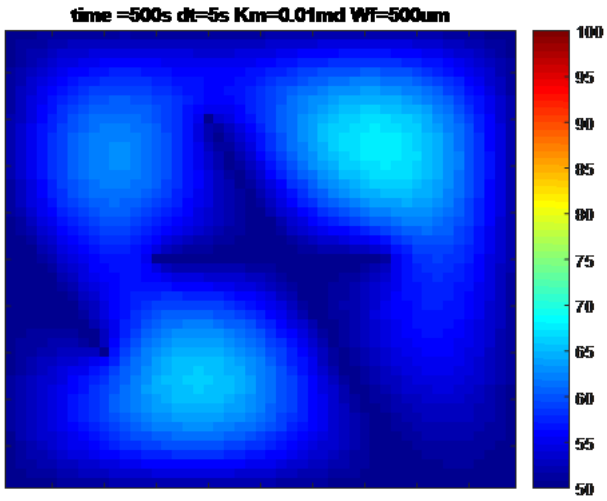

Figure 3.24: Pressure distribution at t = 500 s (k_m = 0.01 md,k_f = 2.11e8 md)

$$\epsilon = \frac{|p_b - p_c|}{p_b} \tag{3.13}$$

Where p_b means the pressure computed from the base case, and p_c means the pressure from other fracture permeability cases. The relative difference maps at t = 100 s for the two cases (whose fracture permeabilities are 2.110e3 md and 2.11e8 md, respectively) are shown in Fig.3.25 and Fig.3.26 respectively.

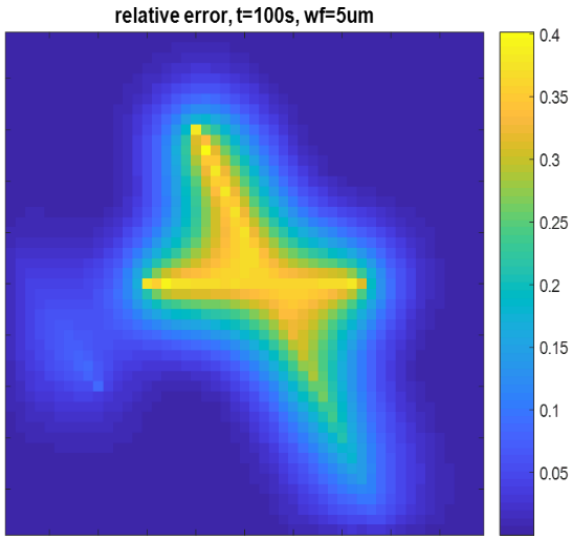

Figure 3.25: Relative error between Fig.3-16 and Fig.3-19

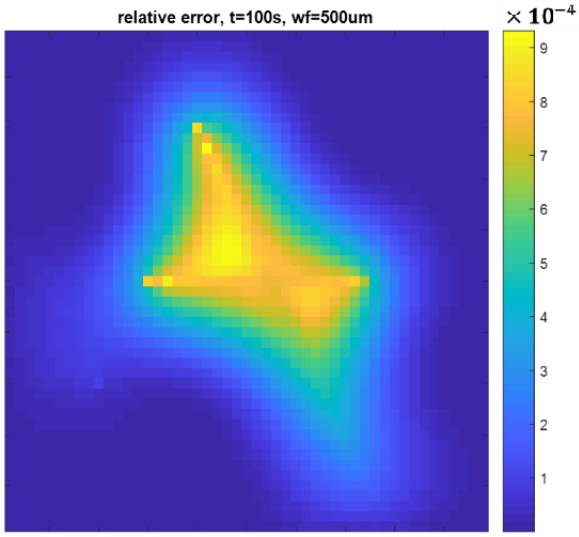

Figure 3.26: Relative error between Fig.3-16 and Fig.3-22

And we can see that the maximum relative errors are about 0.4 and 9.31e-4 respectively for Fig.3.25 and Fig.3.26. This proves our observation: keeping the other parameters constant, as the fracture permeability increases over a critical value, the pressure distribution generated will not

change significantly. Before reaching that critical value, the fracture permeability still plays an important role in influencing the flow dynamics and pressure distribution, as proved by Fig.3.25. After reaching the critical value, the flow will be mainly constrained by other parameters (instead of the fracture permeability), such as the matrix permeability, as indicated by Fig.3.26.

Third, the influence of the fluid viscosity is studied. In this part the fluid viscosity is set as constant 10 cp. And the pressure distributions for t = 100 s, 300 s, 500 s are presented in Fig.3.27 to Fig.3.29, respectively. Comparing the pressure distributions to those in Fig.3.11 to Fig.3.13 (whose k_m = 0.1 md, μ = 1 cp), we see as the fluid viscosity increases, the pressure perturbation slows down. Also, we notice that the pressure distributions for Fig.3.27 to Fig.3.29 (whose k_m = 0.01 md, μ = 10 cp), are very close to those of Fig.3.16 to Fig.3.18 (whose k_m = 0.01 md, μ = 1 cp). Indeed, the relative errors between the two cases after computation are found to be below a few percent.

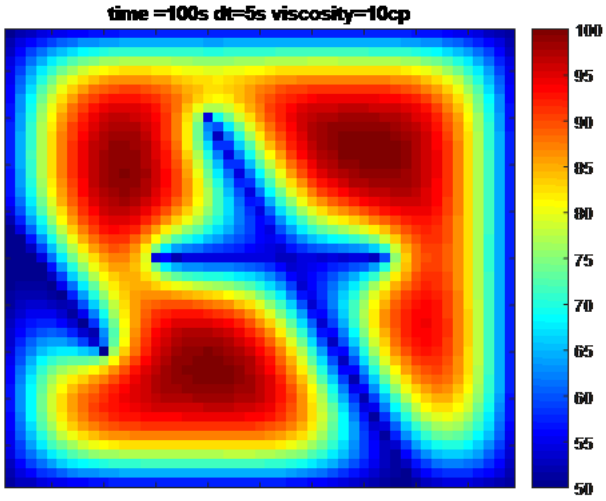

Figure 3.27: Pressure distribution at t = 100 s (k_m = 0.1 md, μ = 10 cp)

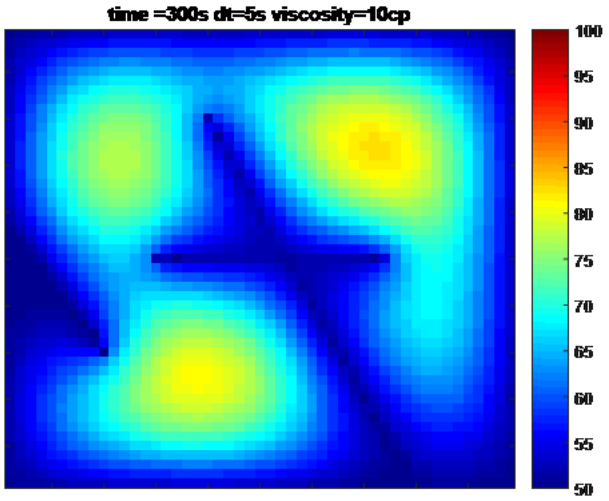

Figure 3.28: Pressure distribution at t = 300 s (k_m = 0.1 md, μ = 10 cp)

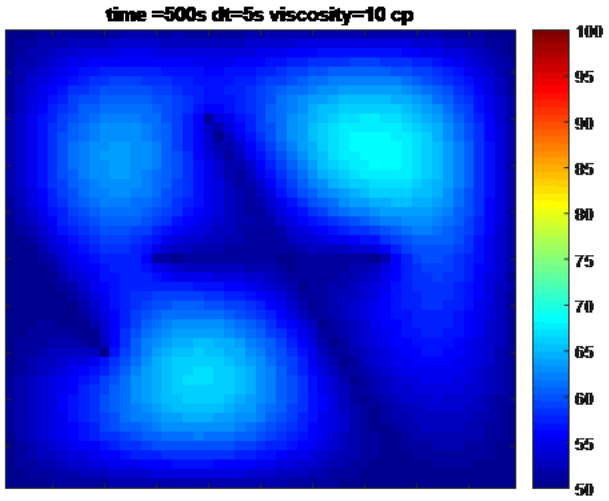

Figure 3.29: Pressure distribution at t = 500 s (k_m = 0.1 md, μ = 10 cp)

As in the single porosity homogeneous reservoir, the flow behavior is governed by the parameter ($\gamma = \dfrac{k}{\phi\mu c_t}$), any combination of the permeability k, porosity ϕ, viscosity μ and the total compressibility c_t resulting in the same value γ will have the same fluid flow behavior. In the fractured porous medium, a similar parameter of $\gamma_f = \dfrac{\alpha k_m}{(\phi_m c_m + \phi_f c_f)\mu}$ can be defined, where α is

the shape factor describing the flow interchange between the fractures and the matrix, and ϕ_m, c_m and ϕ_f, c_f indicate the corresponding compressibilities and porosities for the matrix and fractures, respectively. And the definition of parameter γ_f is inspired from Warren and Root (1963), by the multiplication of λ and τ, where λ and τ are two dimensionless parameters defined by Warren and Root. In our studies here, since the fracture network is fixed (then α is fixed), and the cases of Fig.3.27 to Fig.3.29 and those of Fig.3.16 to Fig.3.18 will generate the same value of γ_f, thus generate the similar pressure distributions.

3.4.4 Heterogeneous matrix porous medium without fractures

We have tested several cases to validate our model for handling matrix heterogeneity. These cases involve fluid flow in porous medium with and without fractures. For the cases where fractures are absent, the computed results are compared with the analytical solutions, and for the cases where fractures exist, the results are compared with the results from a commercial FEM simulator. We describe the cases where fractures are absent first.

A square porous medium with length of L is under consideration, such as Fig.3.2. The permeability of this porous medium is set in the form either as (1) quadratic variation $k = k_0(1+\beta y)^2$ or (2) exponential variation $k = k_0 e^{2\beta y}$, where k_0, β are constants, and y is the y coordinate. Notice the permeability changes only in the y direction. The boundary conditions applied are: no flow conditions for both the left and right boundaries, and the constant pressure conditions for the upper and lower boundaries. And the upper boundary has a higher pressure, while the lower boundary has a lower pressure, and the pressure difference applied is set as constant of $\bigtriangledown p$. The analytical solutions for these two permeability variations are respectively:

$$p(y) = \frac{y\sqrt{k_0}(1+\beta L) \bigtriangledown p}{\sqrt{k(y)}L} \tag{3.14a}$$

$$p(y) = \frac{\bigtriangledown p(1-e^{-2\beta y})}{1-e^{-2\beta L}} \tag{3.14b}$$

First, the case for the quadratic permeability variation is studied. The specific parameters

are: k_0 =5 md, $\beta = 0.05$, $\bigtriangledown p$ = 100 psi,and L = 100 ft. Fig.3.30 shows the permeability field for the porous medium, notice that along y direction the permeability increases. Fig.3.31 and Fig.3.32 show the pressure distributions computed from the analytical equation (Eq.(3.14a)) and our numerical simulator, respectively. In our simulation, the boundary elements and the internal points selected are 40 and 25, respectively. These two figures match very close, and Fig.3.33 represents the relative error map for 361 uniformly distributed internal points, which indicates the maximum relative error is below 0.03, which locates mainly at the lower corners and lower boundary of this porous medium.

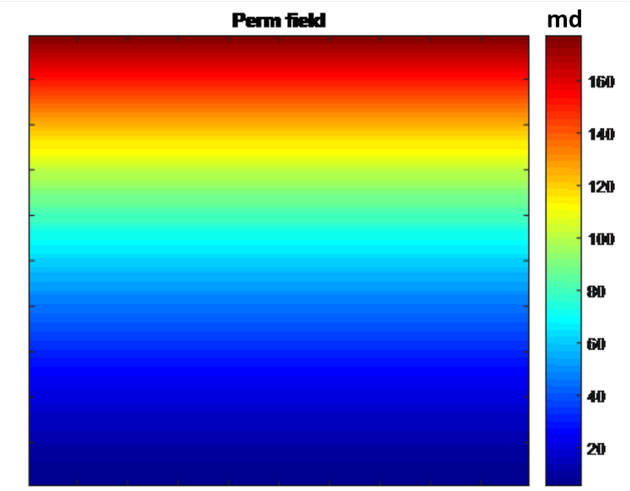

Figure 3.30: Schematic for quadratic permeability variation

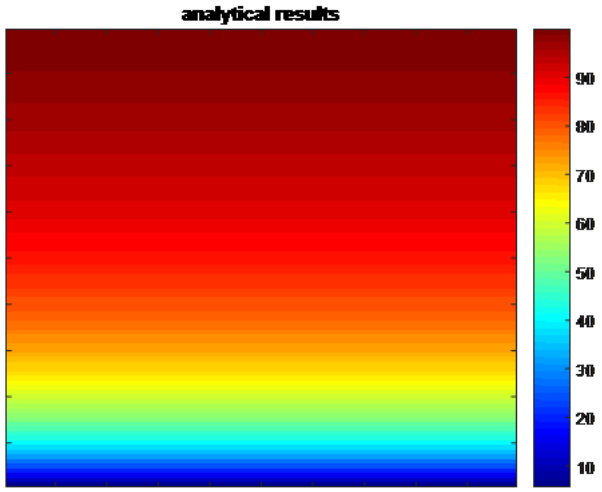

Figure 3.31: Pressure distribution from analytical solution for Case Fig.3.30

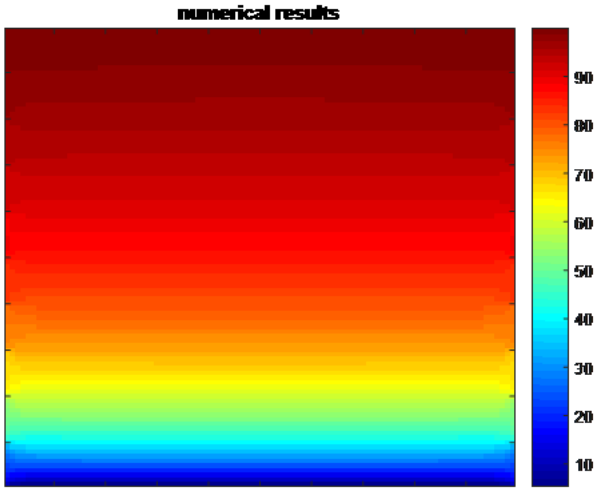

Figure 3.32: Pressure distribution from our solution for Case Fig.3.30

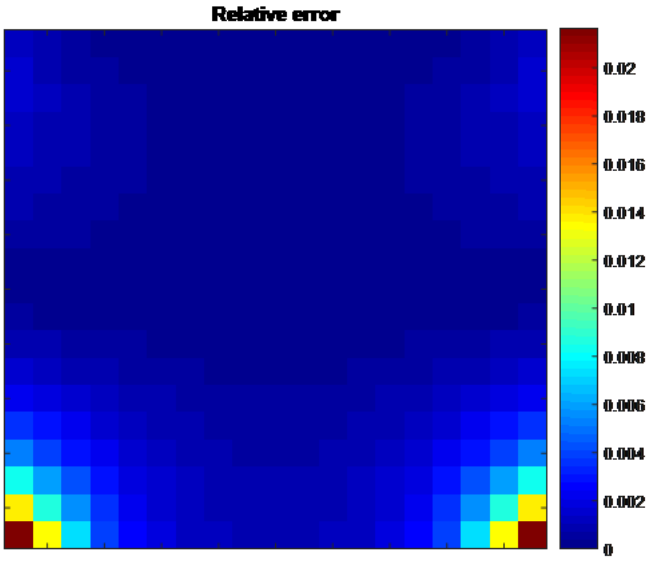

Figure 3.33: Relative errors between analytical and numerical solutions for Case Fig.3.30

Next, the case for the exponential permeability variation is studied. The specific parameters are: k_0 = 5 md, $\beta = 0.03$,$\bigtriangledown p$ = 100 psi,and L = 100 ft. Fig.3.34 shows the permeability field for this case. Fig.3.35 shows the pressure distribution computed analytically. Fig.3.36 shows the pressure distribution computed from our model with 120 boundary elements and 25 internal points. Again, the two figures match very well, with Fig.3.37 presents the relative error map for 361 uniformly distributed internal points, and the maximum relative error is below 0.037 with more than 90% of the relative errors are less than 0.02.

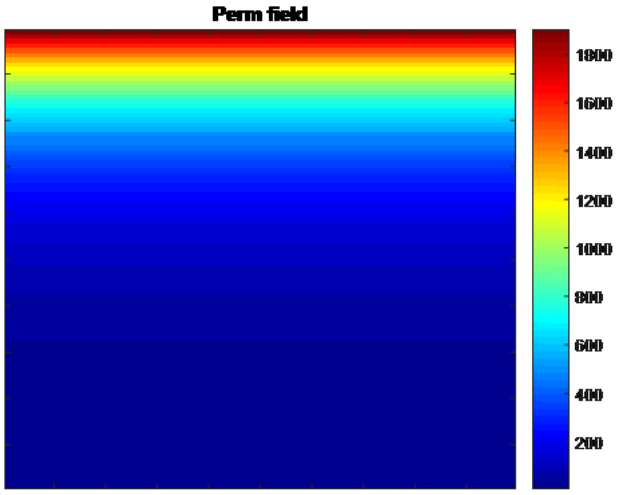

Figure 3.34: Schematic for exponential permeability variation

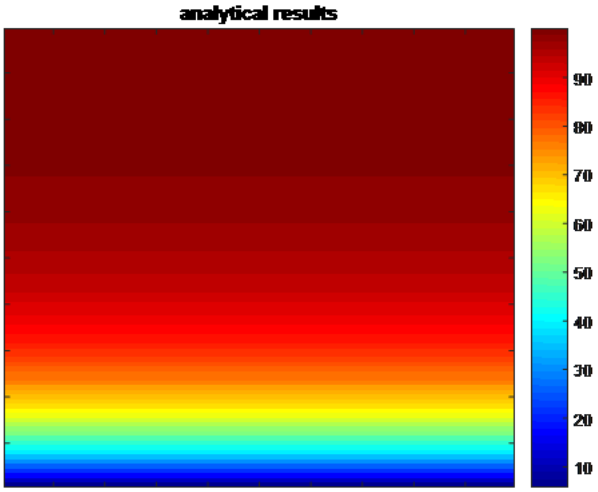

Figure 3.35: Pressure distribution from analytical solution for Case Fig.3.34

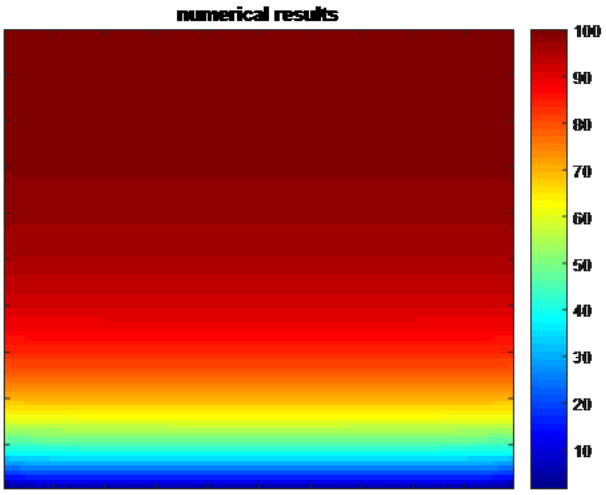

Figure 3.36: Pressure distribution from our solution for Case Fig.3.34

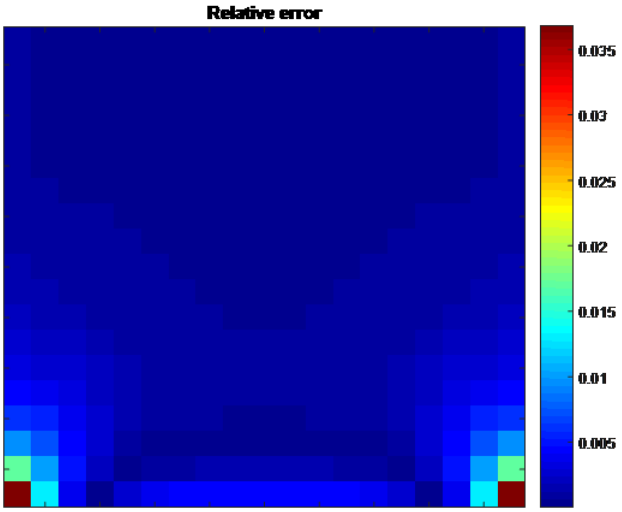

Figure 3.37: Relative errors between analytical and numerical solutions for Case Fig.3.34

3.4.5 Heterogeneous matrix porous medium with fractures

Next, we incorporate the influence of fractures in our simulation. A unit square porous medium embedded with five fractures is considered, see Fig.3.38. No flow boundary condition is applied to

the left and the right boundary. And the pressures at the upper boundary and the lower boundary are set as 100 psi and 50 psi, respectively. The fluid viscosity is set as 1 cp. The fracture aperture is 5 um and accordingly its permeability is 2110 md. The matrix permeability is set following the exponential variation $k = k_0 e^{2\beta y}$, where k_0 = 5e-4 md and β = 3.

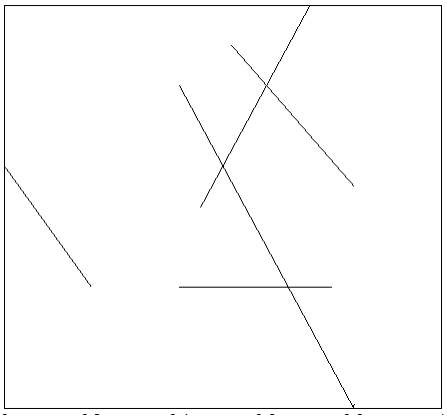

Figure 3.38: Fracture configurations in a block porous medium

Fig.3.39 and Fig.3.40 show the numerical solutions from a commercial FEM simulator and our BEM simulator, respectively. For the FEM simulation, there are 684 triangular elements discretized, see Fig.3.41. For our DRBEM simulation, the numbers of the boundary elements and the internal points are 40 and 25 respectively. And the number of the fracture elements is 73. The pressure distributions from these two methods are very close (as shown in Fig.3.39 and Fig.3.40). To quantify the difference, we computed the pressures at points $(\frac{i}{10}L, \frac{j}{10}L)$, where $i, j = 1, 2, \cdots, 9$, L is the square porous medium length, and the results are shown in Fig.3.42. The maximum relative error is 6.1%, with most of the relative error is below 2%. Also, the accuracy can be improved if more boundary elements or internal points are set.

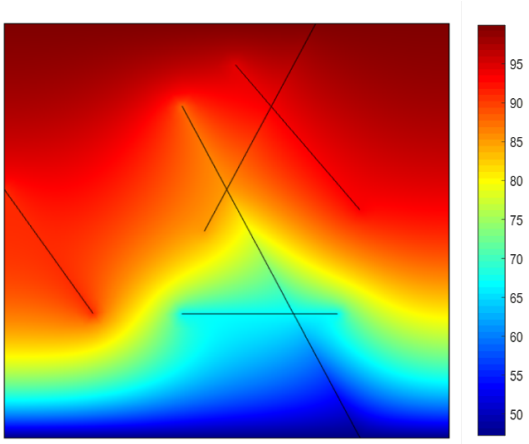

Figure 3.39: Pressure distribution from FEM simulator for Case Fig.3.38

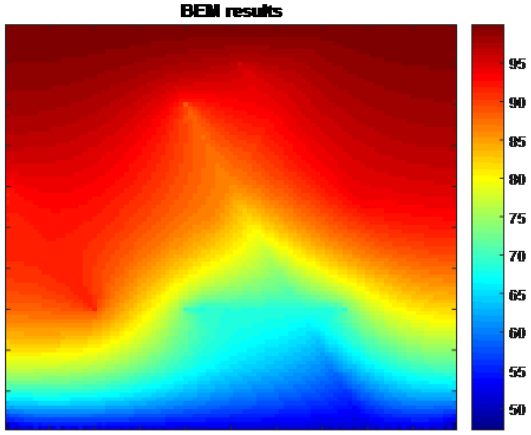

Figure 3.40: Pressure distribution from our simulator for Case Fig.3.38

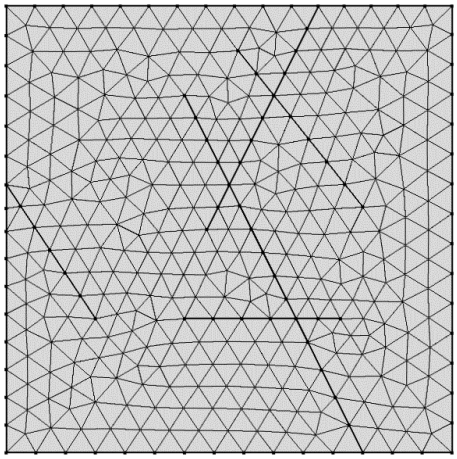

Figure 3.41: Domain discretization for Case Fig.3.38

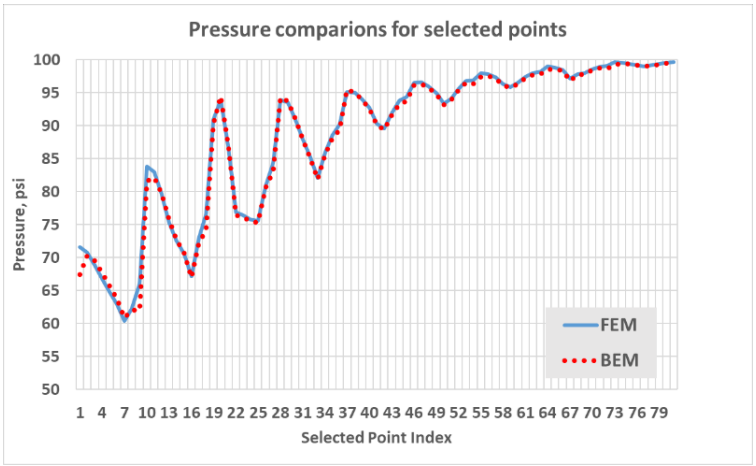

Figure 3.42: Pressure comparison for FEM solution and BEM solution

3.5 Conclusions

(1) Based on DRBEM, modules characterizing the transient flow dynamics and the matrix heterogeneity influence in fractured reservoirs have been developed;

(2) By comparing with analytical and/or numerical solutions, case studies validate the above modules;

(3) Sensitivity analysis indicates that: as the matrix permeability decreases or the viscosity increases, more time is required to deplete the porous medium;

(4) Keeping the other parameters constant, the depletion first speeds up as the fracture permeability increases, after the fracture permeability reaching over a certain value, the pressure distribution does not change significantly as the fracture permeability increases further;

4. FLOW SIMULATION FOR 3D FRACTURED RESERVOIR

We have extended our algorithm to simulate fluid flow in 3D fractured reservoirs. Not only regular fracture network, but also relatively complex fracture configurations can be incorporated. First, we will introduce the governing equations related to simulating flow in 3D fractured reservoirs; then the numerical implementation of the methodology is described, where the emphasis is put on the discretization algorithm and the assemblance of the matrix-vector system; finally, the results of the case study and conclusions are presented.

4.1 Governing equations

Eq.(4.1) and Eq.(4.2) are the governing equations are used to simulate flow in 3D fractured porous medium.

$$c(\xi)p(\xi) = \int_{\Gamma} G\frac{\partial p}{\partial n}d\Gamma - \int_{\Gamma} p\frac{\partial G}{\partial n}d\Gamma + \frac{\mu}{k_m}\sum_{i=1}^{n_f}\int_{\Gamma_{fi}} GQ(\vec{\xi})d\Gamma_{fi} \tag{4.1}$$

$$\bigtriangledown_f \cdot(\frac{k_f}{\mu} \bigtriangledown p) = \frac{Q}{w_f} \tag{4.2}$$

Where Γ and Γ_f are the boundary surfaces and the fracture surfaces. n_f is the number of the embedded fractures. Q is the source strength of the fracture plane to the matrix, and the last term of right hand side (R.H.S.) in Eq.(4.1) is the flow contribution from the fractures to the matrix. (See the introduction of Eq.(2.2) for the other nomenclatures.) Eq.(4.1) is the boundary integral equation which indicates how to compute the pressure at any point ξ using the variables on the boundary surfaces Γ and the fracture surfaces Γ_f. Eq.(4.2) is the differential equation which indicates the mass conservation in the fractures, where the mass at any point of the fractures conserves considering the flow terms and the fracture source term. In the derivation of Eq.(4.1) and Eq.(4.2), the gravity effects are ignored. And constant k_f, μ and w_f are assumed in the derivation.

Surface discretization is an important component in the whole workflow. The next part intro-

duces the algorithms developed to discretize the boundary surfaces and the fracture surfaces. The approaches computing the relevant parameters are also included.

4.2 Discretization scheme

The discretization is only done on the boundary surfaces and the fracture surfaces, and no domain discretization is needed. And the discretization on the boundary surfaces and the fracture surfaces are conducted separately. The discretization on the boundary surfaces is done using the conventional triangular discretization, while the discretization on the fracture surfaces is done through the perpendicular bisector (PEBI) method. The reason is that PEBI method can flexibly handle irregular fractures and complicated fracture intersections. We will take Fig.4.1 as an example to illustrate our algorithm, where two intersecting fractures are contained in a cubic porous medium, and the six boundary surfaces Γ and the two fracture surfaces Γ_f need be discretized.

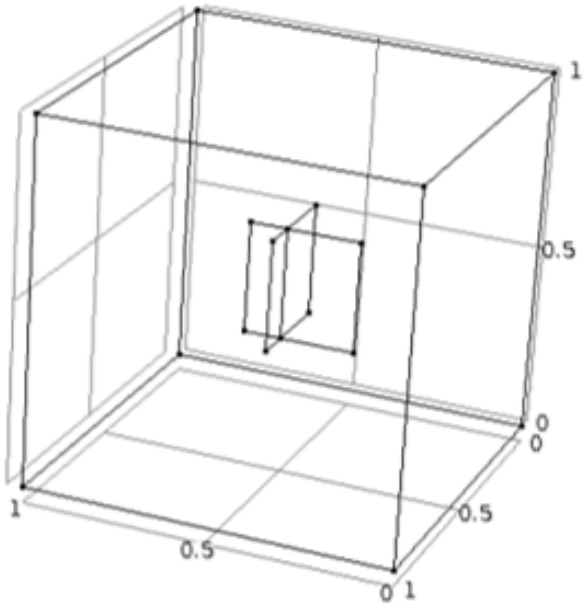

Figure 4.1: Fracture configurations in a cubic porous medium

4.2.1 Boundary surface discretization

Fig.4.2 shows one example for the discretization of the boundary surfaces. In this example, 14 triangles are generated in each boundary surfaces. Each boundary element is associated one unknown, which is either pressure or flow rate depending on the given boundary condition. A particular point inside each triangle (see description in Part 4.3) is selected as the allocation point and to represent the properties of that triangle.

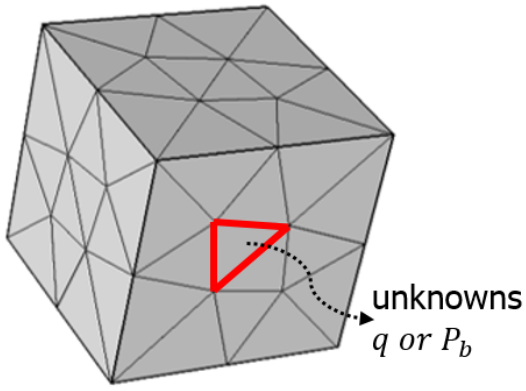

Figure 4.2: Boundary surface discretization example for Fig.4.1

4.2.2 Fracture surface discretization

The fracture surfaces are discretized into perpendicular bisector (PEBI) elements, such as Fig.4.3. The locally orthogonal unstructured grids can represent complex fracture network. Eq.(4.2) is applied to each PEBI element node. Two unknowns are associated with each PEBI element: the pressure p_f and the source strength Q.

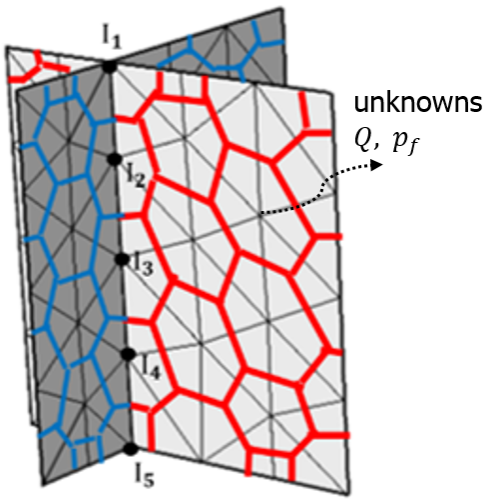

Figure 4.3: Fracture surface discretization for Fig.4.1

During the fracture surface discretization, some parameters need be computed and recorded. For each PEBI element, these parameters include: its neighboring element number and indexes, the connecting side lengths, the node distances, and the element area. For example, Fig.4.4 illustrates the fracture surface element i and its neighboring elements, there are 6 elements neighboring element i, whose nodes (also the equation allocation points) are represented by the green stars. O_i and O_j are the nodes of element i and element j. Then the lengths of O_iO_j and AB are the node distance $d_{j,i}$, the connecting side length $l_{j,i}$ for the connection of element i and element j, respectively.

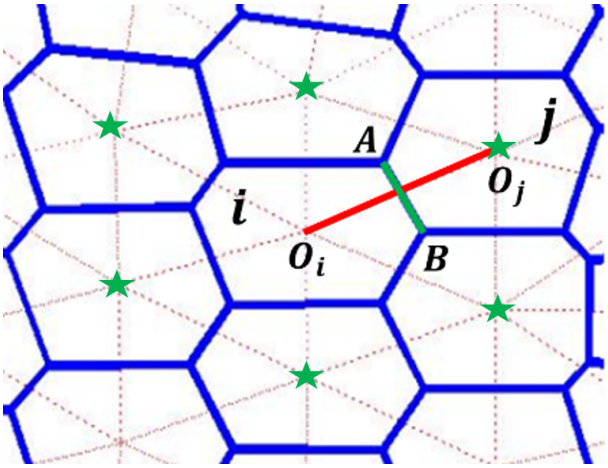

Figure 4.4: Schematic for PEBI element relevant parameters

The specific fracture discretization procedures are described in the following:

First, the fracture intersections are detected. Then the constrained Delaunay triangulation honoring these intersections are be conducted for each fracture surface. This triangulation step is tedious for complex fracture configurations. Some open source meshing programs and commercial softwares can be used, such as gmesh (Geuzaine and Remacle, 2009), Triangle (Shewchuk, 2002) and CMOSOL. Here we use the meshing feature in the commercial software CMOSOL, which takes the coordinates of the corner points (such as $A_1, B_1, \cdots, D_2$ in Fig.4.5) of all the fracture surfaces, and conducts the constrained Delaunay triangulation with specified element sizes for each fracture surface (as in Fig.4.5). The output of this step are the coordinates of all the triangle vertices and a triangulation connectivity list T, which is recorded as an m-by-3 matrix, where m is the number of triangles, and each row of T contains the vertex indexes that define that triangle. The output is then passed to our self-developed program.

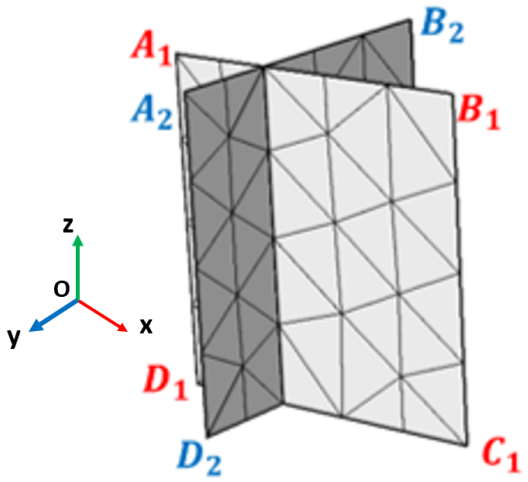

Figure 4.5: Delaunay triangulation on fracture surfaces

Second, generate the PEBI elements on the fracture surfaces using our self-developed Matlab code. The PEBI element generation is conducted on each fracture surface individually. The procedures include: (1) From the output of the last step, determine for each fracture surface: which triangles are included and their connectivity; (2) For each fracture surface, convert the coordinates for the triangles of 3D coordinate system $Oxyz$ to a 2D coordinate system $O'st$, Fig.4.6 shows one example of this conversion for fracture surface 1 (whose converted corner points are $A_1^{'}$,$B_1^{'}$,$C_1^{'}$, and $D_1^{'}$); (3) PEBI element generation is conducted on the converted 2D coordinate system $O'st$. The Voronoi diagram (PEBI elements) are dual to the Delaunay triangulation. Fig.4.7 shows the discretization result corresponding to Fig.4.6.

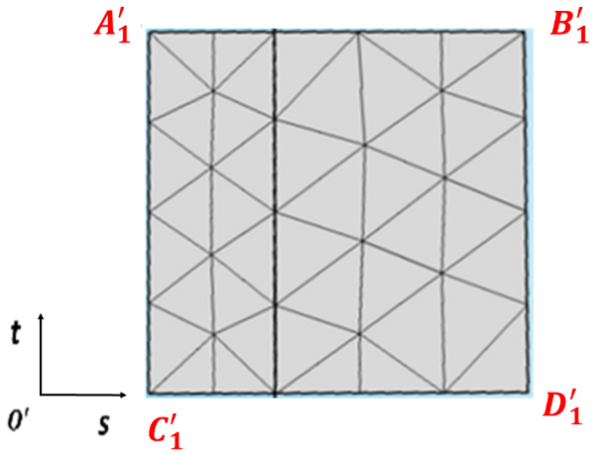

Figure 4.6: Coordinate conversion for fracture surface 1

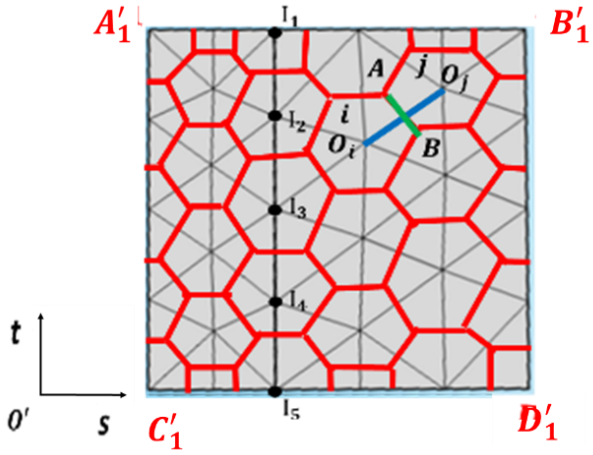

Figure 4.7: PEBI element generation for fracture surface 1 on the converted coordinate

The PEBI elements on all fracture surfaces are indexed together. And the relevant properties, such as the connectivities, the node distances, and the connecting side lengths, are computed for each PEBI element. In addition, the PEBI element indexes (such as $I_1, \cdots, I_5$ in Fig.4.7) corresponding to the fracture intersections, together with their belonged fracture surface indexes are

also recorded. The properties (such as pressure p_f, source strength Q) at the PEBI element nodes are taken to represent each element.

4.3 Numerical formulation

And suppose the boundary surfaces are discretized into N_b surface elements with symbols as Γ_b^i, where $i = 1, 2, \cdots, N_b$. The fracture surfaces are discretized into N_f elements with the symbols as Γ_f^i, where $i = 1, 2, \cdots, N_f$. Constant shape functions are used to approximate the unknowns on the (boundary and fracture) surface elements. The unknown on each boundary surface element Γ_b^i is u_i, which is either pressure or flow rate (depending on the given boundary conditions), and the unknowns on the fracture surface element Γ_f^j are pressure p_f^j and the source strength Q^j, where $i = 1, 2, \cdots, N_b$ and $j = 1, 2, \cdots, N_f$. In total we will have $N_b + 2N_f$ unknowns.

Eq.(4.1) can be transformed into the following discretized form, as

$$c(\xi)p(\xi) = \sum_{i=1}^{N_b} \int_{\Gamma_b^i} G \frac{\partial p}{\partial n} d\Gamma_b^i - \sum_{i=1}^{N_b} \int_{\Gamma_b^i} p \frac{\partial G}{\partial n} d\Gamma_b^i + \frac{\mu}{K} \sum_{i=1}^{N_f} \int_{\Gamma_f^i} GQ(\vec{\xi}) d\Gamma_f^i \tag{4.3}$$

In order to compute the integrals in Eq.(4.3), an interior point $(\bar{x}^i, \bar{y}^i, \bar{z}^i)$ is selected to represent each element Γ_b^i or Γ_f^i. For the boundary triangular element Γ_b^i, this point is determined using the approach introduced by Ang (2007). Ang (2007) parameterizes the points in each triangle using two variables a and b,

$$(x, y, z) = (X(a, b), Y(a, b), Z(a, b)) \quad \text{for} \quad 0 < a < 1 - b, \quad 0 < b < 1 \tag{4.4}$$

The point corresponding to $(X(\frac{1}{4}, \frac{1}{2}), Y(\frac{1}{4}, \frac{1}{2}), Z(\frac{1}{4}, \frac{1}{2}))$ is selected as the interior point for each boundary triangular element. Details on how to conduct this transformation of Eq.(4.4) are in Part 6.2.6 of Ang (2007). For the fracture surface element Γ_f^i, each PEBI element node is treated as the representative point.

Apply Eq.(4.3) to the selected internal points successively, $N_b + N_f$ equations can be generated:

$$p_j = \sum_{i=1}^{N_b} \int_{\Gamma_b^i} G \frac{\partial p}{\partial n} d\Gamma_b^i - \sum_{i=1}^{N_b} \int_{\Gamma_b^i} p \frac{\partial G}{\partial n} d\Gamma_b^i + \frac{\mu}{K} \sum_{i=1}^{N_f} \int_{\Gamma_f^i} GQ(\Gamma_f^i) d\Gamma_f^i \tag{4.5}$$

Where in the derivation, $c = 1$ are adopted since the elements under studied are all planar.

Eq.(4.2) is only applied on the fracture surface element Γ_f^i, whose discretized form is in the following:

$$\sum_{j=1}^{N_{eb}(i)} \frac{K_f A_{j,i}}{\mu d_{j,i}} (p_j - p_i) = Q_i S_i \quad i = 1, 2, \ldots, N_f \tag{4.6}$$

Where Q_i, and S_i are the planar source strength and the element area for the fracture element Γ_f^i, j is the index for its neighboring elements, and for each fracture element i, it has $N_{eb}(i)$ neighboring elements. (The exact values depend on the discretization scheme. For example, for finite difference method, N_{eb} is the same for all the non-boundary elements, which equals 4, and 8 for 2D and 3D problems, respectively. Here since we use finite volume method (FVM) to discretize the fracture surfaces, N_{eb} values may be different for different PEBI elements.) $A_{j,i}$ is the interface area between the fracture element i and its neighboring fracture element j, and $A_{j,i} = w_f l_{j,i}$, where w_f is the fracture aperture, and $l_{j,i}$ and $d_{j,i}$, as shown in Fig.4.4, are the connecting side length, the node distance between the element i and element j, respectively.

Eq.(4.5) and Eq.(4.6) form a set of $N_b + 2N_f$ equations , which correspond to the same number of unknowns. The equations are shown in block matrix form as Eq.(4.7):

$$\begin{bmatrix} \boldsymbol{A_1} & \boldsymbol{0_1} & \boldsymbol{C_1} \\ \boldsymbol{A_2} & \boldsymbol{B_2} & \boldsymbol{C_2} \\ \boldsymbol{0_2} & \boldsymbol{B_3} & \boldsymbol{C_3} \end{bmatrix} \begin{bmatrix} \boldsymbol{U} \\ \boldsymbol{P_f} \\ \boldsymbol{Q} \end{bmatrix} = \begin{bmatrix} \boldsymbol{R_1} \\ \boldsymbol{R_2} \\ \boldsymbol{0_3} \end{bmatrix} \tag{4.7}$$

Where $\boldsymbol{U}$ is a $N_b \times 1$ vector containing the boundary element unknowns u, and $\boldsymbol{P_f}$, $\boldsymbol{Q}$ are the unknown vectors containing the fracture element unknowns P_f and Q respectively. Both have the size of $N_f \times 1$. $\boldsymbol{A_1}, \boldsymbol{A_2}, \boldsymbol{B_2}, \boldsymbol{B_3}, \boldsymbol{C_1}, \boldsymbol{C_2}, \boldsymbol{C_3}$ are the coefficients matrixes for the respective unknowns derived from Eq.(4.5) and Eq.(4.6). $\boldsymbol{R_1}, \boldsymbol{R_2}$ are vectors generated from the known parts

of Eq.(4.5). $\mathbf{0_1}, \mathbf{0_2}$ and $\mathbf{0_3}$ are the zero matrixes, whose sizes are $N_b \times N_f$, $N_f \times N_b$ and $N_f \times 1$ respectively. $\boldsymbol{B_2}$ is the identity matrix with the size of $N_f \times N_f$. Eq.(4.7) are solved numerically using direct or iterative methods.

To be specific, two issues regarding to solving Eq.(4.7) are discussed: one is the surface integrals computation; the other is the fracture intersection treatment.

4.3.1 Surface integral computation

To solve Eq.(4.7), the integrals over the surface elements need be computed. For example, $\boldsymbol{A_1}$, $\boldsymbol{A_2}$ in Eq.(4.7) involve the integral computation over the boundary triangular elements. To be specific,

$$A_1(i,j) = \begin{cases} -\int_{\Gamma_b^j} G(\bar{x}^i, \bar{y}^i, \bar{z}^i; x, y, z) d\Gamma_b^j & \text{Pressure is given for } \Gamma_b^j \\ \int_{\Gamma_b^j} \dfrac{\partial G(\bar{x}^i, \bar{y}^i, \bar{z}^i; x, y, z)}{\partial n} d\Gamma_b^j - \dfrac{1}{2}\delta_{i,j} & \text{Flow rate is given for } \Gamma_b^j \end{cases} \tag{4.8}$$

Where G is the fundamental solution for the 3D Laplace operator, $(\bar{x}^i, \bar{y}^i, \bar{z}^i)$ are the coordinates of the representative point for element i, $i, j = 1, 2, \cdots, N_b$, and

$$A_2(i,j) = \begin{cases} -\int_{\Gamma_b^j} G(\bar{x}^i, \bar{y}^i, \bar{z}^i; x, y, z) d\Gamma_b^j & \text{Pressure is given for } \Gamma_b^j \\ \int_{\Gamma_b^j} \dfrac{\partial G(\bar{x}^i, \bar{y}^i, \bar{z}^i; x, y, z)}{\partial n} d\Gamma_b^j & \text{Flow rate is given for } \Gamma_b^j \end{cases} \tag{4.9}$$

Where $i = 1, 2, \cdots, N_f, j = 1, 2, \cdots, N_b$.

While $\boldsymbol{C_1}$, $\boldsymbol{C_2}$ involve $\int_{\Gamma_f^i} G(\bar{x}^i, \bar{y}^i, \bar{z}^i; x, y, z) d\Gamma_f^j$, which is the integral computation over the fracture PEBI elements Γ_f^j, where $j = 1, 2, \cdots, N_b$. To be specific, $\boldsymbol{C_1}$ computes the surface integrals for the representative points $(\bar{x}^i, \bar{y}^i, \bar{z}^i)$ on the boundary elements; while $\boldsymbol{C_2}$ computes the surface integrals for the representative points $(\bar{x}^i, \bar{y}^i, \bar{z}^i)$ on the fracture elements.

For the surface integral computation over boundary triangular elements: the approach outlined by Ang (2007) is adopted. The surface integrals over triangular elements are rewritten in terms of two new variables (t, v), as in Eq.(6.30) of Ang (2007). The Gaussian integration formula is

used to compute the transformed double integrals, as shown in Eq.(4.10), where F is some general function and f is its associated transformed function. The function values at 16 different points are summarized to give the value of the double integrals.

$$\int_{\Gamma_b^j} F(\bar{x}^i, \bar{y}^i, \bar{z}^i; x, y, z) d\Gamma_b^j \Rightarrow \int_0^1 \int_0^1 f(t, v) dt dv \approx \frac{1}{16} \sum_{i=1}^{16} f(t_i, v_i) \tag{4.10}$$

For the surface integral computation over the fracture PEBI elements: each PEBI element is essentially a polygon with a certain number of edges. And the edge number for different PEBI elements may be different. We developed a general and flexible numerical integration algorithm: (1) Any fracture PEBI element with m-sides is decomposed into either m triangles or $(m-1)$ triangles or $(m-2)$ triangles, see Fig.4.8. The triangles are generated by connecting the PEBI

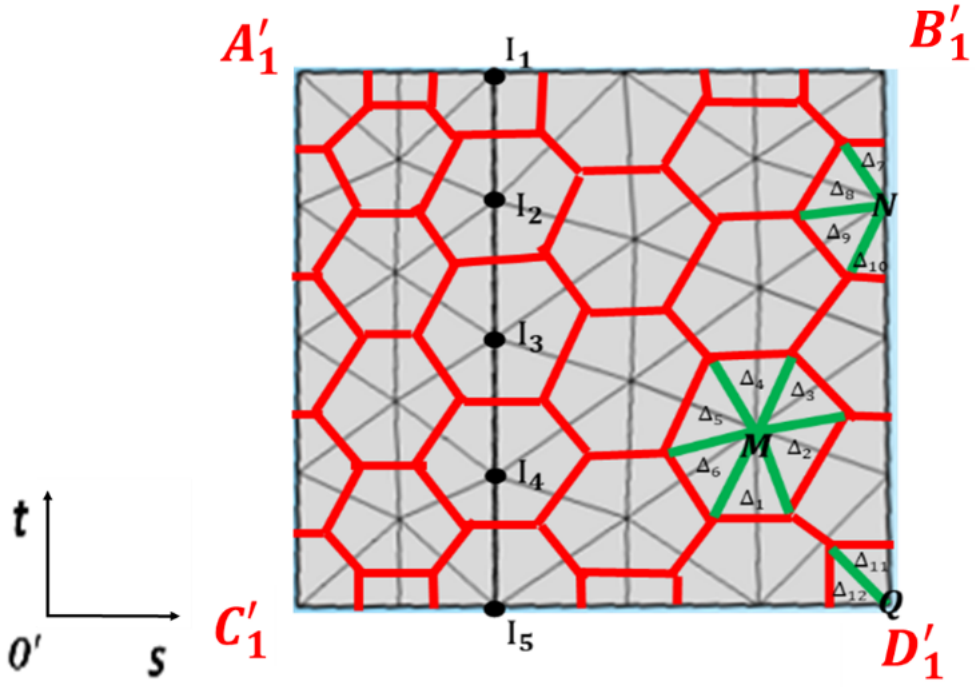

Figure 4.8: PEBI element triangular decomposition

element node with its vertices. And if the PBEI element lies inside the fracture surface plane (as

PEBI element M in Fig.4.8), then it will generate m triangles; when the PEBI element lies on the boundaries but not the corners (as PEBI element N in Fig.4.8), it will generate $(m-1)$ triangles; when it lies in the corner of the fracture plane (as PEBI element Q in Fig.4.8), it will generate $(m-2)$ triangles; (2) The surface integral over each decomposed triangle is computed through the approach described as in Eq.(4.10); (3) The surface integral over each PEBI element is acquired by summing up the surface integrals over its decomposed triangles. Eq.(4.11) lists the procedure we described for computing surface integrals over the fracture PEBI elements.

$$\begin{aligned}\int_{\Gamma_f^j} G(\bar{x}^i,\bar{y}^i,\bar{z}^i;x,y,z)d\Gamma_f^j = \sum_{S=1}^{N_\triangle(j)} \int_{\Gamma_{\triangle_S}^j} G(\bar{x}^i,\bar{y}^i,\bar{z}^i;x,y,z)d\Gamma_{\triangle_S}^j \Rightarrow \\ \sum_{S=1}^{N_\triangle(j)} \int_0^1 \int_0^1 f_S(t,v)dtdv \approx \sum_{S=1}^{N_\triangle(j)} \frac{1}{16} \sum_{i=1}^{16} f_S(t_i,v_i)\end{aligned} \tag{4.11}$$

Where $N_\triangle(j)$ is the number of the decomposed triangles for PEBI element Γ_f^j, $\Gamma_{\triangle_s}^j$ is the sth decomposed triangles, and $f_S(t,v)$ is the transformed two variable equation for computing surface integral over $\Gamma_{\triangle_s}^j$.

4.3.2 Fracture intersections

The fracture PEBI elements at the fracture intersections share the same element nodes. For example nodes $I_1,\cdots,I_5$ in Fig.4.3, each is shared by the two PEBI elements on the two corresponding fractures. Whenever intersections occur, the number of the pressure unknowns on the fracture surfaces reduces, since the PEBI elements shared with the same nodes have the same pressure.

Suppose there are N_I PEBI element nodes located at the fracture intersections, and each element node I_i ($i=1,2,\cdots,N_I$) is shared by N_{I_i} PEBI elements (that is N_{I_i} fractures intersecting at the node I_i, and $N_{I_i} \geq 2 \in \mathbb{N}$), then the number of pressure unknown reduction is $\sum_{i=1}^{N_I} N_{I_i} - N_I$. When applying Eq.(4.5) to some fracture PEBI element Γ_f^i, if an fracture PEBI element sharing the same node with Γ_f^i has already been allocated of Eq.(4.5), then this application of Eq.(4.5) is skipped. Correspondingly, the same number of equations are reduced in Eq.(4.5).

The application of Eq.(4.6) is also influenced by fracture intersections. First, for fracture PEBI elements sharing the same fracture intersections, Eq.(4.6) is applied for one (not all) of the PEBI elements. This results in the same number ($\sum_{i=1}^{N_I} N_{I_i} - N_I$) of equation reduction as that for Eq.(4.5). Second, the applications of Eq.(4.6) for nodes at fracture intersections will be different from those of non-intersections. Suppose one PEBI element node I_i is shared by N_{I_i} PEBI elements, and the indexes of these elements are $J_1, J_2, \cdots, J_{N_{I_i}}$, respectively. (The indexes are put in increase order and here we set $J_1 = I_i$). Each PEBI element J_i is contained in a sperate fracture surface with the number of its neighboring elements on that fracture as $N_c(J_i)$, and suppose the indexes of these neighboring elements are $T^1_{J_i}, T^2_{J_i}, \cdots, T^{N_c(J_i)}_{J_i}$. Then for element J_i, the net flow from its neighboring elements are $\sum_{k=1}^{N_c(J_i)} \dfrac{k_f A_{T^k_{J_i},J_i}}{\mu d_{T^k_{J_i},J_i}}(p_{T^k_{J_i}} - p_{J_i})$, since pressure at $J_1, J_2, \cdots, J_{N_{I_i}}$ are the same (as that of element I_i), so further this net flow can be written as $\sum_{k=1}^{N_c(J_i)} \dfrac{K_f A_{T^k_{J_i},J_i}}{\mu d_{T^k_{J_i},J_i}}(p_{T^k_{J_i}} - p_{I_i})$. Then Eq.(4.6) can be rewritten for element node I_i as:

$$\sum_{S=1}^{N_{I_i}} \sum_{k=1}^{N_c(J_s)} \frac{k_f A_{T^k_{J_s},J_s}}{\mu d_{T^k_{J_s},J_s}}(p_{T^k_{J_s}} - p_{I_i}) = \sum_{s=1}^{N_{I_i}} Q_s S_s \quad \text{for intersection element node } I_i \tag{4.12}$$

Where Q_s, S_s are the source strength and area for PEBI element s, the left-hand side and the right-hand side of Eq.(4.12) are the net inflow and the sum of the source strengths for intersection element node I_i. Eq.(4.12) represents the material conservation at the controlling volume of the shared node I_i.

There are in total $2 \times (\sum_{i=1}^{N_I} N_{I_i} - N_I)$ equation reductions for applying Eq.(4.5) and Eq.(4.6) when we have N_I intersection element nodes. The pressures of the PEBI elements sharing the same intersections are equal, this reduces the unknowns by a number of $\sum_{i=1}^{N_I} N_{I_i} - N_I$. We assume that the source strengths of the PEBI elements sharing the same intersections are equal, which reduces the number of the unknowns by another number of $\sum_{i=1}^{N_I} N_{I_i} - N_I$. Thus the equations are closed. Therefore, Eq.(4.10) can be derived as

$$\sum_{S=1}^{N_{I_i}} \sum_{k=1}^{N_c(J_s)} \frac{K_f A_{T^k_{J_s},J_s}}{\mu d_{T^k_{J_s},J_s}} (P_{T^k_{J_s}} - P_{I_i}) = Q_{I_i} \sum_{s=1}^{N_{I_i}} S_s \quad \text{for intersection element node } I_i \tag{4.13}$$

When fractures hit the boundaries, our algorithm is adjusted accordingly to honor the given boundary conditions.

4.4 3D case study

4.4.1 No fracture case

First, we would like to test our code applying for 3D problems without fractures. The result is compared with the analytical solution. The case is from an example in Partridge et al. (1992). The following equation is considered:

$$\frac{\partial^2 u}{\partial x^2} + \frac{\partial^2 u}{\partial y^2} + \frac{\partial^2 u}{\partial z^2} = -2 \tag{4.14}$$

Where u is the unknown variable. And since Eq.(4.14) is a non-homogeneous Laplace equation, the method of DRBEM is applied. Eq.(4.14) is solved for the geometry in Fig.4.9. The essential boundary condition as Eq.(4.15) is imposed on the cubic boundaries, which is also the analytical solution for this problem.

$$u = -\frac{1}{3}(x^2 + y^2 + z^2) \tag{4.15}$$

The cubic boundaries are discretized into triangular as shown in Fig.4.10. In total, there are 108 triangular elements on the boundaries, and one internal point in the cubic center is additionally taken for applying the DRBEM computation. We solved Eq.(4.14) following the approach outlined in the previous sections, and the results are compared with the analytical solution Eq.(4.15) for the 125 selected internal points, which uniformly distributed in the domain, with their x coordinates as $x = \frac{i}{6}L$, y coordinates as $y = \frac{j}{6}L$, z coordinates as $z = \frac{k}{6}L$, where L is the square side length, and $i, j, k = 1, 2, \cdots, 5$. The relative errors are shown in Fig.4.11. We can see the maximum

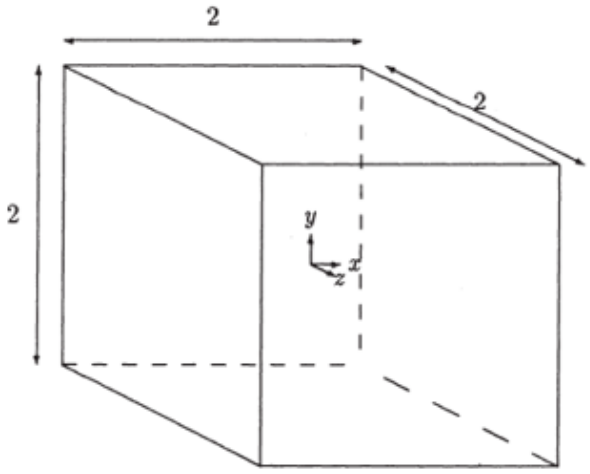

Figure 4.9: Geometry for 3D problem without fractures. Reprinted from Fig.4.15 in Partridge et al. (1992)

relative error is 6.48%, and most of the relative errors are less than 2%. This validates the capacity of our code in simulating 3D problems without fractures.

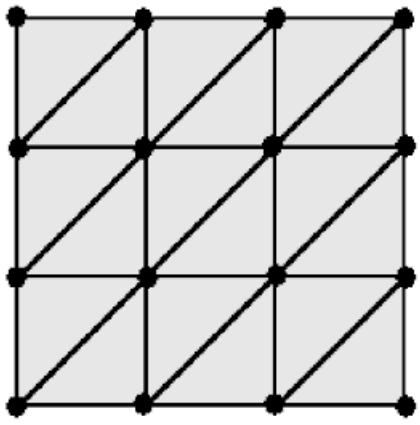

Figure 4.10: Discretized triangular on one boundary

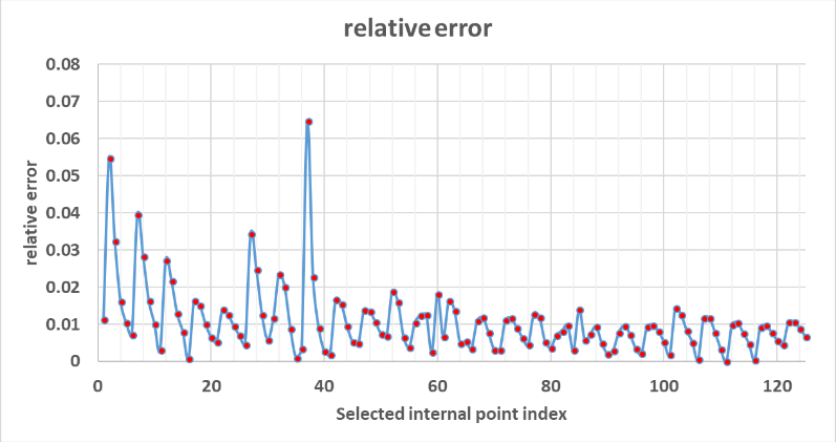

Figure 4.11: Relative errors at selected internal points

4.4.2 Multiple fracture case

Here we test a case with a cubic porous medium with 3 fractures, where two of them are intersecting with each other, Fig.4.12 shows the specific configurations. The fluid viscosity is set as 1 cp. The fracture aperture is 5 um and accordingly its permeability is 2110 md. The matrix permeability is set as 5e-4 md, the matrix porosity and fracture porosity are 0.05 and 1.0, respectively. And the pressures at boundary $y = 0$ and $x = 0$ are set as 100 psi and 50 psi, respectively. No flow condition is applied to the remaining boundaries.

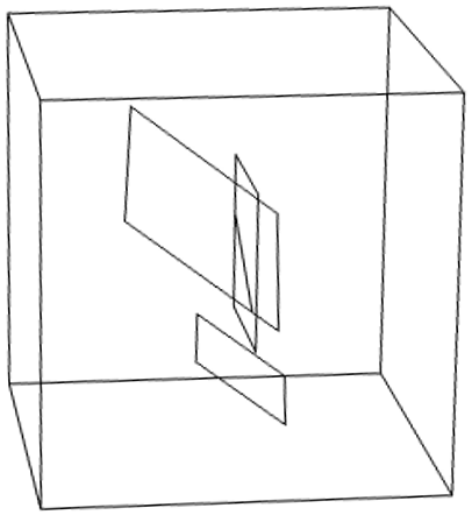

Figure 4.12: Fracture configurations for a cubic porous medium

If FEM method is used, the tetrahedral elements are generated. Fig.4.13 shows an example generated by a commercial simulator, and 806 tetrahedral elements are included. If the fracture

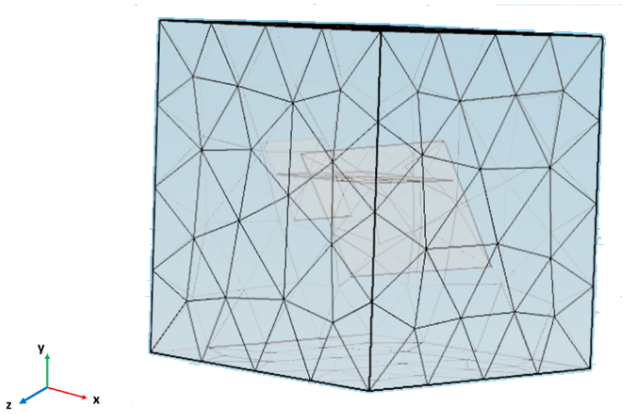

Figure 4.13: FEM Domain discretization of cubic porous medium

network is more complicated, the number of the tetrahedral elements will be increased largely. For our BEM simulator, only the cubic boundaries and the fracture surfaces are discretized, where the cubic boundaries are discretized as that in Fig.4.10, while the fracture surfaces are discretized

following the procedure we have outlined previously. Fig.4.14 and Fig.4.15 shows two different schemes of the fracture discretization, which have 82 triangular elements and 360 triangular elements, respectively. PEBI elements can be generated from these fracture surface triangles.

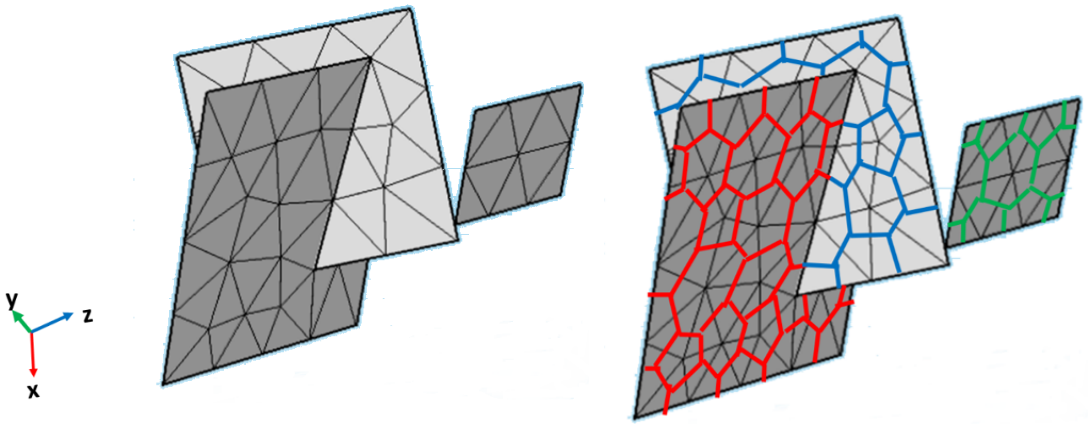

(a) Fracture triangulation (b) PEBI element generation

Figure 4.14: Fracture discretization for our simulator (82 triangles)

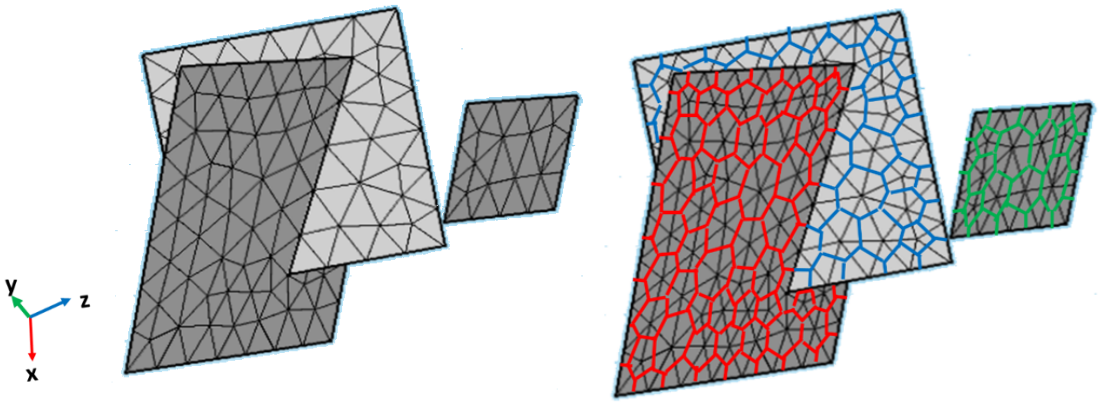

(a) Fracture triangulation (b) PEBI element generation

Figure 4.15: Fracture discretization for our simulator (360 triangles)

We have compared our results with those from a FEM simulator. Here the numbers of the PEBI

elements are 15, 13, and 16 on fracture 1, fracture 2, and fracture 3, respectively. And the number for the boundary triangular elements is 192. Fig.4.16 to Fig.4.18 show the pressure distribution computed for three cross sections $z = 0.2$, $z = 0.5$, and $z = 0.7$ respectively. The results are very close.

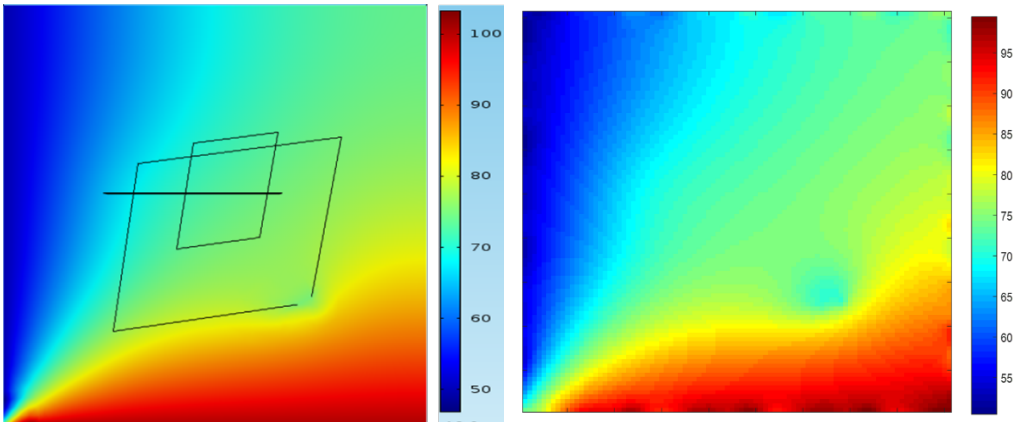

(a) FEM results (b) BEM results

Figure 4.16: Pressure distribution for $z = 0.2$ (left: FEM; right: BEM)

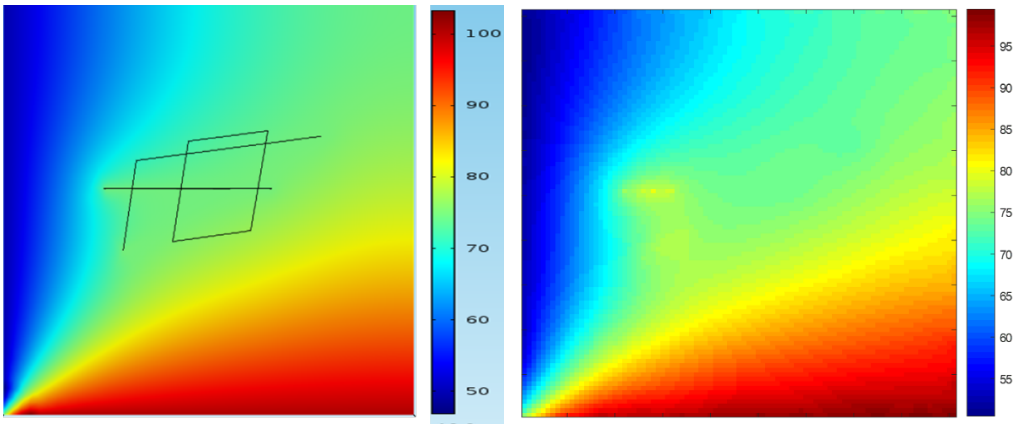

(a) FEM results (b) BEM results

Figure 4.17: Pressure distribution for $z = 0.5$ (left: FEM; right: BEM)

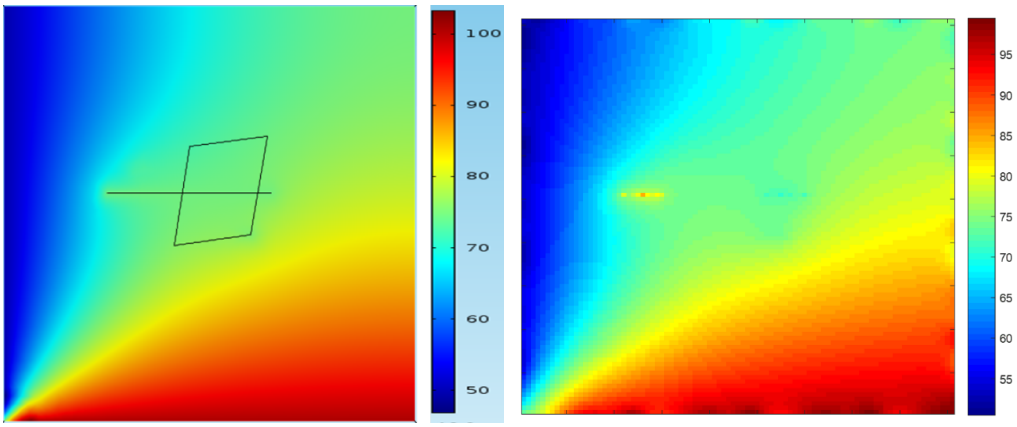

(a) FEM results (b) BEM results

Figure 4.18: Pressure distribution for $z = 0.7$ (left: FEM; right: BEM)

Fig.4.19 to Fig.4.21 show the pressure values computed from both FEM simulator and our BEM simulator for 81 points at the three cross sections. The coordinates for these selected points are $x = \frac{i}{10}L$, $y = \frac{j}{10}L$, z = 0.2, 0.5, and 0.7, where $i, j = 1, \cdots, 9$.

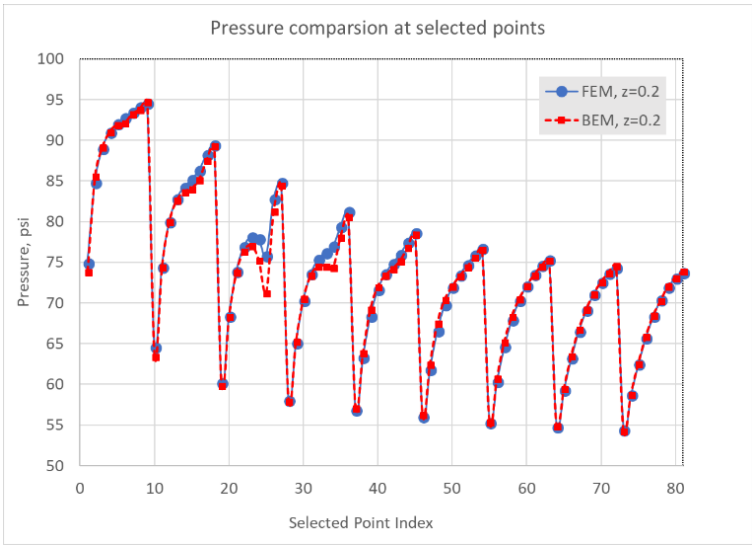

Figure 4.19: Pressure comparison at selected points for $z = 0.2$

We further compared the relative differences of the pressures in 729 internal points of the cubic

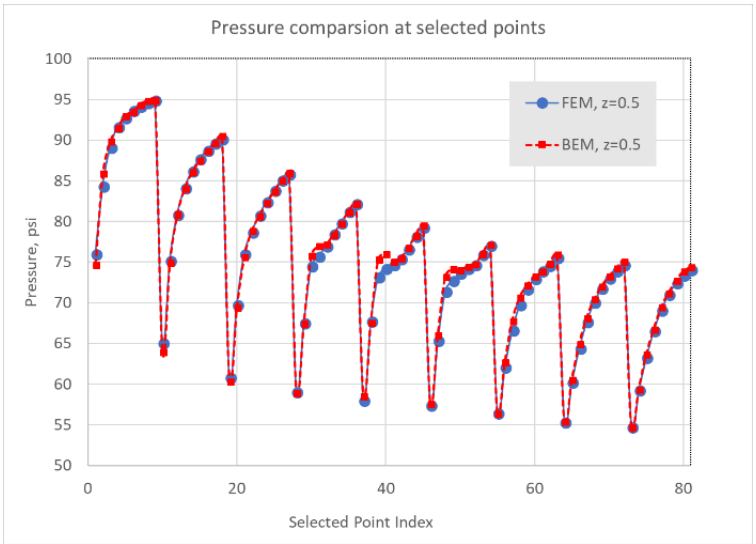

Figure 4.20: Pressure comparison at selected points for $z = 0.5$

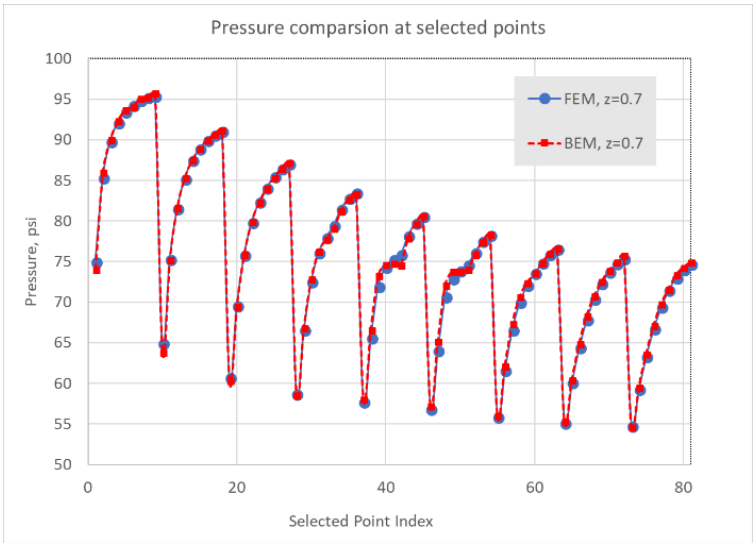

Figure 4.21: Pressure comparison at selected points for $z = 0.7$

domain, with their coordinates as $(\frac{i}{10}L, \frac{j}{10}L, \frac{k}{10}L)$, where $i, j, k = 1, \cdots, 9$. The maximum relative difference is 6.36%, and the average of the relative difference is 0.58%. This indicates the validity of our approach for modeling flow in 3D fractured porous medium.

4.5 Conclusions

(1) Novel formulations have been developed to characterize the fluid flow in 3D fractured porous medium. Fluid flow in the matrix is described using BEM/DRBEM approach, while the flow in the fracture are considered using FVM approach;

(2) A general workflow has been developed to discretize the fracture and boundary surfaces;

(3) The fracture surfaces are discretized into PEBI elements, which simplifies the modeling of complex fracture network comparing with domain discretization methods;

(4) General and flexible numerical integration algorithm is developed to compute the surface integral over the fracture PEBI elements;

(5) 3D Case studies have validated the feasibility of our simulator.

5. COMPOSITIONAL SIMULATOR DEVELOPMENT AND MULTI-COMPONENT DIFFUSION/ADSORPTION INFLUENCE IN SHALE RESERVOIRS*

The influence of multi-component diffusion/adsorption on fluid flow and hydrocarbon recovery are studied through our own developed compositional simulator. In the following section, the important aspects of the compositional simulator for modeling hydrocarbon recovery from shale reservoirs will be first described. The purpose is to show a general picture of the model's structure and methodology, and the methods/equations adopted in our study.

5.1 Governing equations

The component material balance equations serve as the governing equations, which have the following form:

$$\frac{\partial m_i}{\partial t} + \bigtriangledown \cdot \sum_{\alpha} (\rho_\alpha x_{i,\alpha} u_\alpha + J_{i,\alpha}) = Q_i - \frac{\partial Q_{ai}}{\partial t} \quad i = 1, \cdots, n_{hc}; \quad \alpha = o, g \tag{5.1}$$

$$\frac{\partial m_w}{\partial t} + \bigtriangledown \cdot (\rho_w u_w) = Q_w \tag{5.2}$$

Eq.(5.1) describes the material conservation of the non-aqueous components, where n_{hc} is the number of non-aqueous components, m_i is the molar mass for component i, ρ_α is the phase α (oil phase or gas phase) molar density, $x_{i,\alpha}$ is molar fraction of component i in phase α, u_α is the Darcy velocity for phase α, which is calculated using Darcy's Law, Q_i is the source/sink term for component i, and $J_{i,\alpha}$, Q_{ai} are the diffusion molar flux for component i in phase α, and the adsorption molar mass of component i, respectively, and more discussions on these two terms are in Part 5.2. Eq.(5.2) describes the material conservation for the water component (aqueous phase), where m_w is the molar mass for water component, ρ_w is the aqueous phase molar density, u_w is

*Part of this section is reprinted with permission from "A Novel Compositional Model of Simulating Fluid Flow in Shale Reservoirs - Some Preliminary Tests and Results" by Y. Cao, B. Yan, M. Alfi and J. E. Killough, 2015. SPE Proceedings, Copyright [2015] by Society of Petroleum Engineers.

the Darcy velocity for aqueous phase, Q_w is the source/sink term for aqueous phase.

$$u_\beta = \frac{kk_{r\beta}}{\mu_\beta} \bigtriangledown (p_\beta - \rho_\beta M_\beta g D) \quad \beta = o, g, w \tag{5.3}$$

Eq.(5.3) is Darcy's Law for calculating the phase velocity in Eq.(5.1) and Eq.(5.2), where k is the absolute permeability, $k_{r\beta}$ is the relative permeability of phase β ($\beta = o, g, w$), M_β is the molecular weight of phase β ($\beta = o, g, w$), D is vertical depth.

The diffusion and adsorption terms in the aqueous phase are ignored. Other formulation assumptions include instantaneous equilibrium between oil and gas phases in any grid block and mutual insolubility of water and hydrocarbon components. The Peng Robinson Equation of State is used for the gas and liquid thermodynamic property calculations (Peng et al. 1976). Finally, the finite difference method is used for discretization.

5.2 Diffusion/Adsorption terms

Besides the compressed oil and gas, a substantial fraction of the fluid stored in shale is adsorbed on the surface of the shale (Hill et al. 2000). The adsorbed hydrocarbon has critical influence on the assessment of shale-gas resources, and also has significant implications on the production profile. Ambrose et al. (2010) account for the pore space taken up by the sorbed phase, and proposes a new gas-in-place equation. Later a multi-component version of this equation was developed (Ambrose et al. 2011). Without properly accounting for the influence of the adsorbed phase, a 20% overestimation of the total gas storage capacity may occur (Ambrose et al. 2011). Haghshenas et al. (2014) studies the influence of heavy hydrocarbon fraction desorption on the production in liquid-rich shale gas reservoirs, and they observe that condensate production will largely increase as the heavy component fraction increases. Gas adsorption characteristics are influenced by the organic-matter type, thermal maturity and the content of moisture, but generally speaking, the higher the total carbon content (TOC), the greater the gas-sorption capacity (Zhang et al. 2012). We also try to investigate the influence of TOC on adsorption and the production profile in shale reservoirs; the corresponding algorithms incorporating TOC influence thus are developed.

Adsorption is usually described using an isotherm, which is defined as the amount of adsorbate on the adsorbent as a function of pressure at constant temperature. Various models have been proposed to describe the adsorption phenomenon and correlate pure- and mixed-gas adsorption isotherms, such as the Langmuir model, Extended Langmuir model, the ideal adsorbed solution (IAS) theory, real adsorbed solution (RAS) theory, two-dimensional equation of state (2D EOS) models, and pore-filling theory (Gasem et al. 2009). Among these the most popular remain the simple Langmuir model and its extensions to multi-components. This comes for good reasons: it is simple and easy to use, and also the performance of the Langmuir adsorption models is generally acceptable, probably due to the flexibility offered by the Langmuir parameters (Freeman et al. 2013) . Thus in our model we stick to the Langmuir model and Extended Langmuir model, whose forms are illustrated as follows:

$$Q_a = \rho_s \frac{pV_L}{p + P_L} \tag{5.4}$$

$$Q_{ai} = \rho_s \frac{V_{L,i} b_i p y_i}{1 + \sum_j b_j p y_j} \tag{5.5}$$

Eq.(5.4) is the Langmuir equation used for single component adsorption, and Eq.(5.5) is the Extended Langmuir equation for multi-component adsorption. Where Q_a is the adsorbed gas storage capacity, V_L is the Langmuir storage capacity, which equals the total storage at infinite pressure, P_L is the Langmuir pressure, which is the pressure with half of V_L stored, Q_{ai}, V_{Li} are the corresponding parameters for component i, b_i is the reciprocal of Langmuir pressure for component i, and y_i is gas molar fraction for component i, p is pressure, and ρ_s is the adsorbent density.

Three molecular diffusion models for single-phase multicomponent mixtures are commonly used: the classical Fick's first law, the Maxwell-Stefan (MS) model, and the generalized Fick's Law (Hoteit 2013). Most commercial and academic reservoir simulators apply the classical Fick's law, which assumes that each component diffuses as a result of only its own concentration gradient. The classical Fick's law is simple to compute and provides acceptable accuracy in most cases. But

Hoteit (2013) points out, it may fail to honor the total flux balance and in some cases the incorrect diffusion direction may be predicted. Thus besides the classical Fick's law, the generalized Fick's law is also incorporated into our simulator to account for the phase thermodynamic non-ideality and the component interactions. The two models adopted are expressed in Eq.(5.6) and Eq.(5.7) (Hoteit 2013).

$$J_i = -cD_i^{eff} \bigtriangledown x_i \quad i = 1, \cdots, n_c \tag{5.6}$$

$$J_i = -c \sum_{j=1}^{n_c-1} D_{ij} \bigtriangledown x_j \quad i = 1, \cdots, n_c - 1 \tag{5.7a}$$

$$J_{n_c} = -\sum_{j=1}^{n_c-1} J_j \tag{5.7b}$$

Where D_i^{eff} is the effective diffusion coefficient of component i, D_{ij} is the Fickian diffusion coefficient and characterizes the interaction of component j on the diffusion flux of component i, c is the overall molar density, x_i is the phase molar fraction of component i. Note that Eq.(5.7b) comes from the equi-molar constraint and guarantees that the total diffusion flux is zero (total flux balance). In our simulator, a variant form of the above equations is also used, which put the overall molar density into the operator $\bigtriangledown$, for example, therefore Eq.(5.6) evolves into

$$J_i = -D_i^{eff} \bigtriangledown (cx_i) = -D_i^{eff} \bigtriangledown (c_i) \quad i = 1, \cdots, n_c \tag{5.8}$$

Where c_i is the phase molar density of component i. In tight porous bodies, Knudsen diffusion may also be important.

Knudsen diffusion describes the gas molecules traveling through very small capillary pores, where the pore size is smaller than the mean free-path of the gas molecules and the molecules collide with the walls more often than between themselves. Many researchers have investigated the influence of Knudsen diffusion in shale reservoirs (Civan 2010; Alfi et al. 2014). Although the

classical and generalized Fick's law is initially developed for describing for molecular diffusion, an augmented effective diffusion coefficient can be adopted to incorporate the influence of Knudsen diffusion, such as (Sherwood et al. 1975)

$$D^{eff} = (\frac{1}{D_M^{eff}} + \frac{1}{D_K^{eff}})^{-1} \tag{5.9}$$

Where D^{eff}, D_M^{eff}, D_K^{eff} is the augmented effective diffusion coefficient, the effective molecular diffusion coefficient, and the effective Knudsen diffusion coefficient. In our model, a specialized and independent module is formulated to calculate or assign the diffusion coefficients. The diffusion coefficients can either be computed through some theoretical or empirical relations, such as Leahy-Dios and Firoozabadi's unified model (Leahy-Dios et al. 2007), or be assigned directly with experimental data, as did by Sun et al. (2014).

5.3 Numerical method

As concluded by Acs et al. (1985), for an isothermal system, the total number of fluid properties that uniquely determine all the others is n_c in the intensive case and $n_c + 1$ in the extensive case. In our model, we select the oil pressure p_o and the component molar masses m_i, $i = 1, \cdots, n_c$ as the $n_c + 1$ primary variables, and all the other properties can be uniquely determined thereafter. The corresponding $n_c + 1$ primary equations are the material mass balance equations described above, plus one additional equation $V_F = V_P$, which expresses that the volume of fluid, V_F, occupying in a block must be equal to the pore space available V_P in that block (Acs et al. 1985; Wong et al. 1987). The standard Newton-Raphson procedure, which involves the calculation of the partial derivatives of all the pertinent equations with respect to a set of selected primary variables in the Jacobian matrix, is used to compute the next time step's unknowns. At this stage, we use the IMPEM technique to solve our model, which treats the pressure implicitly and the component molar masses explicitly.

5.4 Simulation results and discussions

In this part, a few cases will be investigated. The validity of our compositional model, especially the capacity of the multi-component adsorption and diffusion feature, is tested. Some relevant parameters' influence on the shale fluid production is also presented. The parameters under investigation include the operating condition (bottom hole pressure), TOC, adsorption coefficients, fluid type, diffusivity, and wettability.

5.4.1 Adsorption feature case study

In this part, a 2D reservoir well model of a horizontal well with multi-stage hydraulic fractures as introduced in Chaudhary et al. is modeled (Chaudhary et al. 2011), as shown in Fig.5.1. The reservoir is 2000 ft long, 1000 ft wide and 200 ft thick. The well length consists of 10 transverse hydraulic fractures placed equally 200 ft apart, and the fracture half-length and height is 500 ft and 200 ft, respectively. Local grid refinement or adaptive mesh refinement (Luo et al 2008) can be used to capture the steep pressure and saturation changes near the hydraulic fractures. In our calculation, the logarithmically spaced grids are assigned along the fracture, and the "trick" proposed by Rubin (2010) is adopted, that is setting the simulation fracture cells as 2 ft wide and 41.65 md permeability instead of the physical fracture of 0.001 ft wide and 83300 md permeability. A quarter of a single fracture is selected as simulation unit, to get the entire well's production, the simulation results need be multiplied to 40. The specific reservoir and fracture properties set in our calculation are presented in Table 5.1.

The synthetic Eagle Ford gas-condensate with condensate gas ratio (CGR) of 30 stb/MMscf introduced by Orangi et al. (2011) is used as the reservoir fluid. The specific composition of the fluid (we name it as Fluid Type 1) is shown in Table 5.2. And the EOS parameters are also taken from Orangi et al. (2011).

The Langmuir coefficients used are from Ambrose et al. (2011), with the specific values shown in Table 5.3. We have taken the liberty to assign the C4+ data to the components from IC4 to C20+ since there are no other available adsorption data for them. Zero adsorption is assumed for N2.

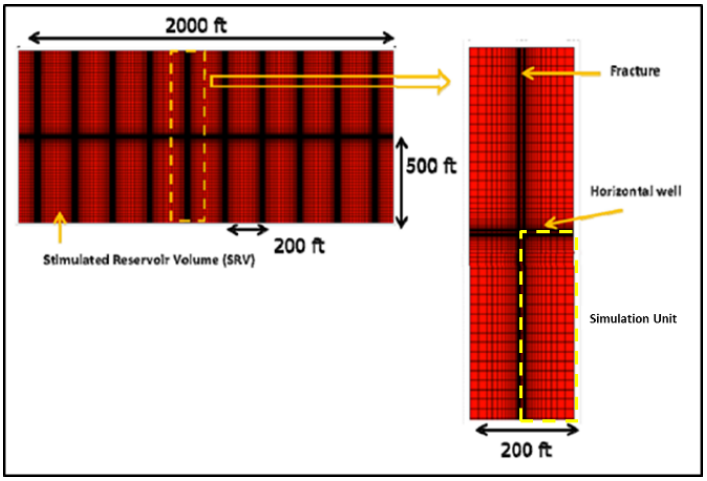

Figure 5.1: Simulated reservoir well model. Modified from Chaudhary et al. (2011)

Initial Water Saturation	0.05
Porosity in Shale	0.1
Compressibility of Shale	3e-6 psi^{-1}
Permeability of Shale	0.0001 md
Reservoir Thickness	200 ft
Fracture Spacing	200 ft
Fracture Half Length	500 ft
Fracture Width	0.001 ft
Fracture Perm	83300 md
Fracture Conductivity	83.3 md-ft
Fracture Cell Width	2 ft
Fracture Cell Permeability	41.65 md
Grid Size	$50 \times 25 \times 1$
Initial Reservoir Pressure	6000 psi
Initial Reservoir Temperature	$210\,^{\circ}F$

Table 5.1: Reservoir and fracture properties specification

The corresponding adsorption isotherms are shown in Fig.5.2.

Component	Mole Frac
C1	0.743
N2	0.002
C2	0.094
C3	0.052
CO2	0.031
ICH4	0.011
NCH4	0.02
IC5	0.008
NC5	0.007
NC6	0.002
C7+	0.0167
C11+	0.008
C15+	0.001
X20+	0.001

Table 5.2: Reservoir fluid composition Fluid Type 1. Reprinted from Orangi et al. (2011)

	C1	C2	C3	C4+	CO2
V_L (scf/ton)	56	91	179	232	145
P_L (psia)	1562	811	844	355	836

Table 5.3: Adsorption isotherm parameters. Reprinted from Ambrose et al. (2011)

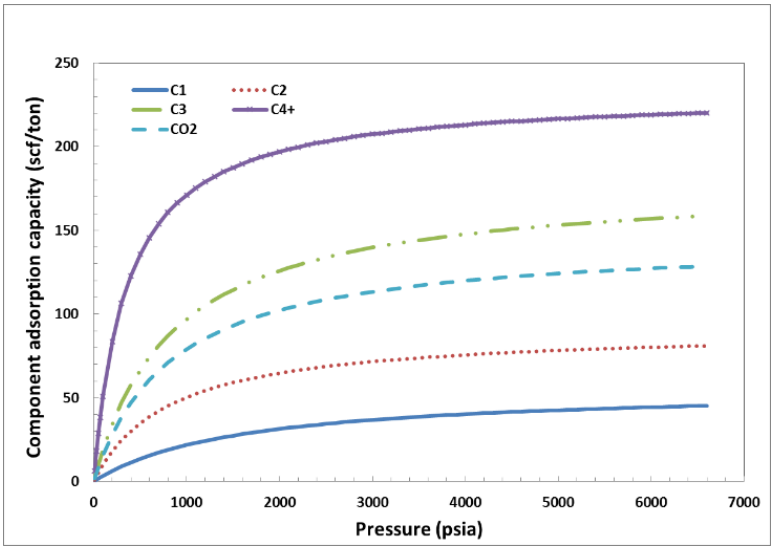

Figure 5.2: Adsorption isotherms for different components

The influence of the multi-component adsorption on shale fluid production are investigated, and the sensitivity analysis of the two relevant parameters, bottom hole pressure and TOC, are conducted, results are presented in the subsequent sections.

(A) Bottom hole pressure influence:

Three different constant production bottom hole pressures are investigated, 3000 psi, 4000 psi, and 5000 psi. We name them as Case 1, Case 2 and Case 3. Note for the fluid system (Fluid Type 1) we simulated, the dew point pressure is approximately 3500 psi (Haghshenas et al. 2014), thus, reservoir condensate dropout only occurs for Case 1. The cumulative gas and condensate production for the three cases with and without considering multi-component adsorption is shown in Fig.5.3 and Fig.5.4. We observe that the cases considering adsorption will unanimously yield more production (either for oil or gas) than their corresponding cases without adsorption consideration. The reason is that adsorption adds the gas in place significantly and as depletion continues, the released adsorbed hydrocarbon will offset the produced fluid and mitigate the decrease of the reservoir pressure. These results fit our expectations, and they reflect the significance of multi-component adsorption in shale reservoir development, similar results have also been reported by Haghshenas et al. (2014). Another observation is that for the three cases, the lower the production pressure, the more gas will be produced for the case with adsorption compared with the case without adsorption. It is hard to make this a general conclusion that the lower the production pressure, the more hydrocarbon we can recover for cases with the adsorbed hydrocarbon. As the low pressure also facilitates condensate dropout around the wellbore and may serve to increase the condensate blockage. This aspect should also be accounted for.

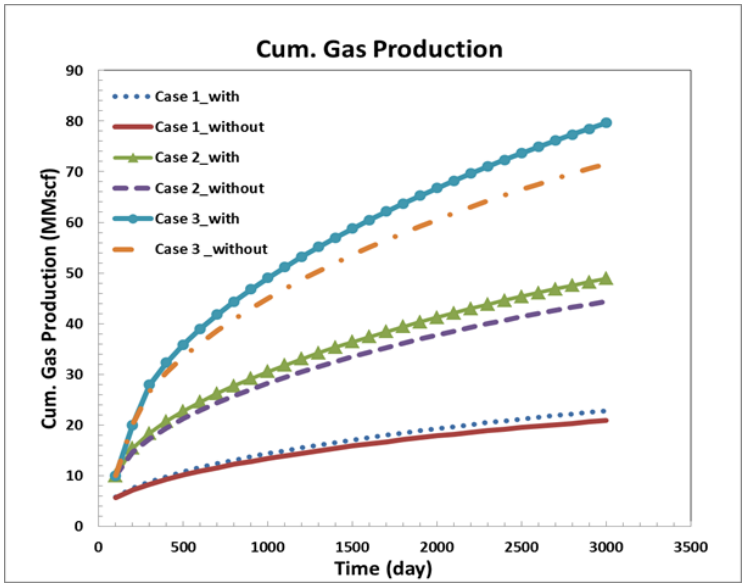

Figure 5.3: Cumulative gas production comparison for Case 1, Case 2 and Case 3

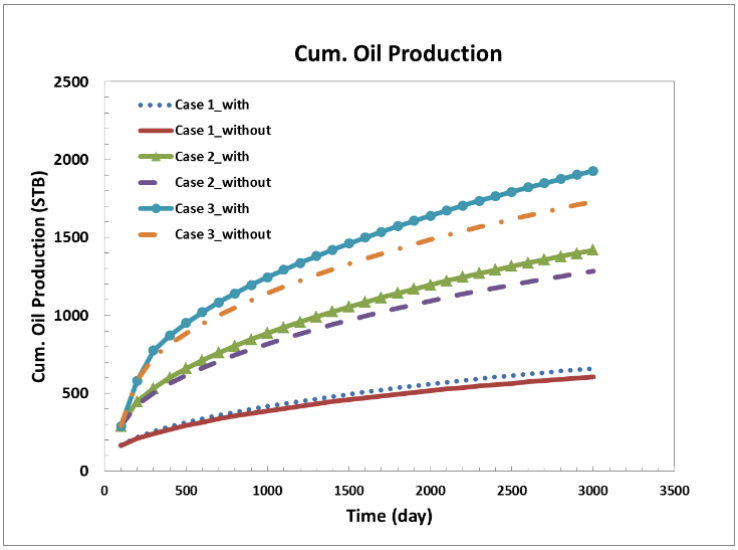

Figure 5.4: Cumulative condensate production comparison for Case 1, Case 2 and Case 3

(B) TOC influence:

Generally speaking, the higher the TOC content, the greater the gas-sorption capacity. Zhang et al. (2012) observes a linear relationship between methane Langmuir maximum capacity and TOC

in shale, shown in Fig.5.5. And a regression equation is given to relate TOC with the maximum capacity, shown in Eq.(5.10).

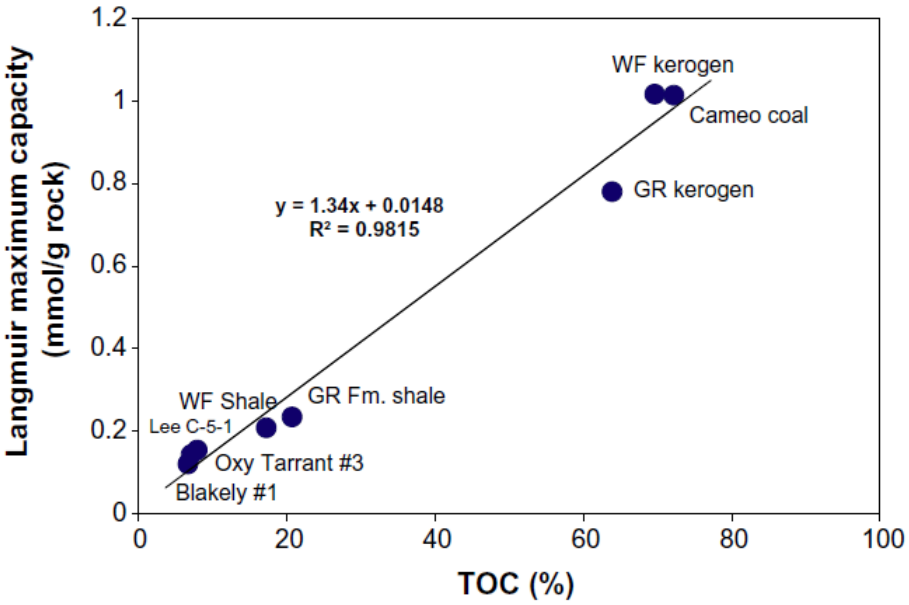

Figure 5.5: Linear relation between Langmuir maximum capacity and TOC. Reprinted from Fig.8 in Zhang et al. (2012)

$$V_L = 1.34 \times TOC + 0.0148 \tag{5.10}$$

Assume the methane adsorption data given in Table 5.3 fits this relation. This is a very tenable assumption, as mentioned in Ambrose et al. (2011), the TOC used to generate their data is 4%, when we substitute this value into Eq.(5.10), the Langmuir capacity will be 57.9 scf/ton and very close to the value of 56 scf/ton in Table 5.3. By analogy, other components in Table 5.3 follow the similar trend as in Eq.(5.10), which can be expressed as a general equation as in Eq.(5.11).

$$V_L = A_i \times TOC + B_i \tag{5.11}$$

Where V_{Li} is the Langmuir maximum capacity for component i, and A_i, B_i are the constants for linear relations between Langmuir maximum capacity and TOC of component i. For methane, the constant values are already known as 1.34 and 0.0148, respectively. For the other components, we only know that when we substitute TOC as 4% into Eq.(5.11), the value should equal to its corresponding value in Table 5.3. Since no experimental data is available, a further assumption that B_i of all the components equals to 0.0148 is made, after that A_i of the other components can be calculated and the results are shown in Table 5.4.

	C1	C2	C3	C4+	CO2
$\boldsymbol{A_i}$	1.34	2.51	5.29	6.96	4.21

Table 5.4: A_i value for different components

Thus the Langmuir maximum capacity for all the components can be calculated through Eq.(5.11) together with Table 5.4. In this paper, three cases with different TOC are considered, 2%, 4% and 6%. The maximum adsorption capacity V_L for the three cases are calculated and listed in Table 5.5.

TOC	C1	C2	C3	C4+	CO2
2%	34	51	95	121	78
4%	56	91	179	232	145
6%	78	131	263	342	212

Table 5.5: Maximum adsorption capacity V_L (scf/ton) for different TOC

The Langmuir pressure P_L is constant at a given temperature (Halliburton 2008), the values will be kept the same as those in Table 5-3. First we examine the Fluid Type 1, and the bottom hole pressure will be set as 4000 psi. The cumulative gas productions for the three TOC values are compared in Fig.5.6. Only slightly increase appears for the cumulative gas production as the

TOC increases, and in Fig.5.6 the three curves for different TOC can hardly be distinguished. The similar behavior is also observed for the cumulative oil production of this fluid system. The reason is that during the pressure range (from the initial reservoir pressure 6000 psi to bottom hole pressure 4000 psi), for this fluid system Fluid Type 1 the amounts of the desorbed hydrocarbon are comparably insignificant for the recovery of the three TOC cases. To confirm this, the mixture Langmuir curves of the three TOC cases are calculated and shown in Fig.5.7. Apparently, in the pressure range we investigated, gas desorption is very limited for all three TOC values.

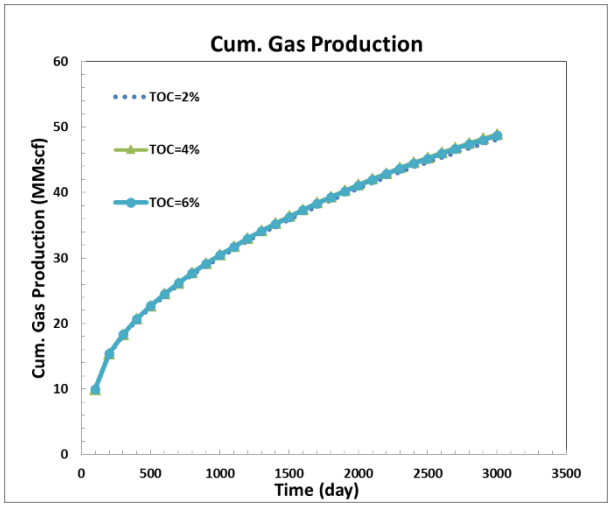

Figure 5.6: Cumulative gas production comparison of 3 TOC values for Fluid Type 1

Later another set of fluid (we name it as Fluid Type 2) is investigated, which consists only 3 hydrocarbon components C1, C2 and C8 with their initial molar fraction as 0.95, 0.01 and 0.04 respectively. The reservoir and fracture properties keep the same except for the initial reservoir pressure and bottom hole pressure change to 4568 psi and 2000 psi, respectively. The cumulative oil and gas production for the three TOC cases is shown in Fig.5.8 and Fig.5.9, respectively. The difference for the influence of TOC on cumulative shale fluid production is obvious and significant for this fluid type and consistent with our intuition that the larger TOC, the more shale gas and oil we recover. From the above investigations, we conclude that multi-component adsorption brought

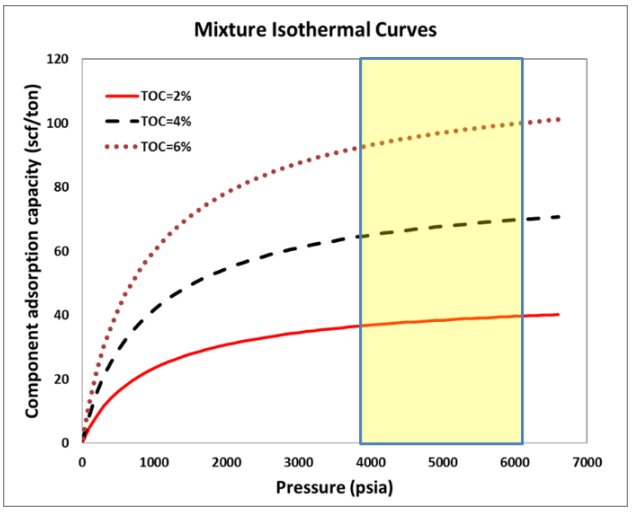

Figure 5.7: Fluid mixture isotherm curves for Fluid Type 1

up by the existence of organic matter will usually play a positive role in shale reservoir recovery, yet the influence of different TOC values on shale fluid recovery may be different depending on the fluid composition and the operating conditions. For example, for test of Fluid Type 1, changing TOC from 2% to 6% will produce almost no change for cumulative gas production, yet for test of Fluid Type 2, the change is quite noticeable.

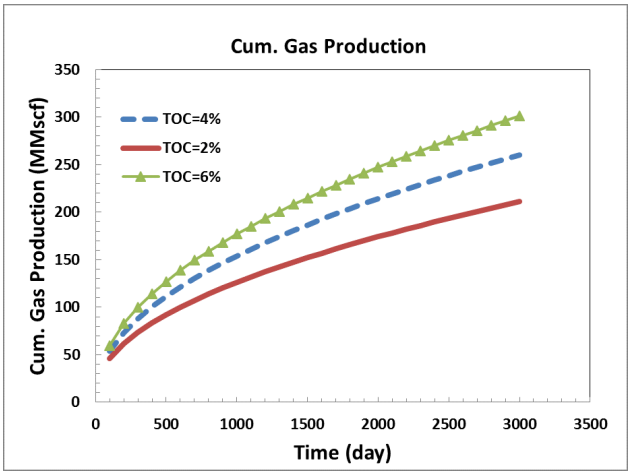

Figure 5.8: Cumulative gas production comparison of 3 TOC values for Fluid Type 2

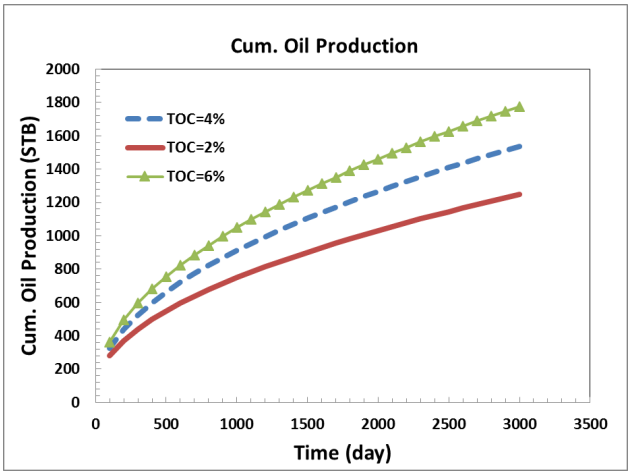

Figure 5.9: Cumulative oil production comparison of 3 TOC values for Fluid Type 2

5.4.2 Diffusion feature case study

In this part, first the diffusion feature in our compositional model is tested in a simple 1D case. Then a 2D reservoir scale model is constructed, with an additional intention is to investigate the influence of diffusivity and wettability on shale fluid recovery.

(A) Validation of the diffusion feature: First the same conceptual model as depicted in Fig.3 of Hoteit (2013) is considered. A binary mixture of C1 and CO2 is existing in a 1D porous medium of length 100 ft, with initially that C1 saturates the left half of the domain, and CO2 saturates the right half of the domain. The diffusion coefficients are set to be 1 ft^2/d for both components. The sketch of the porous medium and the initial gas composition is shown in Fig.5.10. The intra-diffusion of this binary mixture will be simulated under the standard PVT condition using our simulator, results are compared with the analytical solution given by Eq.(58) in Hoteit (2013). The grid size is $20 \times 1 \times 1$ with each grid 5 ft long equally. The comparison result at 100 days is shown in Fig.5.11. We can see the results from our simulator and the analytical calculation are very close.

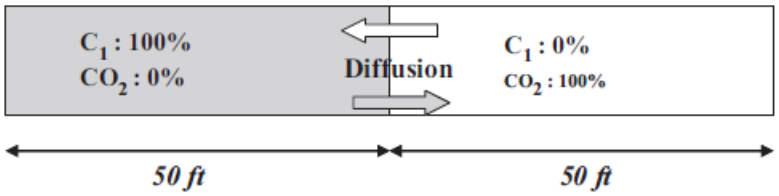

Figure 5.10: Sketch of the binary mixture conceptual model. Reprinted from Fig.3 in Hoteit (2013)

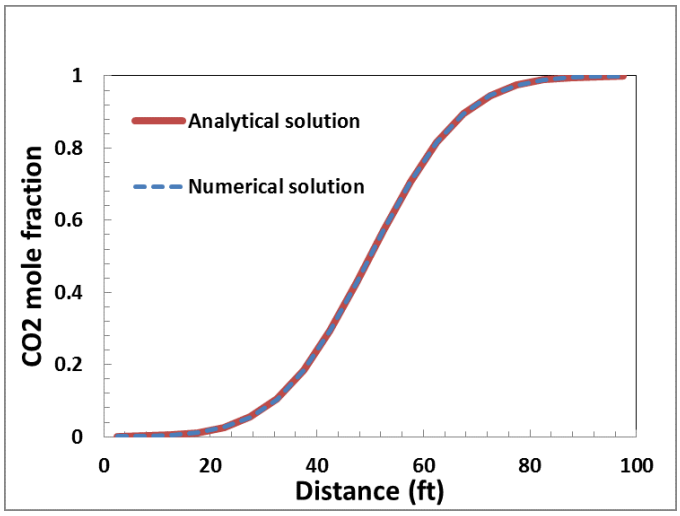

Figure 5.11: Comparison of CO2 mole fraction as distance at 100 days

(B) Reservoir model investigation: In this part, we construct a simple reservoir model with a synthetic reservoir fluid consisting of ternary hydrocarbon components of C1, C2, and C8. This simulation has a twin purpose: first to test the multi-component diffusion feature in a reservoir scale modeling, and the second is to investigate how wettability together with diffusion may influence the production profiles from shale reservoirs, since besides the water wet character, in some cases, the shale systems may present less water wet properties (negative capillary pressure curves) (Jurus et al. 2013), and to our knowledge, not much research has been carried out studying the combined effects of wettability and diffusion.

A shoe-box shape homogeneous reservoir (200 ft long, 200 ft wide and 100 ft thick) with a single vertical well drilling in the center is investigated, no hydraulic fracturing stimulation is considered. One quarter of the reservoir is selected as the simulation unit. And the specific reservoir properties and parameters are listed in Table 5.6. The initial water saturation is 0.25 and 0.1 for water wet and oil wet case, respectively. The initial molar composition for the three components C1, C2 and C8 is 0.82, 0.1, and 0.08, respectively.

Initial Water Saturation	0.25/0.1
Porosity in Shale	0.1
Compressibility of Shale	3e-6 psi^{-1}
Permeability of Shale	0.001 md
Reservoir Thickness	100 ft
Reservoir Width	200 ft
Reservoir Length	200 ft
Fracture Width	0.001 ft
Grid Size	$20 \times 20 \times 1$
Initial Reservoir Pressure	3600 psi
Initial Reservoir Temp	180 F°

Table 5.6: Reservoir and fracture properties specification

The capillary pressure curves introduced by Jia et al. (2013) are modified and incorporated into our simulator, and the relative permeability curves for water wet case are borrowed from Haghshenas et al. (2014), which are represented by Fig.5.12. By analogy, a set of relative permeability curves for oil wet case is developed, and shown in Fig.5.13. To simplify the problem, only the diagonal terms in the diffusivity matrix are considered (which means the component interactions are ignored). The same diffusivity of 1 ft^2/d is assigned to the components. The experimental diffusivity values for this ternary system in shale matrix under reservoir conditions are not available. Dutta (2009) reported a scale of 0.65 ft^2/d for a ternary system (CO2, N2, CH4) at a condition of 305 K and 400 psia. Considering the increase in reservoir temperature and especially the enhancement from Knudsen diffusion, this value we assigned appears reasonable. The results for

different wettability cases with and without considering diffusion are presented in Fig.5.14 and Fig.5.15. The results indicate that no matter what wettability the shale formation is, diffusion will invariably improve the gas recovery. Yet the degree of this improvement differs for different wettability cases; the diffusion exerts a larger positive role for the oil wet wettability case than that for the water wet wettability case. The reason is likely to be: that for the oil wet case, diffusion can effectively accelerate the recovery of the hydrocarbon components and mitigate the chances of these components dropping out as condensates and blocking the flow pathways. Thus the gas recovery in these oil wet reservoirs is largely enhanced.

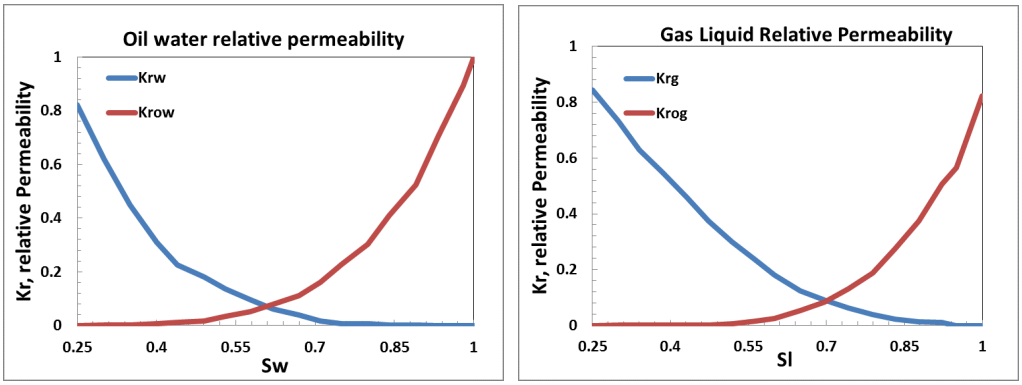

(a) Oil water relative perm curves (b) Gas liquid relative perm curves

Figure 5.12: Relative permeability curves used for water wet case. Reprinted from Fig.3 in Haghshenas et al. (2014)

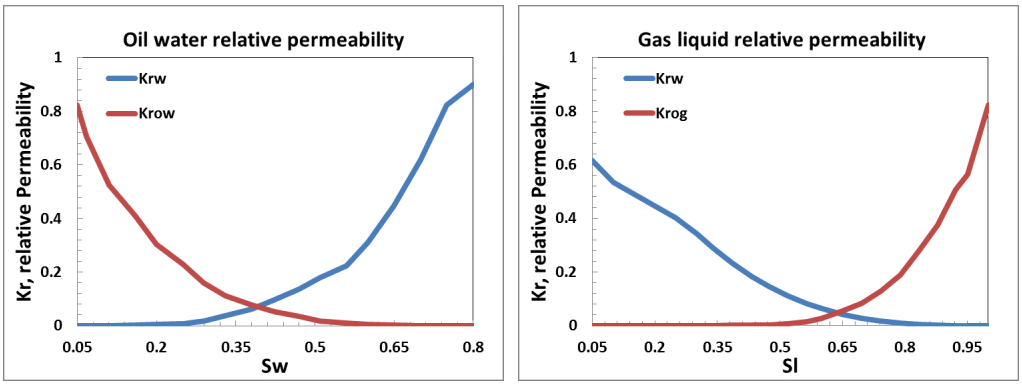

(a) Oil water relative perm curves (b) Gas liquid relative perm curves

Figure 5.13: Relative permeability curves used for oil wet case

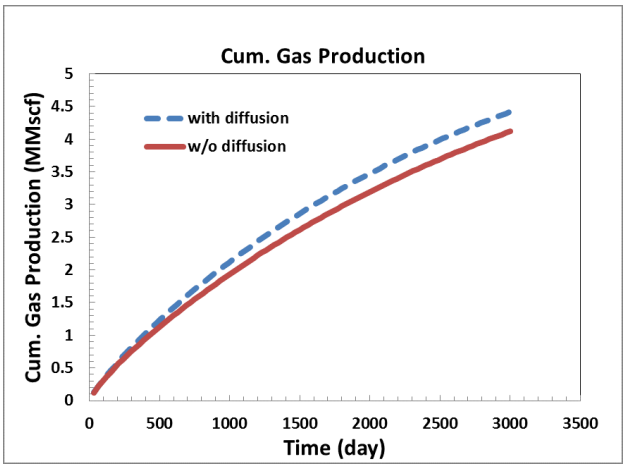

Figure 5.14: Cumulative gas production comparison with and without comparison (water wet case)

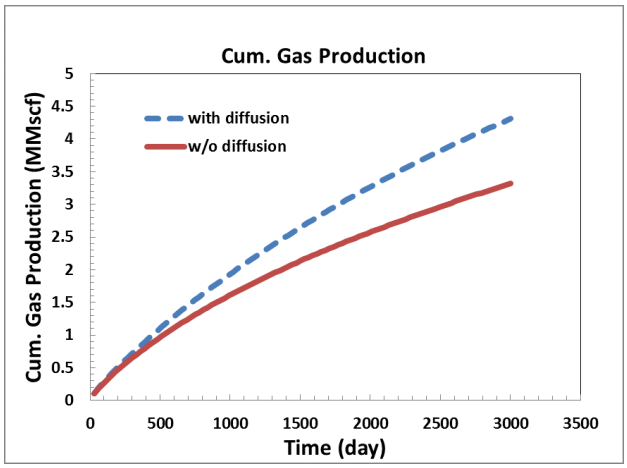

Figure 5.15: Cumulative gas production comparison with and without comparison (oil wet case)

5.5 Conclusions

A compositional model specially designed for modeling fluid flow in shale reservoirs was developed. The multi-component adsorption and diffusion terms for the model are incorporated into the governing equations. The IMPEM method is applied as the solution technique.

Case studies have been conducted to validate the proposed model, and the influences of some important parameters, such as bottom hole pressure, TOC, wettability, and fluid type, on shale reservoir fluid recovery were investigated. The results indicate: multi-component adsorption which mainly exists in the shale organic matter usually plays a positive role in shale reservoir recovery, yet the influence of different TOC values on shale fluid recovery may be different depending on the fluid type and the operating conditions; multi-component diffusion will facilitate the gas recovery, but the degree of this improvement differs in different wettability formations, a larger positive role appears for oil wet wettability case. These tests and results illustrate the validity and capacity of our established model.

Later more work can be done to improve the model, such as adopting a more efficient solution technique (adaptive implicit or fully implicit method), and developing the feature to consider the special phase behavior in shale nano-pores.

6. CONCLUSIONS AND FUTURE WORK

Considering the explicit fracture modeling can better capture the flow intricacies and dynamics in fractured reservoirs, and the inconvenience of the domain discretization techniques (such as FDM, FEM) in dealing with complex explicit fracture modeling, we developed a more concise and efficient BEM based approach to model fluid flow in fractured porous medium. For simulating the steady state flow in homogeneous reservoirs, only the block boundaries and the fracture surfaces need be discretized, thus the complicated domain discretization is dismissed. When the flow transientness and matrix heterogeneity are concerned, additional internal matrix points are selected and taken into computation, following the procedure of DRBEM. To our knowledge, none of the previous researchers have studied fractured reservoir fluid flow through this approach. For 3D cases, the matrix flow is treated through the BEM approach, while the fluid flow in the fractures is characterized through FVM approach. This greatly adds flexibility to our approach in handling reservoirs with irregular fractures. And the discretization process occurs essentially only on the 2D entities (fracture surfaces and block boundaries), which significantly simplifies the simulation procedure.

Also, a compositional model specially designed for modeling fluid flow in shale reservoirs was developed. The multi-component adsorption and diffusion terms for the model are incorporated into the governing equations. The IMPEM method is applied as the solution technique at the current stage of development. The influences of some important parameters, such as bottom hole pressure, on shale reservoir fluid recovery are investigated through our model. This compositional model can serve as a helpful tool for us to better understand the fluid flow in shale reservoirs and improve the decision-making in shale reservoir development.

Preliminary studies have validated the feasibility of our developed models, but more work in the following aspects can be done in the future.

First, the automation of workflow for simulating fluid flow in 3D fractured reservoirs should be improved. Since external software, which is used in constrained Delaunay triangulation, and

multiple self-developed programs are interactively employed in the process, currently data communication among these components is conducted manually. Later high-level main program should be developed to automatically control the workflow implementation.

Second, our developed BEM based approach simplifies the discretization and element generation process. To further simplify this procedure, especially for the reservoirs with very complex fracture configurations, inspired by the work (Graf and Therrien, 2007; Mustapha and Dimitrakopoulos, 2011; Mustapha et al. 2011), techniques reducing the complex structures yet acceptably honoring the solution accuracy can be implemented. The modified fracture configurations then can be passed to our simulator.

Third, one disadvantage of the BEM is the generation of dense matrix, which may pose heavy burden on computation and storage requirements. Techniques dealing with the generated fully populated matrices from the BEM, such as the fast multipole boundary element method (FMM-BEM) (Liu and Nishimura, 2006), hierarchical matrix (H-Matrix) (Benedetti et al. 2008) are to be explored next step. Also, the coupling usage of FEM and BEM for simulating flow in fractured reservoirs is also recommended to be explored in the future, which will take the advantages of both methods.

Finally, regarding to the compositional simulator, two aspects are to be done to improve the model, adopting a more efficient solution technique (adaptive implicit or fully implicit method), and developing a feature to consider the phase behavior deviation in shale nano-pores.

REFERENCES

[1] Acs, G., Doleschall, S. and Farkas, E. 1985. General Purpose Compositional Model, *Soc. Pet. Eng. J.*, August, 1985:543-553. SPE-10515-PA. http://dx.doi.org/10.2118/10515-PA.

[2] Alfi, M., Yan, B. and Cao, Y. et al. 2014. How to Improve Our Understanding of Gas and Oil Production Mechanisms in Liquid-rich Shale. Paper presented at the SPE Annual Technical Conference and Exhibition held in Amsterdam, The Netherlands, 27-29 October 2014. SPE-170959-MS. doi:10.2118/170959-MS.

[3] Ambrose, R.J., Hartman, R.C. and Diaz-Campos, M. et al. 2010. Shale Gas-in-Place Caculations Part I: New Pore-Scale Considerations. Presented at the SPE Unconventional Gas Conference, Pennsylvania, USA, 23-25 February 2010. SPE-131772-PA. doi:10.2118/131772-PA.

[4] Ambrose, R.J., Hartman, R.C. and Akkutlu, I.Y. 2011. Multi-component Sorbed-phase Considerations for Shale Gas-in-place Caculations. Paper presented at the SPE Production and Opeartions Symposium held in Oklahoma City, Oklahoma, USA, 27-29 March 2011. SPE-141416-MS. http://dx.doi.org/10.2118/141416-MS.

[5] Ang, W. T., 2007. *A Beginner's Course in Boundary Element Methods*, Universal Publishers, Boca Raton, USA, 2007.

[6] Archer, R. A. 2000. *Computing Flow and Pressure Transients in Heterogeneous Media using Boundary Elment Methods*. PH.D thesis, Standford University, Stanford, California (March 2000).

[7] Barenblatt, G. I., and Zheltov, Y. P. 1960. Fundamental equations of filtration of homogeneous liquids in fissured rocks, *Dokl. Akad. Nauk SSSR*, 13, 545 - 548.

[8] Benedetti, I., Aliabadi, M.H. and Davi, G., 2008. A fast 3D dual boundary element method based on hierarchical matrices. *International Journal of Solids and*

Structures, Volume 45, Issues 7-8, 2008, Pages 2355-2376, ISSN 0020-7683, https://doi.org/10.1016/j.ijsolstr.2007.11.018.

[9] Bourke, P., 1989. Intersection point of two line segments in 2 dimensions. Retrieved from http://paulbourke.net/geometry/pointlineplane/.

[10] Cao, Y., Killough, J. E. 2016. An Improved Boundary Element Method for Modeling Fluid Flow through Fractured Porous Medium, presented at the SPE Reservoir Simulation Conference held in Montgomery, TX, USA, 20-22 February, 2017. SPE-182658-MS. http://dx.doi.org/10.2118/182658-MS.

[11] Chai, Z., Yan, B. and Killough, J. E. 2016. Dynamic Embedded Discrete Fracture Multi-Continuum Model for the Simulation of Fractured Shale Reservoirs. Paper presented at the International Petroleum Technology Conference held in Bangkok, Thailand, 14-16 November 2016. IPTC-18887-MS.

[12] Chaudhary, A. S., Ehlig-Economides, C. and Wattenbarger, R. 2011. Shale Oil Production Performance from a Stimulated Reservoir Volume. Paper presented at the SPE Annual Technical Conference and Exhibition held in Denver, Colorado, USA, 30 October-2 Novemeber 2011. SPE-147596-MS. http://dx.doi.org/10.2118/147596-MS.

[13] Civan, F. 2010. Effective correlation of apparent gas permeability in tight porous media, *Transport in Porous Media*, Vol.82:375-384.

[14] Crank, J. 1975. *The mathematics of diffusion*. Oxford [England] : Clarendon Press.

[15] Clarkson, C. R. and Ertekin, T. 2010. A new model for shale gas matrix flow using the dynamic-slippage concept. AAPG Hedberg Conference, Austin, Texas, December 5-10.

[16] Dershowitz, B., LaPointe, P., Eiben, T. et al. 2000. Integration of discrete fracture network methods with conventional simulator approaches, *SPE Reservoir Eval. Eng.*, 3(2), 165-170.

[17] Ding, D. Y., Farah, N., Bourbiaux. B. et al. 2017. Simulation of Matrix-Fracture Interaction in Low-Permeability Fractured Unconventional Reservoirs. Paper presented at the SPE Reservoir

Simulation Conference held in Montgomery, TX, USA, 20-22 February 2017. SPE-182608-MS. http://dx.doi.org/10.2118/182608-MS.

[18] Dutta, A. 2009. *Multicomponent Gas Diffusion and Adsorption in Coals for Enhanced Methane Recovery.* MA thesis, Stanford University, Stanford, California (June 2009).

[19] El Harrouni, K., Ouazar, D., Wrobel, L. C. et al. 1996. Global Interpolation Function Based DRBEM Applied to Darcy's Flow in Heterogeneous Media. *Engineering Analysis with Boundary Elements*, 1996, 281-285.

[20] Ertekin, T., King, G. R. and Schwerer, F. C. 1986. Dynamic gas slippage: a unique dual-mechanism approach to the flow of gas in tight formations. *SPE Formation Evaluation*, 1(1): 43-52. Paper SPE-12045-PA. http://dx.doi.org/10.2118/12045-PA.

[21] Freeman, C. M., Moridis, G. J. and Blasingame, T. A. 2013. Modeling and Performance Interpretation of Flowing Gas Composition Changes in Shale Gas Wells with Complex Fractures. Paper presented at the International Petroleum Technology Conference held in Beijing, China, 26-28 March 2013. SPE-17075-MS. http://dx.doi.org/10.2523/17075-MS.

[22] Gasem, K.A.M., Mohammad, S. and Robinson Jr., R.L. 2009. Modeling Coalbed Methane Adsorption and CO2 Sequestration. *In Encyclopedia of Chemical Processing*. Taylor and Francis: New York, Published online: 28 May 2009; 1-21.

[23] Gaul, L., Kögl, M., and Wagner M., 2003. *Boundary Element Methods for Engineers and Scientists: An Introductory Course with Advanced Topics*. Berlin, Germany: Springer-Verlag, 2003.

[24] Geuzaine, C. and Remacle, J.-F. Gmsh: a three-dimensional finite element mesh generator with built-in pre- and post-processing facilities. *International Journal for Numerical Methods in Engineering* 79(11), pp. 1309-1331, 2009.

[25] Gilman, J. R. 1986. An efficient finite-difference method for simulating phase segregation in the matrix blocks in double-porosity reservoirs, *SPE Reservoir Eng.*, 1, 403-413.

[26] Gilman, J. R., and Kazemi, H. 1988. Improved calculations for viscous and gravity displacement in matrix blocks in dual-porosity simulators, *JPT J. Pet. Technol.*, 40(1), 60-70.

[27] Gong, B., Karimi-Fard, M., and Durlofsky, L. J. 2008. Upscaling Discrete Fracture Characterizations to Dual-Porosity, Dual-Permeability Models for Efficient Simulation of Flow With Strong Gravitational Effects. March 2008 SPE J. http://dx.doi.org/10.2118/102491-PA.

[28] Graf T and Therrien R. A method to discretize non-planar fractures for 3D subsurface flow and transport simulations. *International Journal for Numerical Methods in Fluids* 2007; 56:2069-2090.

[29] Haghshenas, B., Soroush, M. and Brohi, I. et al. 2014. Simulation of Liquid-Rich Shale Gas Reservoirs with Heavy Hydrocarbon Fraction Desorption. Paper presented at the SPE Unconventional Resources Conference - USA held in The Woodlands, Texas, USA, 1-3 April 2014. SPE-168968-MS. http://dx.doi.org/10.2118/168968-MS.

[30] Hajibeygi, H., Karvounis, D. and Jenny, P. 2011. A hierarchical fracture model for the iterative multiscale finite volume method [J]. *Journal of Computational Physics*, 2011, 230(24): 8729-8743.

[31] Halliburton, 2008. *Coalbed Methane: Principles and Practices*, Chapter 3, Sorption, 147. http://www.halliburton.com/public/pe/contents/Books_and_Catalogs/web/CBM/H06263_Chap_03.pdf.

[32] Halliburton, 2013. *Nexus® Technical Reference Guide*, Chapter 10, Multi-Porosity, 366. Houston, TX: Author.

[33] He, J., Killough, J. E., Fadlelmula, M. M. et al. 2015. A Unified Finite Difference Model for the Simulation of Transient Flow in Naturally Fractured Carbonate Karst Reservoirs. Paper presented during the SPE Reservoir Simulation Symposium, 23-25 February, Houston, TX, USA. SPE-173262-MS. http://dx.doi.org/10.2118/173262-MS.

[34] Hill, D. G. and Nelson, C. R. 2000. *Gas productive fractured shales: an overview and update*. Gas TIPS 6(3): 4-13. Hart Energy Publishing, Houston, TX.

[35] Hinkley, R., Wang, Q., Wang, K. et al. 2013. Flexible and Efficient N-Porosity, Full-Featured Simulator Design, and Application. Paper presented at the 2013 SPE Reservoir Simulation Symposium, The Woodlands, TX, USA. SPE-163619-MS. http://dx.doi.org/10.2118/163619-ms.

[36] Hoteit, H. 2013. Modeling Diffusion and Gas-oil Mass Transfer in Fractured Reservoirs. *Journal of Petroleum Science and Engineering* 105 (2013) 1-17.

[37] Hui, M., Gong, B., Karimi-Fard, M. et al. 2007. Development and application of new computational procedures for modeling miscible gas injection in fractured reservoirs, presented at the SPE Annual Technical Conference and Exhibition, Anaheim, California, U.S.A., November 11-14. Paper SPE 109686. http://dx.doi.org/10.2118/109686-MS.

[38] Hui, M., Mallison, B., and Lim, K. 2008. An Innovative Workflow to Model Fractures in a Giant Carbonate Reservoir, presented at the International Petroleum Technology Conference, Kuala Lumpur, Malaysia, 3-5 December. Paper IPTC 12572.

[39] Javadpour, F. 2009. Nanopores and apparent permeability of gas flow in mudrocks (shales and siltstone). *J. of Canadian Petroleum Tech.*, v. 48, pp 16-21.

[40] Jiang, J., and Younis, R. M. 2015. A Generic Physics-based Numerical Platform with Hybrid Fracture Modelling Techniques for Simulating Unconventional Gas Reservoirs. Paper presented at the SPE Reservoir Simulation Symposium held in Houston, Texas, USA, 23-25 February 2015. SPE-173318-MS. http://dx.doi.org/10.2118/173318-MS.

[41] Jia, H., McLennan, J. and Deo, M. 2013. The Fate of Injected Water in Shale Formations. Available online at http://dx.doi.org/10.5772/56443.

[42] Jurus, W. J., Whitson, C. H. and Golan, M. 2013. Modeling Water Flow in Hydraulically-Fractured Shale Wells. Paper presented at the SPE Annual Technical Conference and Exhibition held in New Orleans, Louisiana, USA, 30 Spetpermeber-2 October 2013. SPE-166439-MS. doi:10.2118/166439-MS.

[43] Karimi-Fard, M., Durlofsky, L. J., and Aziz, K. 2004. An Efficient Discrete-Fracture Model Applicable for General-Purpose Reservoir Simulator. June 2004 *SPE Journal*. http://dx.doi.org/10.2118/88812-PA.

[44] Karimi-Fard, M., Gong, B., and Durlofsky, L. J. 2006. Generation of coarse-scale continuum flow models from detailed fracture characterizations, *Water Resour. Res.*, 42, W10423, http://dx.doi.org/10.1029/2006WR005015.

[45] Kazemi, H., Merrill Jr., L. S., Porterfield, K.L. et al. 1976. Numerical Simulation of Water-Oil Flow in Naturally Fractured Reservoirs. *Society of Petroleum Engineers Journal* 16 (6): 317-326. http://dx.doi.org/10.2118/5719-pa.

[46] Leahy-Dios, A. and Firoozabad, A. 2007. Unified Model for Non-ideal Multicomponent Molecular Diffusion Coefficient. *AICHE J.*, 53(11), 2932-2939. DOI: 10.1002/aic.11279.

[47] Lee, S. H., Lough, M. F., and Jensen, C. L. 2001. Hierarchical modeling of flow in naturally fractured formations with multiple length scale. *Water Resources Research*, 37(3), December, pp. 443-445.

[48] Li, L. and Lee, S. H., 2008. Efficient Field-Scale Simulation of Black Oil in a Naturally Fractured Reservoir Through Discrete Fracture Networks and Homogenized Media, SPEREE, 2008.

[49] Liu,Y. J. and Nishimura, N., 2006. The fast multipole boundary element method for potential problems: A tutorial. *Engineering Analysis with Boundary Elements*, Volume 30, Issue 5, 2006, Pages 371-381, ISSN 0955-7997, https://doi.org/10.1016/j.enganabound.2005.11.006.

[50] Loucks, R.G., Reed, R. M. and Ruppel, S. C. et al. 2009. Morphology, Genesis, and Distribution of Nanometer- Scale Pores in Siliceous Mudstones of the Mississippian Barnett Shale. *Journal of Sedimentary Research* 79: 848-861. http://dx.doi.org/10.2110/jsr.2009.092.

[51] Lough, M. F., Lee, S. H. and Kamath, J. 1995. Modeling of fractured reservoirs using the boundary element method. *Transactions on Modelling and Simulation* vol 9, 1995 WIT Press, www.witpress.com, ISSN 1743-355X.

[52] Lough, M. F., Lee, S. H. and Kamath, J. 1997. A new method to calculate effective permeability of gridblocks used in the simulation of naturally fractured reservoirs. *SPE Reservoir Engineering*, August 1997.

[53] Lough, M. F., Lee, S. H. and Kamath, J. 1998. An Efficient Boundary Integral Formulation for Flow through Fractured Porous Media. *Journal of Computational Physics* 143, 464-483 (1998), Article NO. CP985858.

[54] Luo, H. S., Wang, X. H. and Quintard, M. 2008. Adaptive Mesh Refinement for One-Dimensional Three-Phase Flows in Heterogeneous Fractured Porous Media. *Numerical Heat Transfer, Part B: Fundamentals*, 54(6), 476-498.

[55] McKoy, M.L., Sams, W.N., 1997. Tight gas reservoir simulation: modeling discrete irregular strata-bound fracture networks and network flow, including dynamic recharge from the matrix. Paper P17 presented at the 1997 DOE Natural Gas Conference, Houston, TX, March 24-27.

[56] Mi, L., Jiang, H., Wang, Y. et al. 2016. Hydraulic Fracture Optimization Based on Discrete Fracture Network Model in Shale Reservoirs. International Petroleum Technology Conference. http://dx.doi.org/10.2523/IPTC-18884-MS.

[57] Moinfar, A. 2013. *Development of an Efficient Embedded Discrete Fracture Model for 3D Compositional Reservoir Simulation in Fractured Reservoirs*. PHD thesis, University of Texas at Austin.

[58] Moinfar, A., Narr, W., Hui, M.H. et al. 2011. Comparison of Discrete-Fracture and Dual-Permeability for Multiphase Flow in Naturally Fractured Reservoirs. Paper presented at the SPE Reservoir Simulation Symposium held in The Woodlands, Texas, USA, 21-23 February 2011. SPE 142295. http://dx.doi.org/10.2118/142295-MS.

[59] Mustapha, H. and Dimitrakopoulos, R. 2011. Discretizing two-dimensional complex fractured fields for incompressible two-phase flow. *Int. J. Numer. Meth. Fluids*, 65: 764-780. http://dx.doi.org/10.1002/fld.2197.

[60] Mustapha, H., Dimitrakopoulos, R., Graf, T. et al. 2011. An efficient method for discretizing 3D fractured media for subsurface flow and transport simulations. *Int. J. Numer. Meth. Fluids*, 67: 651-670. http://dx.doi.org/10.1002/fld.2383.

[61] Orangi, A., Nagarajan, N. R. and Honarpour, M. M. et al. 2011. Unconventional Shale Oil and Gas-Condensate Reservoir Production, Impact of Rock, Fluid, and Hydraulic Fractures. Paper presented at the SPE Hydraulic Fracturing Technology Conference and Exhibition held in The Woodlands, Texas, USA, 24-26 January 2011. SPE-140536-MS. http://dx.doi.org/10.2118/140536-MS.

[62] Partridge, P.W., Brebbia, C.A. and Wrobel, L.C. 1991. *The Dual Reciprocity Boundary Element Method*. Springer, London (1991).

[63] Peng, D. Y. and Robinson, D. B. 1976. A New Two-Constant Equation of State. *Industrial & Engineering Chemistry Fundamentals* 15 (1): 59-64. http://dx.doi.org/10.1021/i160057a011.

[64] Pruess, K., and Karasaki, K. 1982. Proximity Function for Modeling Fluid and Heat Flow in Reservoirs with Stochastic Fracture Distributions. Proceedings Eighth Workshop Geothermal Reservoir Engineering Stanford University, Stanford, California, December 1982, SGP-TE-60.

[65] Pruess, K., and Narasimhan, T. N. 1985. A practical method for modeling fluid and heat flow in fractured porous media, *SPE J.*, 25, (1), 14-26.

[66] Rasmussen, T. C., Yeh, T. C. J. and Evans, D. D. 1987. Effect of variable fracture permeability/matrix permeability ratios on three-dimensional fractured rock hydraulic conductivity, Proceedings of the Conference on Geostatistical, Sensitivity, and Uncertainty Methods for Ground-Water Flow and Radionuclide Transport Modeling, San Francisco, California, September 1987, edited by B. E. Buxton (Batelle Press, Columbus, OH, 1987), p. 337.

[67] Rubin, B. 2010. Accurate Simulation of Non Darcy Flow in Stimulated Fractured Shale Reservoirs. Paper presented at the SPE Western Regional Meeting, Anaheim, California, USA, 27-29 May. SPE-132093-MS. http://dx.doi.org/10.2118/132093-MS.

[68] Sarda, S., Jeannin, L., Basquet, R. et al. 2002. Hydraulic characterization of fractured reservoirs: Simulation on discrete fracture models, *SPE Reservoir Eval. Eng.*, 5(2), 154-162.

[69] Sarma, P., and Aziz, K. 2004. New transfer functions for simulation of naturally fractured reservoirs with dual porosity models, presented at the SPE Annual Technical Conference and Exhibition, Soc. of Pet. Eng., Houston, Texas. SPE 90231. http://dx.doi.org/10.2118/90231-MS.

[70] Shapiro, A. M. and Andersson, J. 1983. Steady State Fluid Response in Fractured Rock: A Boundary Element Solution for a Coupled, Discrete Fracture Continuum Model. *Water Resources Research*, VOL. 19, NO. 4, PAGES 959-969, AUGUST 1983.

[71] Sherwood, T., Pigford, P. and Wilke, C., 1975. *Mass Transfer*, McGraw Hill, New York.

[72] Shewchuk, J. R., Delaunay Refinement Algorithms for Triangular Mesh Generation, *Computational Geometry: Theory and Applications* 22(1-3):21-74, May 2002. PostScript (5,128k, 54 pages).

[73] Sun, H., Chawathe, A., Hoteit, H. et al. 2014. Understanding Shale Gas Production Mechanisms through Reservoir Simulation. Paper presented at the SPE/EAGE European Unconventional Conference and Exhibition held in Vienna, Austria, 25-27 February 2014. SPE-167753-MS. http://dx.doi.org/10.2118/167753-MS.

[74] Sun, J. and Schechter, D. 2014. Optimization-Based Unstructured Meshing Algorithms for Simulation of Hydraulically and Naturally Fractured Reservoirs with Variable Distribution of Fracture Aperture, Spacing, Length and Strike. Paper presented at the SPE Annual Technical Conference and Exhibition held in Amsterdam, The Netherlands, 27-29 October 2014. SPE-170702-MS. http://dx.doi.org/10.2118/170702-MS.

[75] Syihab, Z. 2009. *Simulation on Discrete Fracture Network Using Flexible Voronoi Grid System*. PHD thesis, Texas A&M University.

[76] Teimoori, A., Chen, Z., Rahman, S. S. et al. 2005. Effective Permeability Calculation Using Boundary Element Method in Naturally Fractured Reservoirs, *Petroleum Science and Technology*, 23:5-6, 693-709, http://dx.doi.org/10.1081/LFT-200033029.

[77] Thomas, L. K., Dixon, T. N., and Person, R. G. 1983. Fractured reservoir simulation. *SPE J.*, 23(1), 42-54.

[78] Wang, C., Wu, Y., Xiong, Y., et al. Geomechanics Coupling Simulation of Fracture Closure and Its Influence on Gas Production in Shale Gas Reservoirs. Paper presented at the SPE Reservoir Simulation Symposium held in Houston, Texas, USA, 23-25 February, 2015. SPE-173222-MS. http://dx.doi.org/10.2118/173222-MS.

[79] Wang, F. P. and Reed, R. M. 2009. Pore Networks and Fluid Flow in Gas Shales. Paper presented at the SPE Annual Technical Conference and Exhibition, New Orleans, Louisiana. SPE-124253-MS. http://dx.doi.org/10.2118/124253-ms.

[80] Warren, J. E., and Root, P. J. 1963. The behavior of naturally fractured reservoirs, *SPE J.*, 3(3), 245-255.

[81] Wong, T. W., Firoozabadi, A. and Nutakki, R. 1987. A comparison of Two Approaches to Compositional and Black Oil Simulation. Paper presented at the Ninth SPE Symposium on Reservoir Simulation held in San Antonio, Texas, February 1-4, 1987. SPE-15999-MS. http://dx.doi.org/10.2118/15999-MS.

[82] Wu, Y. S., and Pruess, K. 1988. A multiple-porosity method for simulation of naturally fractured petroleum reservoirs, *SPE Reservoir Eng.*, 3, 327-336.

[83] Yan, B., Alfi, M., Cao, Y. et al. 2015. Advanced Multiple Porosity Model for Fractured Reservoirs. International Petroleum Technology Conference. IPTC-18308-MS. http://dx.doi.org/10.2523/IPTC-18308-MS.

[84] Yan, B., Wang, Y. and Killough, J. E. 2013. Beyond Dual-Porosity Modeling for the Simulation of Complex Flow Mechanisms in Shale Reservoirs. Paper presented at the SPE Reser-

voirs Simulation Symposium held in The Woodlands, Texas USA, 18-20 February, 2013. SPE-163651-MS. http://dx.doi.org/10.2118/163651-MS.

[85] Zhang, Y. L. and Zhu, S. P. 1994. On the choice of interpolation functions used in the dual-reciprocity boundary-element method. *Engineering Analysis with Boundary Elements* 13 (1994) 387-396.

[86] Zhang T.W., Ellis, G.S. and Ruppel, S. C et al. 2012. Effect of Organic-matter Type and Thermal Maturity on Methane Adsorption in Shale-gas Systems. *Organic Geochemistry*, 47 (2012) 120-131.

[87] Zimmerman, R. W., Chen, G., Hadgu, T. et al. 1993. A numerical dual-porosity model with semianalytical treatment of fracture/matrix flow, *Water Resour. Res.*, 29, 2127-2137.